Phase Gradient Estimation Techniques in Fringe Analysis

THÈSE N^O 5375 (2012)

PRÉSENTÉE LE 6 JUILLET 2012

À LA FACULTÉ DE L'ENVIRONNEMENT NATUREL, ARCHITECTURAL ET CONSTRUIT

LABORATOIRE D'INFORMATIQUE ET DE MÉCANIQUE APPLIQUÉES À LA CONSTRUCTION

PROGRAMME DOCTORAL EN PHOTONIQUE

ÉCOLE POLYTECHNIQUE FÉDÉRALE DE LAUSANNE

POUR L'OBTENTION DU GRADE DE DOCTEUR ÈS SCIENCES

PAR

Rajshekhar GANNAVARPU

acceptée sur proposition du jury:

Prof. O. Martin, président du jury
Prof. P. Rastogi, directeur de thèse
Prof. D. Ambrosini, rapporteur
Dr E. Hack, rapporteur
Prof. L. Pflug, rapporteur

Abstract

The thesis introduces novel techniques in the field of fringe analysis for direct estimation of phase gradients or derivatives. A pseudo Wigner-Ville distribution based method is proposed to reliably estimate the phase derivatives from a single fringe pattern. The method's ability for estimating rapidly varying phase derivatives is enhanced by developing an adaptive windowing technique. Further, the two-dimensional extension of the method is presented to handle fringe patterns with severe noise. In addition, a generalized approach is described to enable direct estimation of arbitrary order phase derivatives. Subsequently, methods based on digital holographic moiré and multi-component polynomial phase formulation are introduced to measure the in-plane and out-of-plane displacements and their derivatives for a deformed object in digital holographic interferometry. These methods permit the simultaneous estimation of multiple phases and their derivatives without the need of multiple fringe patterns and complex experimental configurations, which is hitherto not possible with the current state-of-the-art fringe analysis methods.

The major advantages of the developed techniques are the ability to directly estimate phase derivatives without relying on complex unwrapping, filtering and numerical differentiation operations, high computational efficiency and strong robustness against noise. In addition, the requirement of a single fringe pattern makes these techniques less error-prone in the presence of vibrations and external disturbances and enhances their applicability for dynamic measurements. Further, the developed techniques offer a potential solution to the challenging problem of simultaneous multi-dimensional deformation analysis in digital holographic interferometry. The reliable performance of these techniques is validated by numerical simulation and their practical applicability is demonstrated in digital holographic interferometry and fringe projection for slope and curvature measurement, defect detection, surface slope evolution studies and measurement of in-plane and out-of-plane displacements and their derivatives. These techniques offer substantial advancements in fringe analysis and exhibit significant application potential in areas such as non-destructive testing, biomechanics, reliability analysis, material characterization and experimental mechanics.

Keywords: Fringe analysis, phase derivative estimation, digital holographic interferometry, slope and curvature measurement, multi-dimensional deformation analysis

Résumé

Cette thèse introduit de nouvelles techniques dans le domaine de l'analyse de franges pour l'estimation directe des gradients ou des dérivés de phases. Une méthode basée sur la pseudo-distribution de Wigner-Ville est proposée afin d'estimer de façon fiable les dérivées de phases à partir d'un seul motif de franges. La capacité de la méthode à estimer les variations rapides des dérivés de phases est améliorée en développant une technique de fenêtre adaptative. La méthode est généralisée pour des problèmes en deux dimensions afin de traiter les motifs de franges contaminés par un niveau de bruit élevé. En plus de permettre l'estimation directe des dérivées de phases d'ordres arbitraires, une approche basée sur une distribution généralisée est décrite. Par la suite, des méthodes basées sur le moiré holographique digitale ainsi que sur une formulation polynomiale multi-composante des phases sont proposées afin de mesurer les déformations spécifiques et les déplacements dans le plan et hors du plan d'un objet en interférométrie holographique digitale. Ces méthodes permettent l'estimation simultanée de plusieurs phases et de leurs dérivées sans avoir besoin de plusieurs motifs de franges ni de configuration expérimentales complexes.

Les principaux avantages des méthodes développées sont leur capacité à directement estimer les dérivées des phases sans recourir à des analyses complexes et leur robustesse envers les bruits parasites. De plus, la méthode ne nécessite qu'un seul motif de franges ce qui rend l'approche moins sensible aux erreurs en présence de vibrations et des perturbations externes qui sont souvent rencontrées lors de mesures dynamiques. Les techniques développées offrent des solutions potentielles à la problématique de la simulation multi-dimensionnelle des déformées à partir de l'interférométrie holographique. La fiabilité des techniques est validée à l'aide de simulations numériques. Leur applicabilité à des cas pratiques est démontrée pour des mesures de pentes, courbures, défauts et pour suivre l'évolution de surface dans le plan et hors du plan. Ces techniques offrent des avancements substantiels dans le domaine de l'analyse de moirés et se prêtent à une multitude d'applications potentielles telles que les essais non-destructifs, la biomécanique, l'analyse de fiabilité, la caractérisation des matériaux et la mécanique expérimentale.

Mots clefs : Analyse des franges, estimation des dérivées de phases, interférométrie holographique digitale, mesure des pentes et courbures, analyse déformation multidimensionnelles

Acknowledgements

Publications

The work presented in various chapters of the thesis has appeared in the following journals:

1. G. Rajshekhar, S. S. Gorthi, and P. Rastogi, "Strain, curvature and twist measurements in digital holographic interferometry using pseudo Wigner-Ville distribution based method", **Review of Scientific Instruments**, 80, 093107, 2009.

2. G. Rajshekhar, S. S. Gorthi, and P. Rastogi, "An adaptive window Wigner-Ville distribution based method to estimate phase derivative from optical fringes", **Optics Letters**, 34(20), 3151-3153, 2009.

3. G. Rajshekhar, S. S. Gorthi, and P. Rastogi, "Polynomial Wigner-Ville distribution based method for direct phase derivative estimation from optical fringes", **Journal of Optics A: Pure and Applied Optics**, 11(12), 125402, 2009.

4. G. Rajshekhar, S. S. Gorthi, and P. Rastogi, "Estimation of phase derivative using adaptive window spectrogram", **Journal of Optical Society of America A**, 27(1), 69-75, 2010.

5. G. Rajshekhar, S. S. Gorthi, and P. Rastogi, "Estimation of displacement derivatives in digital holographic interferometry using a two-dimensional space-frequency distribution", **Optics Express**, 18(17), 18041-18046, 2010.

6. G. Rajshekhar, S. S. Gorthi, and P. Rastogi, "Estimation of dynamically varying displacement derivatives using fringe projection technique", **Applied Optics**, 50(3), 282-286, 2011.

7. G. Rajshekhar, S. S. Gorthi, and P. Rastogi, "Simultaneous multidimensional deformation measurements using digital holographic moiré", **Applied Optics**, 50(21), 4189-4197, 2011.

8. G. Rajshekhar, S. S. Gorthi, and P. Rastogi, "Simultaneous measurement of in-plane and out-of-plane displacement derivatives using dual-wavelength digital holographic interferometry", **Applied Optics**, 50(34), H16-H21, 2011.

9. G. Rajshekhar and P. Rastogi, "Application of complex-lag distributions for estimation of arbitrary order phase derivatives in digital holographic interferometry", **Optics Letters**, 36(19), 3738-3740, 2011.

10. G. Rajshekhar, S. S. Gorthi, and P. Rastogi, "Estimation of multiple phases from a single fringe pattern in digital holographic interferometry", **Optics Express**, 20(2), 1281-1291, 2012.

11. G. Rajshekhar, S. S. Gorthi, and P. Rastogi, "Detection of defects from fringe patterns using a pseudo Wigner-Ville distribution based method", **Optics and Lasers in Engineering**, 50(8), 1059-1062, 2012.

12. G. Rajshekhar and P. Rastogi, "Fringe analysis: Premise and perspectives", **Optics and Lasers in Engineering**, 50(8), iii-x, 2012.

Contents

List of Figures

List of Tables

Chapter 1

Introduction

1.1 Fringe analysis

Optical techniques like holographic interferometry [1], electronic speckle pattern interferometry [2] and fringe projection [3] are quite popular for non-contact measurements and have many applications in areas such as experimental mechanics, non-destructive testing, profilometry, quality control etc. In all these techniques, the information about the measured physical quantity is usually stored in the phase or its associated derivatives of a fringe pattern. Fringe analysis deals with the extraction of phase (and/or its derivatives) from the fringe pattern.

The mathematical form of a typical fringe pattern is given as

$$I(x, y) = I_0(x, y) + a(x, y) \cos[\phi(x, y)] \tag{1.1}$$

where $I(x, y)$ is the recorded intensity, $I_0(x, y)$ is the background intensity, $a(x, y)$ is the fringe amplitude and $\phi(x, y)$ is the phase. Also, x and y refer to the spatial coordinates or pixels along the horizontal and vertical directions. The main aim of fringe analysis is to estimate ϕ or its derivatives such as $\partial\phi/\partial x, \partial^2\phi/\partial x^2$ etc. from the fringe pattern.

The various fringe analysis methods can be broadly classified in two categories: (1) temporal methods which require multiple fringe patterns to extract phase information and (2) spatial methods which are capable of phase retrieval from a single fringe pattern. The selection of a particular fringe analysis method depends on various factors such as dynamic or static nature of the application, noise, experimental stability, ease of use etc.

Phase-shifting [4] is a popular temporal fringe analysis technique and relies on recording multiple fringe patterns where the phase is incremented between successive frames. For phase extraction in phase-shifting, several methods based on Carré's algorithm [5], the N-bucket algorithm [6, 7], least-squares approach [8], characteristic polynomials [9, 10],

symmetrical phase-shifting algorithm [11], error compensating algorithms [12–23] etc. have been proposed.

Due to the requirement of multiple fringe patterns, temporal methods are difficult to apply for dynamic measurements and quite susceptible to external disturbances and vibrations. Thus, for many applications, extraction of information about the phase or its derivative from a single fringe pattern is desired, which falls under the purview of *spatial* fringe analysis. Various spatial fringe analysis methods based on Fourier transform [24], dilating Gabor transform [25], wavelet transform [26], windowed Fourier transform [27], S-transform [28] etc. have been proposed for phase estimation.

The fringe analysis methods usually involve the application of an 'arctan' function for phase extraction. Since the principal values of the inverse function lie in the range $[-\pi, \pi)$, wrapping occurs when the true phase value lies outside the interval and leads to artificial 2π discontinuities in the wrapped phase [29]. Phase *unwrapping* refers to adding integral multiples of 2π to the wrapped phase map to obtain the continuous phase distribution.

In recent decades, several phase unwrapping algorithms such as noise-immune unwrapping [30], least-squares method [31], minimum cost-matching algorithm [32], flood fill [33], branch-cut algorithm [34], Goldstein's algorithm [35], ZπM algorithm [36], adaptive integration [37], region growing approach [38], local histogram method [39], region-referenced methods [40, 41], multilevel quality guided algorithm [42], phase estimation using adaptive regularization based on local smoothing (PEARLS) [43], local polynomial approximation [44] etc. have been proposed for fringe analysis. It needs to be emphasized that the unwrapping operation adds an extra step in the phase estimation procedure, thereby increasing the overall computational burden and is usually error-prone in the presence of noise.

1.2 Estimation of phase derivatives

Though phase is important, however, the quantities of great interest in areas such as experimental mechanics and non-destructive testing are the *gradients* or *derivatives* of phase. For an object subjected to deformation, the first order phase derivative is related to the derivative of surface displacement [45] and the second order phase derivatives provide information about the flexural and torsional moments i.e. curvature and twist [46]. Consequently, the phase derivatives are of profound significance in applications such as quality assessment [47], residual stress evaluation [48], fault identification [49], leakage detection [50], material characterization [51], biomechanical studies of dentin [52], bones [53, 54] and vascular wall [55], surface slope measurement [56], refractive index profiling [57] etc. Hence, reliable estimation of phase derivatives is highly desired.

It needs to be emphasized that direct estimation of the phase derivative is preferred to the obvious approach of phase estimation and subsequent differentiation for many practical

applications. The reason is the susceptibility of the usually required phase unwrapping and numerical differentiation operations to noise which makes the procedure error-prone [58]. For direct estimation of the phase derivatives, several optical techniques based on shearography [59–63], moiré [64–67] and speckle shearing interferometry [46, 68–70] have been developed. One of the principal reasons behind the widespread popularity and use of shearography in non-destructive testing applications has been the ability to provide fringe patterns directly encoding the phase derivative. However, for these methods, the measurement of the phase derivative depends on the physical setup of a particular method and hence cannot be generalized.

Accordingly, several methods have been proposed to estimate the phase derivatives from a given fringe pattern without relying on the optical configuration. Various phase-shifting technique based methods [71–73] have been developed for phase derivative estimation, though, their application is limited by the requirement of multiple fringe patterns. A Fourier transform based method [74] was proposed for estimation of the phase derivative. However, due to the global or non-localized nature [75] of the Fourier transform, the method is not suitable to analyze non-stationary signals i.e. fringe patterns with spatially varying phase derivatives. In addition, the method requires unwrapping operation to obtain continuous estimates.

In recent years, the use of space-frequency distributions [76, 77] has emerged as a popular approach in fringe analysis for phase derivative estimation. These distributions have localized nature and provide a joint representation of the signal in space and frequency. In this approach, the phase derivative corresponds to the local or instantaneous frequency in the fringe pattern and is estimated by tracing the spectral energy density peaks or *ridges* of the distribution. Wavelet transform [78, 79] is a well-known space-frequency distribution in fringe analysis, however, its performance is deteriorated in the vicinity of null phase gradients, and ridge detection is highly sensitive to noise [80]. Similarly, Wigner-Ville distribution [77] based method has been proposed for phase derivative estimation, but the accuracy is affected by the interference terms arising due to the quadratic nature of the distribution and usually requires a smoothing operation [81]. Recently, windowed Fourier transform [82] was proposed for phase derivative estimation and has emerged as a popular fringe analysis technique. A major limitation of all these space-frequency distribution based techniques is that they provide information about the first order phase derivative only and are not suitable for direct estimation of higher order derivatives.

1.3 Measurement of slopes and curvature in digital holographic interferometry

In the recent decades, digital holographic interferometry (DHI) [1] has emerged as a popular technique for deformation analysis in the areas of experimental mechanics and non-destructive testing. The major advantages of DHI are non-invasive behavior, whole-

field measurement capability and good measurement resolution. Moreover, the use of a charge-coupled device (CCD) camera as the recording medium removed the need of complex and time-consuming chemical processing steps associated with classical holography. The digitalization of recording and processing of holograms greatly facilitated the applicability of DHI for deformation measurements.

In DHI, for a diffuse object subjected to loading, two holograms are recorded corresponding to the object states before and after deformation. The complex amplitudes of the object wave-fields are obtained from the numerical reconstruction of the holograms using discrete Fresnel transform [83]. The complex amplitude before deformation can be written as,

$$\Gamma_1(x,y) = a_1(x,y)\exp[j\psi_1(x,y)] \tag{1.2}$$

where $a_1(x,y)$ is the amplitude and $\psi_1(x,y)$ is the random phase. Similarly, the complex amplitude after deformation is given as,

$$\Gamma_2(x,y) = a_2(x,y)\exp[j\psi_2(x,y)] \tag{1.3}$$

Subsequently, the reconstructed interference field is computed by multiplying the post-deformation complex amplitude with the conjugate of pre-deformation complex amplitude. In other words, we have

$$\begin{aligned}\Gamma(x,y) &= \Gamma_2(x,y)\Gamma_1^*(x,y)\\ &= a_1(x,y)a_2(x,y)\exp[j(\psi_2(x,y) - \psi_1(x,y))]\end{aligned} \tag{1.4}$$

or

$$\Gamma(x,y) = a(x,y)\exp[j\phi(x,y)] \tag{1.5}$$

with $a(x,y) = a_1(x,y)a_2(x,y)$ and,

$$\phi(x,y) = \psi_2(x,y) - \psi_1(x,y) \tag{1.6}$$

Here, $\phi(x,y)$ is the *interference* phase. When the object is deformed, the displacement is related to the interference phase through the sensitivity vector, which is defined as the difference between the observation and illumination unit vectors [83]. In Fig.1.1, $\vec{\mathbf{d}}$ indicates the displacement vector at a point Q on the diffuse object. The unit vectors along the illumination and observation directions are denoted as $\hat{\mathbf{s}}$ and $\hat{\mathbf{u}}$. The relation between the phase and displacement is given as [83],

$$\phi = \frac{2\pi}{\lambda}\,\vec{\mathbf{d}}\cdot(\hat{\mathbf{u}} - \hat{\mathbf{s}}) \tag{1.7}$$

or equivalently,

$$\phi = \frac{2\pi}{\lambda}\,\vec{\mathbf{d}}\cdot\vec{\mathbf{S}} \tag{1.8}$$
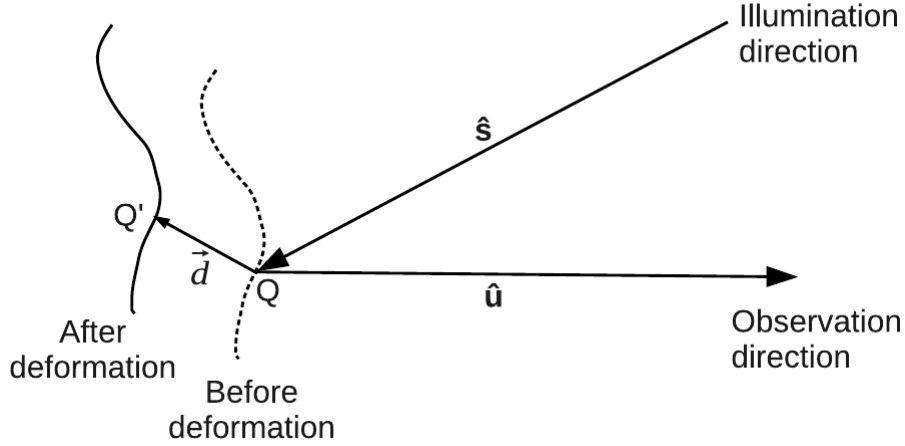
Fig. 1.1. Deformation of the diffuse object

where $\vec{\mathbf{S}} = \hat{\mathbf{u}} - \hat{\mathbf{s}}$ denotes the sensitivity vector and λ is the wavelength. From the above equation, it is clear that the phase depends on the projection of the displacement vector onto the sensitivity vector. As the displacement of the deformed object is related to ϕ, the first and second order displacement derivatives i.e. slope and curvature correspond to the derivatives $\partial\phi/\partial x$ and $\partial^2\phi/\partial x^2$.

For phase derivative estimation in DHI, a prominent approach is digital shearing [84,85] where the sheared reconstructed interference field is superimposed on the original to approximate the phase differentiation operation. Similarly, by successive application of digital shearing, the second order phase derivative has also been estimated [86]. The main drawback of the method is that the performance is severely deteriorated in the presence of noise [79], thereby necessitating the application of filtering operations [87,88]. However, the filtering procedure is a computational overhead and needs to be carefully controlled so as not to smear the dense fringes. In addition, the method also requires an unwrapping operation to obtain continuous estimates.

The techniques described above usually provide information about the displacement derivative along a single dimension i.e. the out-of-plane component or slope only. However, for many practical applications, information about the multi-dimensional i.e. in-plane and out-of-plane displacement derivatives is required for complete characterization of deformation mechanisms. For such measurements, the optical configuration in DHI relies on illuminating the object along different directions [89] resulting in multiple object beams. For each illumination direction, there is an associated sensitivity vector and interference phase. The in-plane and out-of-plane displacements are related to the multiple phases for different directions through the corresponding sensitivity vectors.

Recently, several methods [90–95] have been proposed for multi-dimensional measurements which rely on illuminating the object sequentially by multiple beams i.e. one beam

at a time along different directions. Because of the sequential operation, these methods are unable to simultaneously measure the in-plane and out-of-plane components. In addition, the use of phase-shifting technique in some of these methods requires multiple data frames to be captured, which might be difficult for many practical applications. For simultaneous measurements, methods [89,96–100] relying on multiple reference-object beam pairs have been proposed in DHI. However, usage of multiple reference beams adds complexity to the optical configuration. A major limitation in all these techniques is that only the wrapped estimates of phase are obtained. Hence, to obtain the phase derivatives, additional unwrapping and numerical differentiation operations are required.

1.4 Motivation

It is evident from the previous sections that there is a strong need to develop novel fringe analysis techniques which are capable of estimating phase derivatives from a single fringe pattern with high estimation accuracy, good computational efficiency, strong robustness against noise and non-requirement of unwrapping operation. Additionally, the area of multi-dimensional deformation analysis offers immense scope for developing methods capable of directly estimating multiple phases and derivatives without relying on complex experimental setups, multiple data frames or error-prone unwrapping procedures.

The thesis aims to address these challenges in fringe analysis. Accordingly, the first objective of the thesis is to develop novel methods with the following characteristics:

- Direct estimation of the phase derivative from a single fringe pattern without the need of any unwrapping operation.

- Ability to handle fringe patterns containing rapidly varying phase derivatives.

- High computational efficiency and good robustness against noise.

- Ability to estimate phase derivatives of arbitrary order.

- Applicability in optical techniques such as digital holographic interferometry and fringe projection for the measurement of slopes and curvature, defect detection and temporal evolution studies.

The other objective of the thesis deals with multi-component fringe analysis i.e.

- Development of methods to estimate multiple phases and their derivatives from a single fringe pattern.

- Application of the developed methods in digital holographic interferometry for the simultaneous measurement of in-plane and out-of-plane displacements and their derivatives.

1.5   Outline

The outline of the thesis is as follows:

Chapter 2 presents a pseudo Wigner-Ville distribution (PSWVD) method for direct estimation of the phase derivative without the need of any unwrapping and filtering operations.

Chapter 3 introduces an adaptive windowing technique for the PSWVD method to estimate phase derivatives with rapid variations.

Chapter 4 presents the two-dimensional extension of the PSWVD method for phase derivative estimation. The presence of a two-dimensional window greatly enhances the robustness of the method against noise.

Chapter 5 proposes complex-lag distributions for estimating phase derivatives of arbitrary order.

Chapter 6 highlights some of the applications of the developed methods in digital holographic interferometry and fringe projection.

Chapter 7 introduces the concept of moiré fringes in digital holographic interferometry for multi-dimensional deformation analysis.

Chapter 8 presents a multi-component polynomial phase formulation based approach for estimating multiple phases and their derivatives without requiring any external spatial carrier, filtering and unwrapping operations.

Chapter 9 summarizes the contributions of the thesis and presents the scope of future work.

Chapter 2

Pseudo Wigner-Ville distribution method

2.1 Introduction

As discussed in the previous chapter, reliable estimation of phase derivatives without the need of complex unwrapping and filtering operations is highly desired in spatial fringe analysis. To address this problem, this chapter introduces a pseudo Wigner-Ville distribution based method for the estimation of phase derivatives from a fringe pattern. The method is presented in the context of digital holographic interferometry; however, its generalization to other optical techniques is also discussed.

2.2 Theory

In DHI, the reconstructed interference field is given as,

$$\Gamma(x, y) = a(x, y) \exp[j\phi(x, y)] + \eta(x, y) \quad \forall x, y \in [1, N] \tag{2.1}$$

where $a(x, y)$ is the slow varying amplitude, $\phi(x, y)$ is the interference phase, $\eta(x, y)$ is noise and N is the number of pixels. The first order phase derivative with respect to x is given as,

$$\phi_x(x, y) = \frac{\partial \phi(x, y)}{\partial x} \tag{2.2}$$

For an arbitrary row y, we have,

$$\Gamma(x) = a(x) \exp\left[j\phi(x)\right] + \eta(x) \tag{2.3}$$

To estimate the phase derivative, a pseudo Wigner-Ville distribution [101] is applied. The pseudo Wigner-Ville distribution (PSWVD) is a space-frequency distribution obtained by introducing a lag window in the computation of the ordinary Wigner-Ville distribution (WVD). For better understanding of the two distributions, the WVD for $\Gamma(x)$ is given as,

$$\gamma_1(x, \omega) = \int_{-\infty}^{\infty} \Gamma(x + u/2)\Gamma^*(x - u/2) \exp[-j\omega u] \, \mathrm{d}u \tag{2.4}$$

where '*' denotes the complex conjugate and ω represents the frequency. Using the substitution $\tau = u/2$, we have

$$\gamma_1(x, \omega) = 2 \int_{-\infty}^{\infty} \Gamma(x + \tau)\Gamma^*(x - \tau) \exp[-j2\omega\tau] \, \mathrm{d}\tau \tag{2.5}$$

By introducing a finite length symmetric window function w in the above equation and ignoring the scaling factor in front of the integral, the PSWVD is computed as

$$W(x, \omega) = \int_{-\infty}^{\infty} w(\tau)\Gamma(x + \tau)\Gamma^*(x - \tau) \exp[-j2\omega\tau] \, \mathrm{d}\tau \tag{2.6}$$

The main advantage of using a window is to reduce the interference terms arising due to the quadratic nature of the WVD [101]. Assuming the amplitude variation to be small within the window and neglecting the noise term for the simplicity of analysis, the above equation can be expressed as

$$W(x, \omega) = a^2(x) \int_{-\infty}^{\infty} w(\tau) \exp[j(\phi(x + \tau) - \phi(x - \tau))] \exp[-j2\omega\tau] \, \mathrm{d}\tau \tag{2.7}$$

Within the window region, the phase is assumed to vary slowly and using the second order Taylor series approximation, we have

$$\phi(x + \tau) \approx \phi(x) + \tau \frac{\partial \phi(x)}{\partial x} + \frac{\tau^2}{2} \frac{\partial^2 \phi(x)}{\partial x^2} \tag{2.8}$$

and

$$\phi(x - \tau) \approx \phi(x) - \tau \frac{\partial \phi(x)}{\partial x} + \frac{\tau^2}{2} \frac{\partial^2 \phi(x)}{\partial x^2} \tag{2.9}$$

Using these approximations, Eq.2.7 is modified as,

$$W(x, \omega) = a^2(x) \int_{-\infty}^{\infty} w(\tau) \exp[j2\phi_x(x)\tau] \exp[-j2\omega\tau] \, \mathrm{d}\tau \tag{2.10}$$

where $\phi_x(x) = \partial\phi(x)/\partial x$. In principle, the above equation contains the Fourier transform of the window $w(\tau)$ modulated by the term $\exp[j2\phi_x(x)\tau]$. Hence, denoting the Fourier

transform of the window function as $\hat{w}(\omega)$ and using the frequency shifting property of Fourier transform, we have

$$W(x,\omega) = a^2(x)\hat{w}(2\omega - 2\phi_x(x)) \tag{2.11}$$

Since the window function is chosen to have a low pass behavior, $W(x,\omega)$ is maximum for $\hat{w}(0)$ i.e. when $\omega = \phi_x(x)$. Hence, the phase derivative ϕ_x can be obtained by tracing the peak of the PSWVD. In other words, we have

$$\phi_x(x) = \arg\max_{\omega} W(x,\omega) \tag{2.12}$$

This equation provides the phase derivative estimate for a given row y. The above procedure can be applied for all rows $y \in [1, N]$ to estimate the overall phase derivative $\phi_x(x, y)$ for the entire fringe pattern.

In PSWVD, the presence of a window plays an important role for phase derivative estimation since the second order or quadratic approximation of the phase as in Eq.(2.8) and Eq.(2.9) is reasonably valid in a local region defined by the window. On the contrary, the WVD makes this assumption over the entire length of the signal and hence, the applicability of WVD is limited to quadratic phase signals only. Similarly, the popular windowed Fourier ridges (WFR) technique [27] and wavelet transform method [78] for phase derivative estimation assume a linear approximation of the phase within the window region [102]. So comparatively, the PSWVD offers a better technique for accurate phase derivative estimation.

2.3 Simulation Analysis

To show the superior performance of the PSWVD as compared to WVD for phase derivative estimation, signals of the following form were simulated,

$$\Gamma(x) = \exp[j\phi(x)] \tag{2.13}$$

with the phase $\phi(x)$ as a polynomial of third (cubic) and fourth (quartic) orders. The cubic phase is shown in Fig.2.1(a). For this case, the original vs the estimated phase derivatives using the WVD and PSWVD techniques is shown in Fig.2.1(c). The corresponding estimation errors using the two techniques are shown in Fig.2.1(e). Similarly, for the quartic phase as shown in Fig.2.1(b), the original and the estimated phase derivatives using the WVD and PSWVD techniques are shown in Fig.2.1(d). The corresponding estimation errors for the quartic case using the two techniques are shown in Fig.2.1(f). From Fig.2.1, it is evident that the accuracy of the WVD technique for phase derivative estimation is lower for cubic or higher order phase signals as compared to the PSWVD.
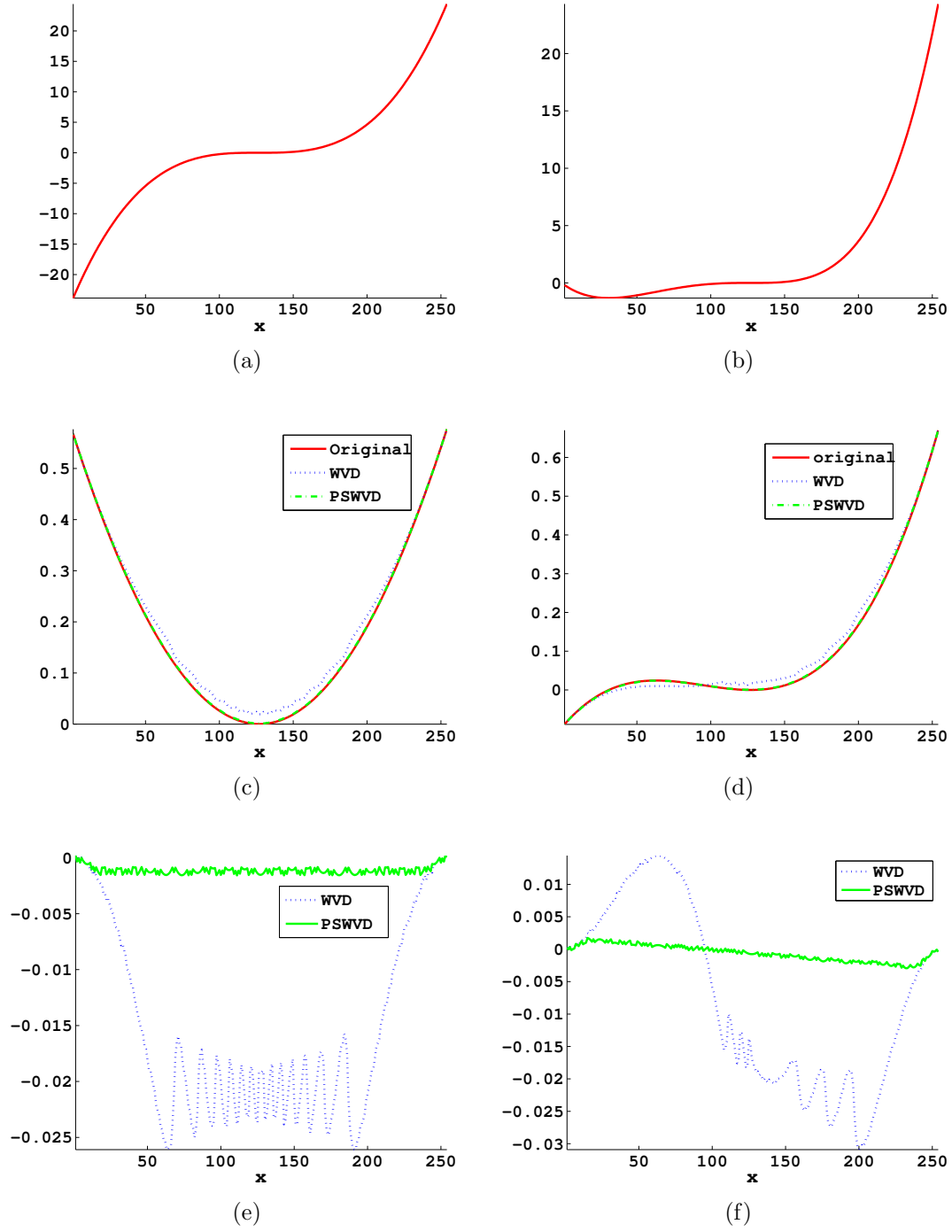
Fig. 2.1. (a) Cubic phase in radians. (b) Quartic phase in radians. (c) Original vs estimated phase derivatives using WVD and PSWVD in radians/pixel for the cubic phase. (d) Original vs estimated phase derivatives using WVD and PSWVD in radians/pixel for the quartic phase. (e) Estimation error in radians/pixel using WVD and PSWVD for the cubic phase. (f) Estimation error in radians/pixel using WVD and PSWVD for the quartic phase.

12

(a)

(b)

(c)

(d)

(e)

(f)
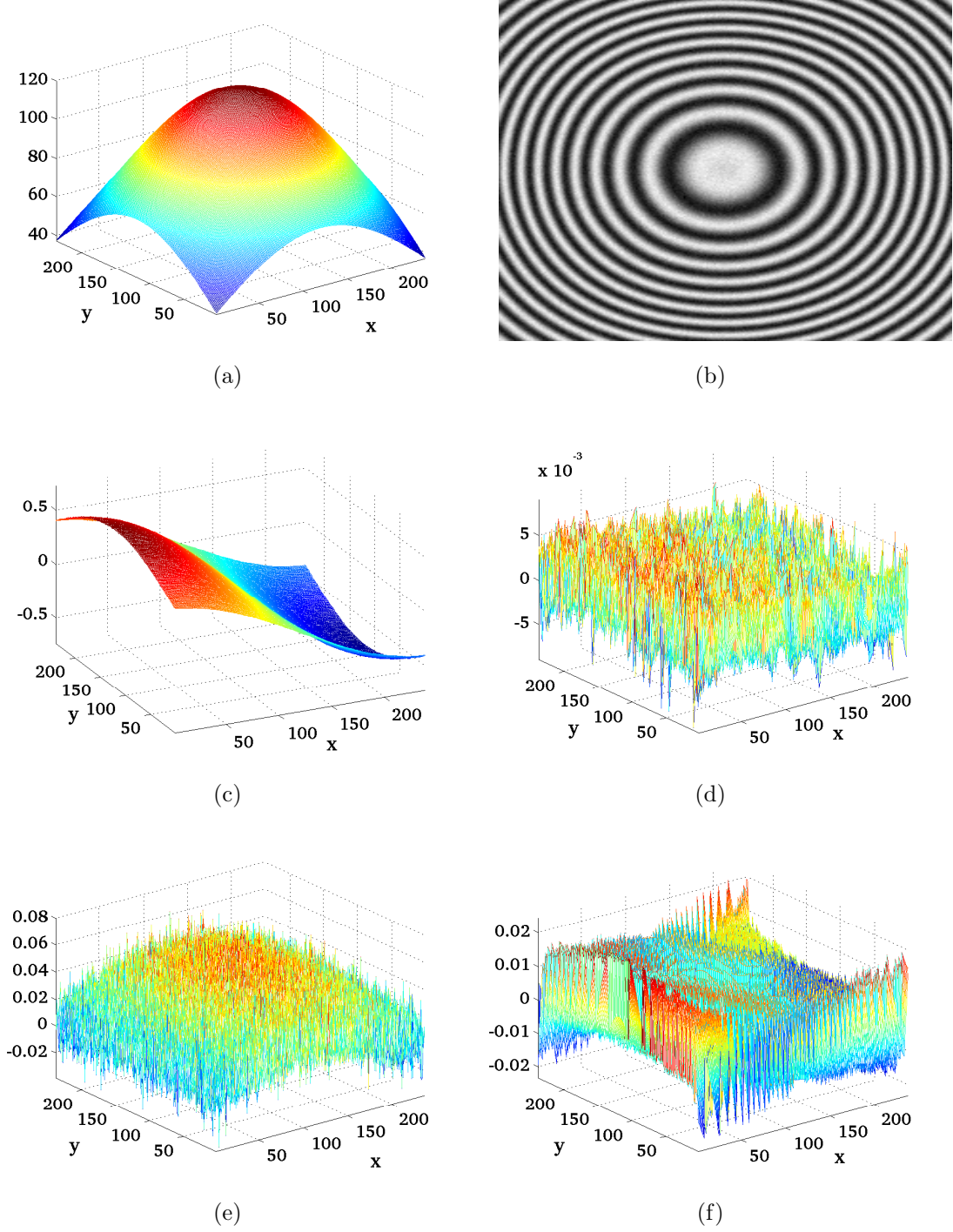
Fig. 2.2. (a) Original phase $\phi(x, y)$ in radians. (b) Fringe pattern. (c) Estimated phase derivative in radians/pixel. (d) Phase derivative estimation error in radians/pixel using 1D-PSWVD method. (e) Phase derivative estimation error in radians/pixel using digital shearing method. (f) Phase derivative estimation error in radians/pixel using WFR method.

13

	Method	RMSE in radians/pixel	Time in seconds
1	PSWVD	0.0023	4.5
2	Digital shearing	0.0151	16.2
3	WFR	0.0083	195.3

Table 2.1. Performance of various phase derivative estimation methods

To analyze the proposed method for phase derivative estimation from fringe patterns, a complex reconstructed interference field signal (size 256×256 pixels) was simulated in MATLAB (version 7.8.0) as

$$\Gamma(x, y) = \exp[j\phi(x, y)] \tag{2.14}$$

and additive white Gaussian noise was added at signal-to-noise-ratio (SNR) of 20 dB using MATLAB's 'awgn' function. The original phase $\phi(x, y)$ is shown in Fig.2.2(a). The real part of $\Gamma(x, y)$ constitutes the fringe pattern as shown in Fig.2.2(b). The estimated phase derivative using the proposed method and the corresponding estimation error are shown in Fig.2.2(c) and Fig.2.2(d). In the method, a Gaussian window of length 33 samples was applied using the MATLAB's 'gausswin' function.

For comparison, the phase derivative was also estimated using the state-of-the-art digital shearing and WFR techniques. For the digital shearing technique, the unwrapping operation was performed using the popular Goldstein's unwrapping algorithm [35]. Also, the various parameters required for the implementation of the WFR technique [82] were selected as wxh = wyh = 0.8, wxl = wyl = -0.8, wxi = wyi = 0.025 and $\sigma_x = \sigma_y = 10$. The phase derivative estimation errors using the digital shearing and WFR techniques are shown in Fig.2.2(e) and Fig.2.2(f). Similarly, the root mean square error (RMSE) in radians/pixel and the computational time in seconds for the PSWVD, digital shearing and WFR techniques are shown in Table 2.1. For the analysis, the pixels near the borders of the fringe pattern were neglected to ignore the errors at the edges.

From Fig.2.2 and Table 2.1, it is clear that the proposed PSWVD based method for phase derivative estimation performs superiorly, when compared to the popular digital shearing and WFR techniques in terms of estimation accuracy and computational efficiency. In addition, when compared to the digital shearing approach, the proposed method provides direct estimates of the phase derivative without the need of any unwrapping operation.

2.4   Experimental Results

To test the practical applicability of the proposed method, a DHI experiment was conducted where a circularly clamped diffuse object (6 *cm* in diameter) was deformed by external loading. The schematic (not drawn to scale) of the off-axis DHI setup is shown in Fig.2.3. A SONY XCL-U1000 CCD camera (1600×1200 pixels), located at a distance of
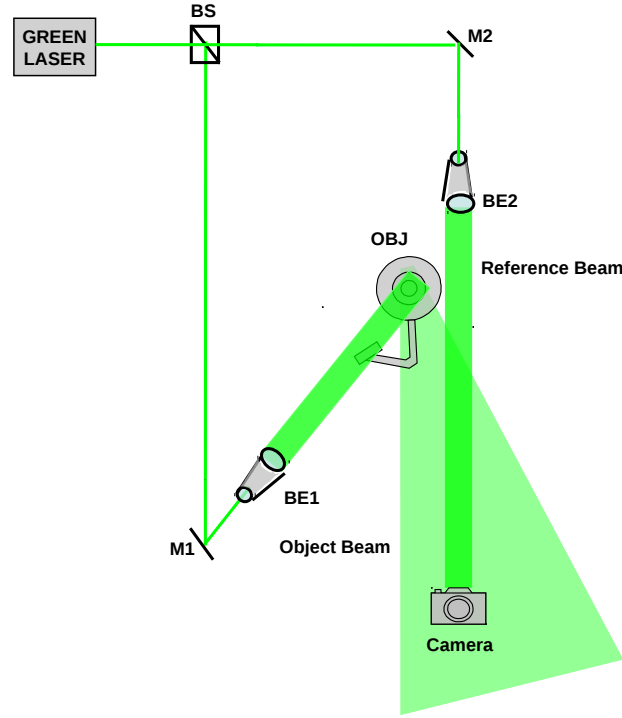
Fig. 2.3. DHI schematic (BS: Beam Splitter, BE: Beam Expander, M: Mirror, OBJ: Diffuse object)

110 cm from the object was used for recording the holograms formed by the superposition of the reference and object beams.

Two digital holograms were recorded by illuminating the object with a Coherent Verdi laser (532 nm) for different object states i.e. before and after loading. The digital hologram recorded before loading the object is shown in Fig.2.4(a). Numerical reconstruction of the hologram was performed using discrete Fresnel transform [83] to obtain the complex amplitudes or wave-fields. The intensity of the complex wave-field obtained after the numerical reconstruction of the hologram is shown in Fig.2.4(b). Since these holograms are recorded in an off-axis configuration, the real and virtual reconstructions of the object and the undiffracted pattern are separated, as shown in Fig.2.4(b).

For the analysis, a small region of interest was selected from the virtual image. The reconstructed interference field was obtained by multiplying the post-deformation complex amplitude with the conjugate of pre-deformation complex amplitude. The experimental fringe pattern i.e. the real part of the reconstructed interference field is shown in Fig.2.4(c). Applying the proposed method, the estimated phase derivative is shown in Fig.2.4(d). The experimental results validate the practical applicability of the proposed method.

15
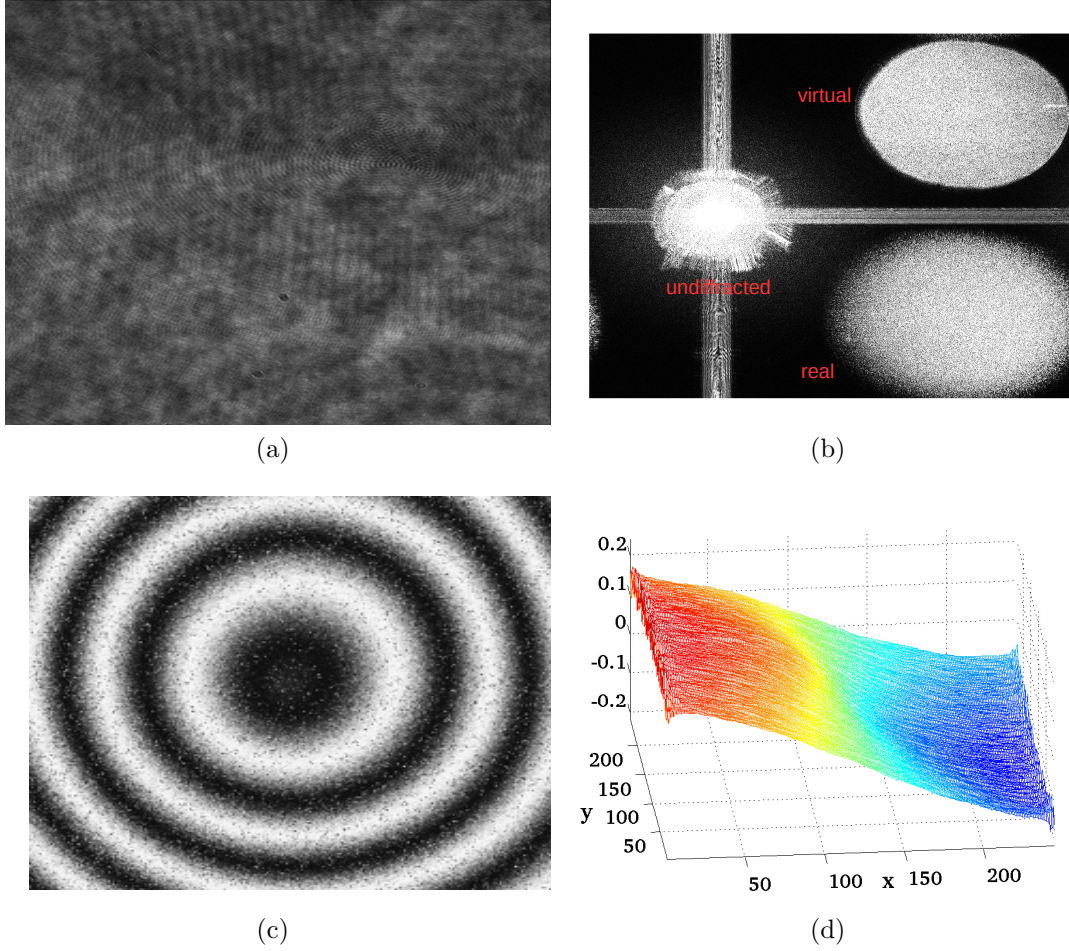
Fig. 2.4. (a) Recorded hologram. (b) Intensity obtained after numerical reconstruction. (c) Experimental fringe pattern. (d) Estimated phase derivative in radians/pixel.

2.5 Extension to other interferometric techniques

Though the method is presented in the context of DHI, its applicability can be extended to other optical interferometric techniques such as electronic speckle pattern interferometry and classical holographic interferometry. In these techniques, the obtained fringe pattern is of the following form,

$$I(x, y) = I_0(x, y) + a(x, y) \cos[\phi(x, y)] \tag{2.15}$$

where $I(x, y)$ is the fringe intensity, $I_0(x, y)$ is the background intensity, $a(x, y)$ is the fringe amplitude and $\phi(x, y)$ is the interference phase. Using a normalization operation [103] and real to analytic signal conversion [104] in presence of a carrier, a complex signal of the following form can be obtained

$$\Gamma(x, y) = \exp[j\phi(x, y)] \tag{2.16}$$

16

which is similar to the one in Eq.(2.1). Subsequently, the proposed method can be applied in the same manner as discussed above.

2.6 Summary

A pseudo Wigner-Ville distribution based method was introduced for the direct estimation of the phase derivative from fringe patterns. The main advantages of the proposed method are estimation accuracy, the ability to estimate phase derivatives without the need of any unwrapping operations and high computational efficiency. Simulation and experimental results presented in the chapter demonstrate the potential of the proposed method.

Chapter 3

Adaptive windowing method

3.1   Introduction

For phase derivative estimation using space-frequency distributions, the choice of window length plays an important role [102]. For a rapidly varying phase derivative, the small window provides good estimation accuracy, but is strongly affected by noise. The converse is true for a large window. Consequently, for estimating phase derivatives with rapid variations, window size selection becomes a challenging issue. The chapter presents an adaptive windowing technique to address this problem.

3.2   Theory

Using Eq.2.1, the reconstructed interference field in DHI is given as,

$$\Gamma(x, y) = a(x, y) \exp[j\phi(x, y)] + \eta(x, y) \tag{3.1}$$

where $\eta(x, y)$ represents the noise, assumed to be zero mean additive white Gaussian noise. For a given row y, Eq.(3.1) can be written as

$$\Gamma(x) = a(x) \exp[j\phi(x)] + \eta(x) \tag{3.2}$$

The phase derivative with respect to x is given as,

$$\omega(x) = \frac{\partial\phi(x)}{\partial x} \tag{3.3}$$

From chapter 2, the PSWVD of $\Gamma(x)$ is given as

$$W(x, \omega) = \sum_{\tau=-\infty}^{\infty} w_h(\tau)\Gamma(x + \tau)\Gamma^*(x - \tau) \exp[-j2\omega\tau] \tag{3.4}$$

where $w_h(x)$ denotes a real symmetric window. For the analysis, we used a Gaussian window,

$$w_h(x) = \frac{1}{\sqrt{2\pi l^2}} \exp\left[-\frac{x^2}{2l^2}\right] \quad \forall\, x \in \left[-\frac{l}{2}, \frac{l}{2}\right] \tag{3.5}$$

with length $h = l + 1$.

The phase derivative estimate $\hat{\omega}_h(x)$ at any point x corresponds to the frequency at which $W(x, \omega)$ becomes maximum. In other words,

$$\hat{\omega}_h(x) = \arg\max_\omega W(x, \omega) \tag{3.6}$$

Since the noise is random, the phase derivative estimate $\hat{\omega}_h(x)$ can be treated as a random variable. Accordingly, the bias B, variance σ^2 and mean square error MSE for the estimate are given as,

$$B = E[\omega(x) - \hat{\omega}_h(x)] \tag{3.7}$$

$$\sigma^2 = E[(\hat{\omega}_h(x) - E[\hat{\omega}_h(x)])^2] \tag{3.8}$$

$$MSE = E[(\omega(x) - \hat{\omega}_h(x))^2] \tag{3.9}$$

and E denotes the expectation operation. The MSE is dependent on the bias and variance as shown below:

$$
\begin{aligned}
MSE &= E\left[(\omega(x) - \hat{\omega}_h(x))^2\right] \\
&= E\left[((\omega(x) - E[\hat{\omega}_h(x)]) + (E[\hat{\omega}_h(x)] - \hat{\omega}_h(x)))^2\right] \\
&= E\left[(\omega(x) - E[\hat{\omega}_h(x)])^2\right] + E\left[(\hat{\omega}_h(x) - E[\hat{\omega}_h(x)])^2\right] \\
&\quad + 2E\left[(\omega(x) - E[\hat{\omega}_h(x)])(E[\hat{\omega}_h(x)] - \hat{\omega}_h(x))\right] \\
&= B^2 + \sigma^2 + 2E\left[\omega(x)E[\hat{\omega}_h(x)] - \omega(x)\hat{\omega}_h(x)\right] \\
&\quad - 2E\left[(E[\hat{\omega}_h(x)])^2 - E[\hat{\omega}_h(x)]\hat{\omega}_h(x)\right]
\end{aligned}
$$

Now, $\omega(x)$ and $E[\hat{\omega}_h(x)]$ are deterministic. Since the expectation operation over a deterministic variable yields the same variable, the above equation is modified as

$$
\begin{aligned}
MSE &= B^2 + \sigma^2 + 2\omega(x)E[\hat{\omega}_h(x)] - 2\omega(x)E[\hat{\omega}_h(x)] \\
&\quad - 2(E[\hat{\omega}_h(x)])^2 + 2E[\hat{\omega}_h(x)]E[\hat{\omega}_h(x)] \\
&= B^2 + \sigma^2 \\
&= bias^2 + variance
\end{aligned}
$$

For PSWVD, the bias and variance depend on the window length h and are given as [105]

$$B(h) = \sum_{s=1}^{\infty} h^{2s} b_s \omega^{(2s)}(x) \tag{3.10}$$

$$\sigma^2(h) = \frac{\sigma_\epsilon^2}{2|a|^2} \left(1 + \frac{\sigma_\epsilon^2}{2|a|^2}\right) \frac{E_1}{h^3 F_1^2} \tag{3.11}$$

$$MSE(h) = B^2(h) + \sigma^2(h) \tag{3.12}$$

where σ_ϵ^2 is the variance of the noise and

$$E_1 = \int_{-\frac{1}{2}}^{\frac{1}{2}} w^2(x) x^2 \, dx \tag{3.13}$$

$$F_1 = \int_{-\frac{1}{2}}^{\frac{1}{2}} w(x) x^2 \, dx \tag{3.14}$$

$$b_s = \frac{1}{(2s+1)! \, F_1} \int_{-\frac{1}{2}}^{\frac{1}{2}} w(x) x^{2s+2} \, dx \tag{3.15}$$

$$w(x) = \frac{1}{\sqrt{2\pi}} \exp\left[-\frac{x^2}{2}\right] \tag{3.16}$$

For Eq.(3.11), the noise variance and signal amplitude estimates i.e. $\hat{\sigma}_\epsilon^2$ and $\hat{a}$ are evaluated using moments based estimator [106] and given as,

$$\hat{a}^2 = \left\{ \left| 2\left[\frac{1}{N}\sum_{x=1}^{N} |\Gamma(x)|^2\right]^2 - \frac{1}{N}\sum_{x=1}^{N} |\Gamma(x)|^4 \right| \right\}^{\frac{1}{2}} \tag{3.17}$$

$$\hat{\sigma}_\epsilon^2 = \left| \sum_{x=1}^{N} \frac{|\Gamma(x)|^2}{N} - \left\{ \left| 2\left[\sum_{x=1}^{N} \frac{|\Gamma(x)|^2}{N}\right]^2 - \sum_{x=1}^{N} \frac{|\Gamma(x)|^4}{N} \right| \right\}^{\frac{1}{2}} \right| \tag{3.18}$$

It is clear from Eq.(3.10) and Eq.(3.11) that with increasing window length h, the bias of phase derivative estimate increases, whereas the variance is reduced. For a better understanding of this feature, consider the random nature of the estimate. Since it is a random variable, we can assign to it a probability density function (pdf) characterized by a mean value and variance. The bias indicates the closeness of the estimate's mean from the true value, whereas the variance quantifies the spread about the estimate's mean.

If the phase derivative varies rapidly, the quadratic phase approximation in Eq.(2.8) and Eq.(2.9) for the PSWVD method would be valid only for a small window. Hence, for small window lengths, the estimated value for the phase derivative is close to the true value and this leads to a smaller bias. However, a small window captures fewer samples for the evaluation of the PSWVD and consequently, the influence of noise on phase derivative estimation is high. This causes a large variance of the estimate for a small window. Conversely, for a large window, the bias is high since the quadratic phase approximation
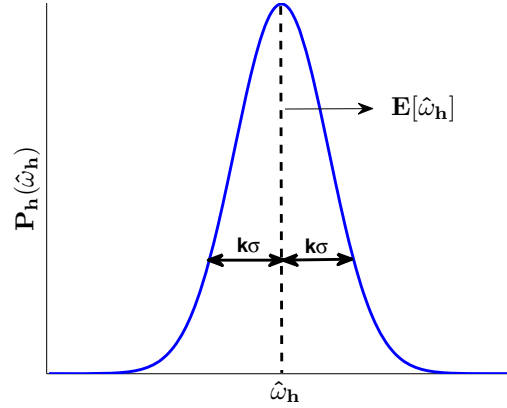
Fig. 3.1. Probability density function for phase derivative estimate

suffers in the vicinity of rapid variations. However, the variance is low, since a large window captures more data samples and consequently provides data smoothing, which leads to better robustness against noise.

From Eq.(3.12), it is clear that the mean square error MSE depends on both bias and variance and hence, any method to minimize it must take both the bias and variance into consideration. For small windows, variance is dominant and for large windows, bias is dominant in the calculation of MSE. So there exists a *bias-variance* trade-off, which necessitates the selection of an optimum window to minimize MSE.

To determine the optimum window length, the intersection of confidence intervals (ICI) algorithm [105] is applied. We assume an arbitrary pdf $P_h(\hat{\omega}_h)$ for the random variable $\hat{\omega}_h$ for a given h as shown in Fig.3.1. The area under the pdf curve for the region $\hat{\omega}_h(x) \in [E[\hat{\omega}_h(x)] - k\sigma(h), E[\hat{\omega}_h(x)] + k\sigma(h)]$ gives the probability $P_k = P(|\hat{\omega}_h(x) - E[\hat{\omega}_h(x)]| \leq k\sigma(h))$. For the random variable $\hat{\omega}_h$, we have

$$
\begin{aligned}
|\hat{\omega}_h(x) - E[\hat{\omega}_h(x)]| &= |\hat{\omega}_h(x) - \omega(x) - (E[\hat{\omega}_h(x)] - \omega(x))| \\
&\geq |\hat{\omega}_h(x) - \omega(x)| - |\omega(x) - E[\hat{\omega}_h(x)]| \\
&\geq |\hat{\omega}_h(x) - \omega(x)| - |bias|
\end{aligned}
\tag{3.19}
$$

Hence for a given k, with a probability P_k,

$$
|\hat{\omega}_h(x) - \omega(x)| - |bias| \leq k\sigma(h)
\tag{3.20}
$$

For small h, when bias is small and variance is dominant, we have

$$
|bias| \leq k\sigma(h)
\tag{3.21}
$$

Hence Eq.(3.20) can be written as

$$
|\hat{\omega}_h(x) - \omega(x)| \leq 2k\sigma(h)
\tag{3.22}
$$

or equivalently,

$$\hat{\omega}_h(x) - 2k\sigma(h) \le \omega(x) \le \hat{\omega}_h(x) + 2k\sigma(h) \tag{3.23}$$

The above equation provides the lower and upper bounds in which the true phase derivative $\omega(x)$ lies. These bounds constitute the confidence interval $D_s = [L_s, U_s]$ where $L_s = \hat{\omega}_h(x) - 2k\sigma(h)$ and $U_s = \hat{\omega}_h(x) + 2k\sigma(h)$ for a particular $h = h_s$. If Eq.(3.21) is true for two consecutive window lengths h_{s-1} and h_s, then $\omega(x)$ will lie in both the consecutive confidence intervals D_{s-1} and D_s. Mathematically, we have

$$\hat{\omega}_{h_{s-1}}(x) - 2k\sigma(h_{s-1}) \le \omega(x) \le \hat{\omega}_{h_{s-1}}(x) + 2k\sigma(h_{s-1}) \tag{3.24}$$

and

$$\hat{\omega}_{h_s}(x) - 2k\sigma(h_s) \le \omega(x) \le \hat{\omega}_{h_s}(x) + 2k\sigma(h_s) \tag{3.25}$$

Hence, from above inequalities, the condition for intersection of confidence intervals can be given as,

$$|\hat{\omega}_{h_s}(x) - \hat{\omega}_{h_{s-1}}(x)| \le 2k[\sigma(h_s) + \sigma(h_{s-1})] \tag{3.26}$$

For an increasing sequence of h_s i.e. $h_1 < h_2 < h_3 \cdots$ etc., beyond a particular window length say h_{opt}, the intersection between confidence intervals will be null i.e. $D_{s-1} \cap D_s = \phi$ for $h_s > h_{opt}$. Hence h_{opt} determines the largest window length for which Eq.(3.21) is still satisfied and corresponds to a bias-variance compromise where bias and standard deviation are of the same order and MSE will be minimum.

So the adaptive windowing scheme is given as,

1. Select a set of different window lengths $H = h_s | h_1 < h_2 \cdots < h_n$ for a particular pixel x belonging to a given row y.

2. For each h_s, estimate the phase derivative $\hat{\omega}_{h_s}$ and variance $\sigma^2(h_s)$ from Eq.(3.6) and Eq.(3.11).

3. Calculate the confidence interval D_s using Eq.(3.23).

4. The optimal window length h_{opt} is found corresponding to the largest s for which $D_{s-1} \cap D_s \ne \phi$ is satisfied i.e. Eq.(3.26) is still valid.

5. The optimal phase derivative estimate is the one corresponding to the optimal window length h_{opt}.

6. Repeat the above steps for all pixels $x \in [1, N]$ and subsequently for all rows $y \in [1, N]$.

	Window	RMSE in radians/pixel
1	Large	0.2104
2	Small	0.0367
3	Adaptive	0.0186

Table 3.1. Performance of PSWVD method for different windows

3.3   Simulation Analysis

To analyze the adaptive windowing technique, a complex signal as in Eq.(3.2) was simulated in MATLAB. Additive white Gaussian noise was added to the signal at an SNR of 15 dB using MATLAB's 'awgn' function. For the ICI algorithm, we used $k = 1.75$ and the set of window lengths were selected as $H = [5, 9, 13, \cdots, 101]$. The performance of the PSWVD method for phase derivative estimation in presence of a small ($h_s = 5$), large ($h_s = 101$) and adaptive window is shown in Fig.3.2(a), Fig.3.2(b) and Fig.3.2(c). The absolute phase derivative estimation errors in radians/pixel for the three cases are shown in Fig.3.2(d).

From the figures, it is evident that the estimation error is high for the small window in slowly varying regions of the phase derivative due to the influence of noise. On the other hand, a large window performs poorly in regions with rapid variations. The optimum performance is obtained for an adaptive window. To minimize the bias-variance trade-off, the adaptive windowing technique selects the suitable window length as shown in Fig.3.2(e). The root mean square errors (RMSEs) in radians/pixel for phase derivative estimation in the presence of the large, small and adaptive windows are shown in Table 3.1. These results highlight the benefit of using an adaptive window instead of a fixed window for estimating rapidly varying phase derivatives.

To demonstrate the validity of the proposed method for fringe analysis, the complex reconstructed interference field (256×256 pixels) was simulated using Eq.(3.1) at an SNR of 20 dB. The corresponding fringe pattern is shown in Fig.3.3(a). The original phase derivative in radians/pixel is shown in Fig.3.3(b). The phase derivative exhibits the characteristics of a triangular pulse train along x and shows rapid variations.

The PSWVD method was applied in conjunction with the proposed adaptive windowing technique for estimating the phase derivative. For a particular row $y = 64$, the original vs the estimated phase derivative in radians/pixel is shown in Fig.3.3(c). It is evident from the figure that the method is able to track the rapid variations in the phase derivative. The estimated phase derivative in radians/pixel for the entire fringe pattern using the proposed method is shown in Fig.3.3(d). The corresponding estimation error in radians/pixel is shown in Fig.3.3(e). The pixels near the edges of the fringe pattern were ignored for the analysis to neglect the errors at the boundaries. The RMSE for phase derivative estimation was found to be 0.0097 radians/pixel and the total computational time required for phase derivative estimation was about 105 seconds. The results clearly substantiate
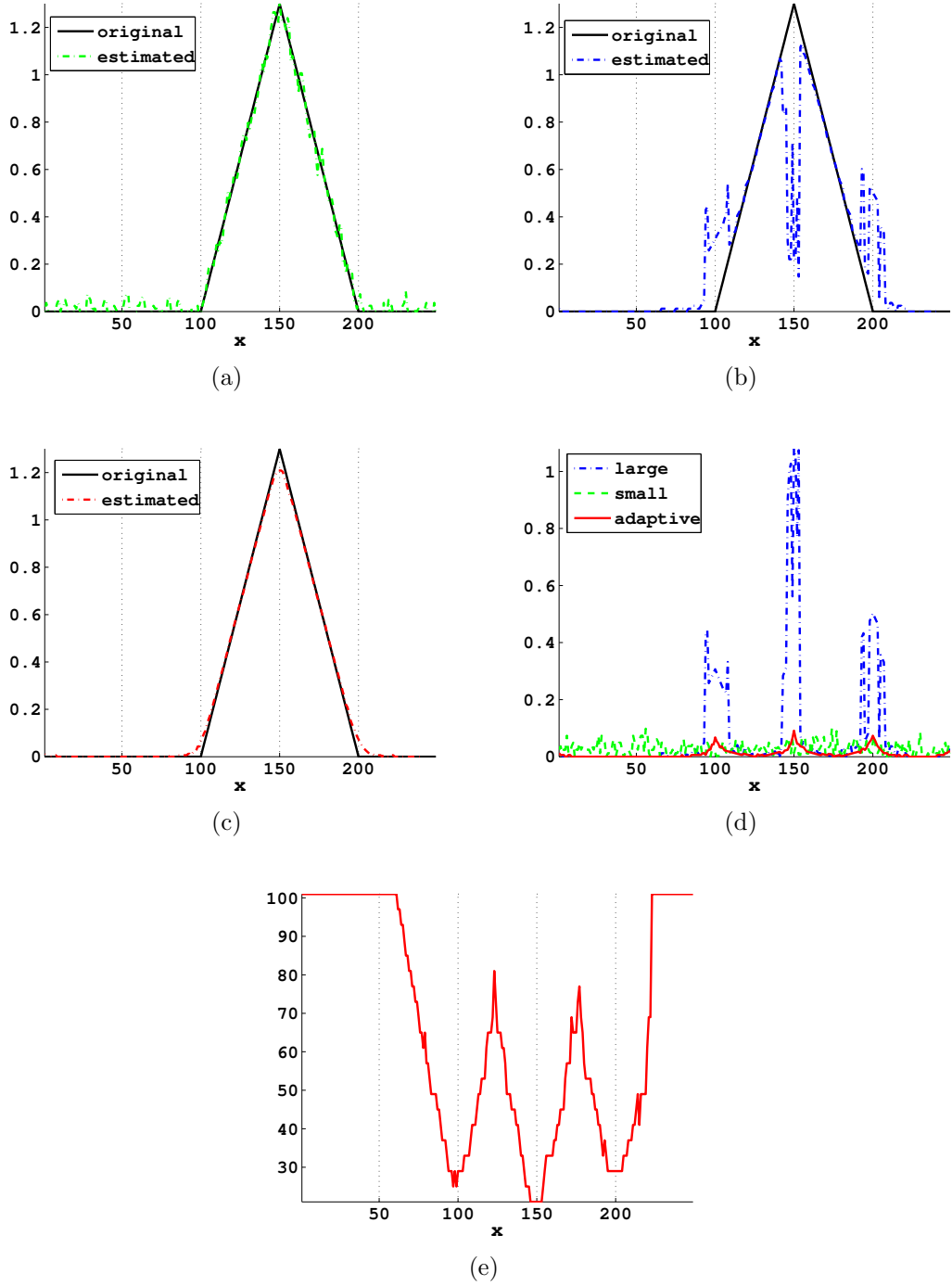
Fig. 3.2. Original vs estimated phase derivative in radians/pixel for (a) small window with $h_s = 5$, (b) large window with $h_s = 101$ and (c) adaptive window. (d) Absolute phase derivative estimation errors in radians/pixel for the small, large and adaptive windows. (e) Optimal window size h_{opt}.

25
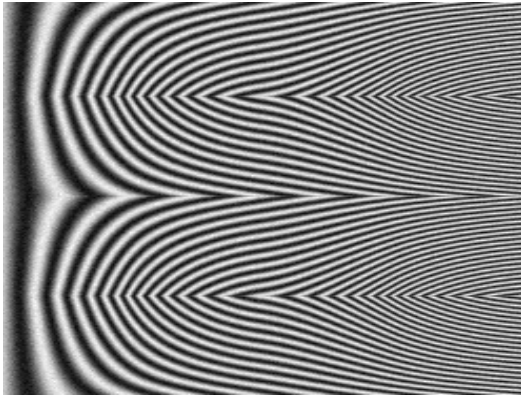
(a)
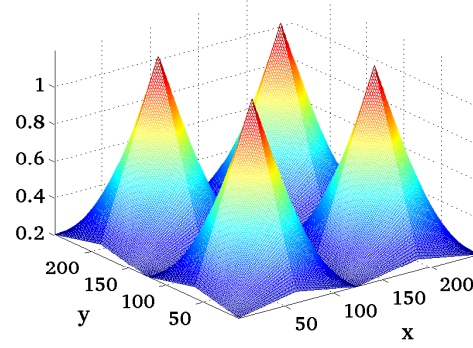
(b)
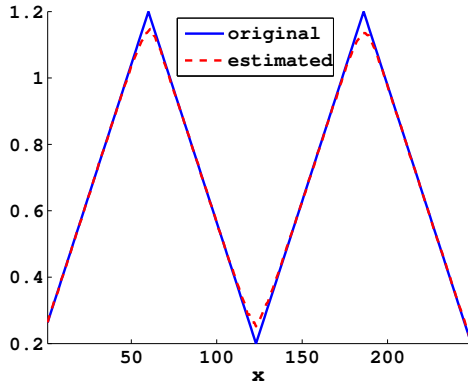
(c)
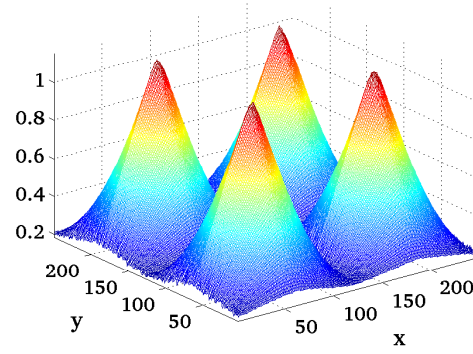
(d)
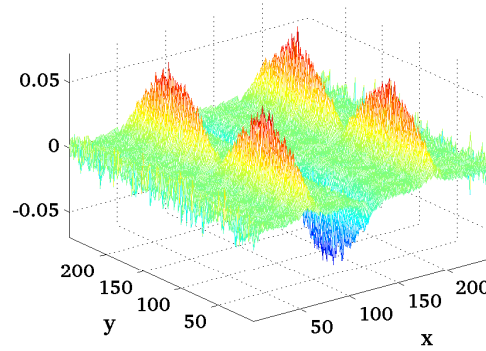
(e)

Fig. 3.3. (a) Simulated fringe pattern. (b) Original phase derivative in radians/pixel. (c) Original and estimated phase derivatives in radians/pixel for row $y = 64$. (d) Estimated phase derivative for the entire fringe pattern in radians/pixel. (e) Estimation error in radians/pixel.

26

the applicability of the proposed method in fringe analysis.

3.4   Summary

The chapter introduced an adaptive windowing technique for the PSWVD method to enable reliable estimation of the phase derivatives with rapid variations. The technique relies on resolving the bias-variance trade-off and provides the optimum window length for phase derivative estimation using the intersection of confidence intervals algorithm. The potential of the proposed technique is demonstrated through the numerical simulation results.

Chapter 4

Two-dimensional pseudo Wigner-Ville distribution method

4.1   Introduction

For practical applications in DHI, a highly desired characteristic of any fringe analysis method is the ability to reliably estimate phase derivatives from a fringe pattern affected by noise. This chapter introduces the two-dimensional (2D) extension of the PSWVD method for phase derivative estimation from noisy fringes. Due to the presence of a 2D window, the robustness of the PSWVD against noise is significantly enhanced.

4.2   Theory

Using Eq.(2.1), the reconstructed interference field in DHI is given as,

$$\Gamma(x,y) = a(x,y)\exp[j\phi(x,y)] + \eta(x,y) \tag{4.1}$$

The 2D Wigner-Ville distribution corresponding to $\Gamma(x,y)$ is given as [107]

$$\gamma_1(x,y,\omega_1,\omega_2) = \int_{-\infty}^{\infty}\int_{-\infty}^{\infty}\Gamma\left(x+\frac{u_1}{2}, y+\frac{u_2}{2}\right)\Gamma^*\left(x-\frac{u_1}{2}, y-\frac{u_2}{2}\right)$$
$$\exp[-j(\omega_1 u_1 + \omega_2 u_2)]\mathrm{d}u_1\mathrm{d}u_2 \tag{4.2}$$

where '*' denotes the complex conjugate. By introducing a two-dimensional window function, the resulting two-dimensional pseudo Wigner-Ville distribution (2D-PSWVD) can be equivalently written as,

$$\gamma(x, y, \omega_1, \omega_2) = \int_{-\infty}^{\infty} \int_{-\infty}^{\infty} w(\tau_1, \tau_2) \Gamma(x + \tau_1, y + \tau_2) \Gamma^*(x - \tau_1, y - \tau_2)$$
$$\exp[-2j(\omega_1\tau_1 + \omega_2\tau_2)]\mathrm{d}\tau_1\mathrm{d}\tau_2 \tag{4.3}$$

where $w(\tau_1, \tau_2)$ is a real symmetric window usually having a low-pass behavior. From above equation, it is clear that 2D-PSWVD maps the reconstructed interference field $\Gamma(x, y)$ in spatial domain to $\gamma(x, y, \omega_1, \omega_2)$, thereby providing a joint space-frequency representation. For simplicity of analysis, the amplitude term within the window region is assumed constant and neglected along with the noise term. Hence from Eq.(4.1) and Eq.(4.3), we have

$$\gamma(x, y, \omega_1, \omega_2) = \int_{-\infty}^{\infty} \int_{-\infty}^{\infty} w(\tau_1, \tau_2) \exp[j(\phi(x + \tau_1, y + \tau_2) - \phi(x - \tau_1, y - \tau_2))]$$
$$\exp[-j(2\omega_1\tau_1 + 2\omega_2\tau_2)]\mathrm{d}\tau_1\mathrm{d}\tau_2 \tag{4.4}$$

Assuming that the phase $\phi(x, y)$ is slowly varying in the neighborhood of (x, y) and using Taylor series expansion up to second order, we have the following approximations,

$$\phi(x + \tau_1, y + \tau_2) \approx \phi(x, y) + \phi_x(x, y)\tau_1 + \phi_y(x, y)\tau_2$$
$$+ \frac{1}{2}[\phi_{xx}(x, y)\tau_1^2 + 2\tau_1\tau_2\phi_{xy}(x, y) + \phi_{yy}(x, y)\tau_2^2] \tag{4.5}$$

$$\phi(x - \tau_1, y - \tau_2) \approx \phi(x, y) - \phi_x(x, y)\tau_1 - \phi_y(x, y)\tau_2$$
$$+ \frac{1}{2}[\phi_{xx}(x, y)\tau_1^2 + 2\tau_1\tau_2\phi_{xy}(x, y) + \phi_{yy}(x, y)\tau_2^2] \tag{4.6}$$

$$\phi(x + \tau_1, y + \tau_2) - \phi(x - \tau_1, y - \tau_2) \approx 2[\phi_x(x, y)\tau_1 + \phi_y(x, y)\tau_2] \tag{4.7}$$

where

$$\phi_x(x, y) = \frac{\partial\phi(x, y)}{\partial x}$$
$$\phi_{xx}(x, y) = \frac{\partial^2\phi(x, y)}{\partial x^2}$$
$$\phi_{xy}(x, y) = \frac{\partial^2\phi(x, y)}{\partial x\partial y}$$
$$\phi_y(x, y) = \frac{\partial\phi(x, y)}{\partial y}$$
$$\phi_{yy}(x, y) = \frac{\partial^2\phi(x, y)}{\partial y^2}$$

Using these approximations in Eq.(4.4), we have

$$\gamma(x, y, \omega_1, \omega_2) = \int_{-\infty}^{\infty} \int_{-\infty}^{\infty} w(\tau_1, \tau_2) \exp[2j(\phi_x(x, y)\tau_1 + \phi_y(x, y)\tau_2)]$$
$$\exp[-2j(\omega_1\tau_1 + \omega_2\tau_2)]\mathrm{d}\tau_1\mathrm{d}\tau_2 \tag{4.8}$$

From the above equation, it is clear that $\gamma(x, y, \omega_1, \omega_2)$ is essentially the 2D Fourier transform of $w(\tau_1, \tau_2)$ modulated by the term $\exp[2j(\phi_x(x, y)\tau_1 + \phi_y(x, y)\tau_2)]$. Denoting $\hat{W}(\omega_1, \omega_2)$ as the 2D Fourier transform of $w(\tau_1, \tau_2)$ and using the frequency shifting property of the Fourier transform, we have

$$\gamma(x, y, \omega_1, \omega_2) = \hat{W}(2\omega_1 - 2\phi_x(x, y), 2\omega_2 - 2\phi_y(x, y)) \tag{4.9}$$

As window w has a low-pass behavior, $\gamma(x, y, \omega_1, \omega_2)$ is maximum for $\hat{W}(0, 0)$ i.e. when $[\omega_1, \omega_2] = [\phi_x(x, y), \phi_y(x, y)]$. In other words,

$$[\phi_x(x, y), \phi_y(x, y)] = \arg\max_{\omega_1, \omega_2} \gamma(x, y, \omega_1, \omega_2) \tag{4.10}$$

Hence, the phase derivatives at pixel location (x, y) can be estimated by finding the values of (ω_1, ω_2) at which $\gamma(x, y, \omega_1, \omega_2)$ attains its maximum. Note that the phase derivatives with respect to both spatial coordinates i.e. x and y can be simultaneously determined using Eq.(4.10). By repeating the above analysis for all pixels, the phase derivatives for the entire fringe pattern can be estimated. The computational burden for evaluating the 2D Fourier transform can be greatly relieved by using 2D fast Fourier transform (FFT) algorithm.

4.3 Simulation and Experimental Analysis

For analysis, a complex reconstructed interference field signal $\Gamma(x, y)$ (128×128 pixels) was simulated at an SNR of 10 dB using 'awgn' function of MATLAB. The real part of $\Gamma(x, y)$ i.e. the corresponding fringe pattern is shown in Fig.4.1(a). For the 2D-PSWVD method, a 17×17 Gaussian window was used.

Applying the proposed method, the estimated phase derivative with respect to x and the corresponding estimation error in radians/pixel are shown in Fig.4.1(b) and Fig.4.1(c). Similarly, the estimated phase derivative estimate with respect to y and the corresponding estimation error in radians/pixel are shown in Fig.4.1(d) and Fig.4.1(e). The RMSEs for phase derivative estimation with respect to x and y were 0.0048 and 0.0036 radians/pixel respectively. The pixels near the borders of the fringe pattern were neglected in the analysis to ignore the errors at the boundaries.
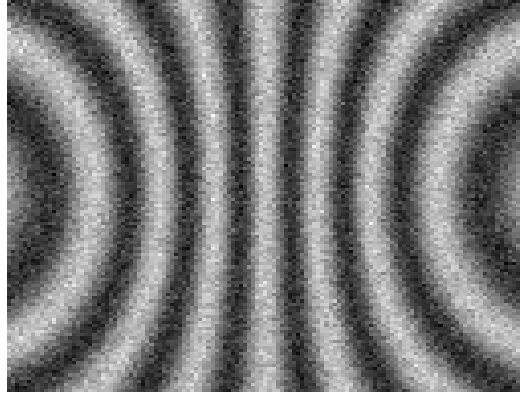
(a)
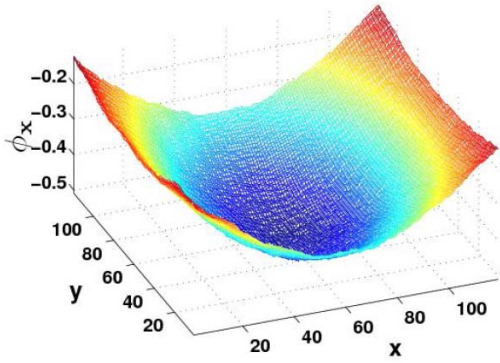
(b)
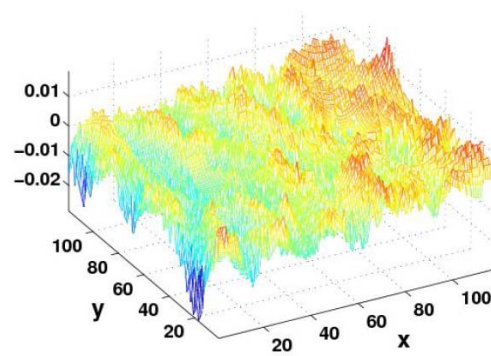
(c)
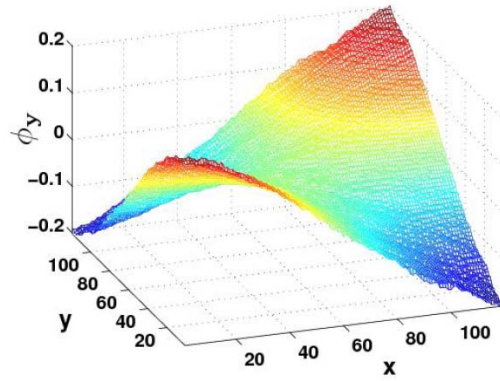
(d)
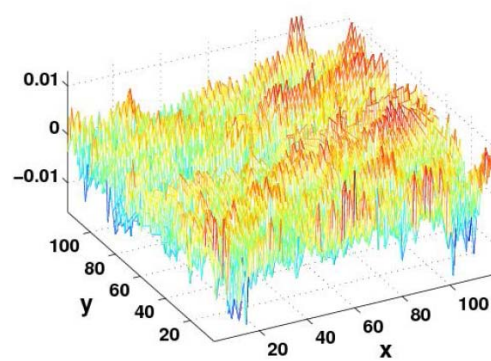
(e)

Fig. 4.1. (a) Simulated fringe pattern. (b) Estimated phase derivative with respect to x in radians/pixel. (c) Error between original and estimated phase derivatives with respect to x in radians/pixel. (d) Estimated phase derivative with respect to y in radians/pixel. (e) Error between original and estimated phase derivatives with respect to y in radians/pixel.

SNR	RMSE for the 2D-PSWVD method	RMSE for 1D-PSWVD method
2	0.0090	0.2912
5	0.0067	0.0499
10	0.0048	0.0122
15	0.0040	0.0072
20	0.0037	0.0047

Table 4.1. Comparison of RMSEs (in radians/pixel) for estimating phase derivative with respect to x at various SNRs (in dB).

The major advantage of the proposed method is the improved robustness against noise as compared to the one-dimensional PSWVD. The reason is that, a two-dimensional window captures data samples along both x and y for the evaluation of the PSWVD in the proposed method and consequently provides smoothing in both directions, effectively increasing the method's immunity against noise. On the contrary, the 1D-PSWVD method uses a window along only one direction. Hence, although the method is quite computationally efficient due to the use of one-dimensional Fourier transform, its performance is deteriorated in the presence of high noise.

To compare the robustness of both methods against noise, a reconstructed interference field signal similar to the one used for Fig.4.1 was simulated at different SNRs. The RMSEs (in radians/pixel) for phase derivative estimation obtained by the proposed method and the 1D-PSWVD method at various SNRs (in dB) are shown in Table 4.1. From the table, it is clear that the proposed method exhibits superior performance and provides phase derivative estimates with reasonable accuracy even for very low SNR such as 2 dB. In addition, the computational efficiency of the proposed method can be significantly improved using techniques like fixed-point computations [108] and graphics processing units [109].

To test the practical applicability of the proposed method, a DHI experiment was conducted by subjecting a circularly clamped object to central load and recording two holograms before and after deformation using a Coherent Verdi laser (532 nm). The complex amplitudes of the object wave before and after deformation were obtained by numerical reconstruction performed using discrete Fresnel transform [83]. The reconstructed interference field was obtained by multiplying the post-deformation complex amplitude with the conjugate of the pre-deformation complex amplitude. The corresponding experimental fringe pattern is shown in Fig.4.2(a). The estimated phase derivative with respect to x in radians/pixel is shown in Fig.4.2(b). Similarly, Fig.4.2(c) shows the estimated phase derivative with respect to y in radians/pixel.
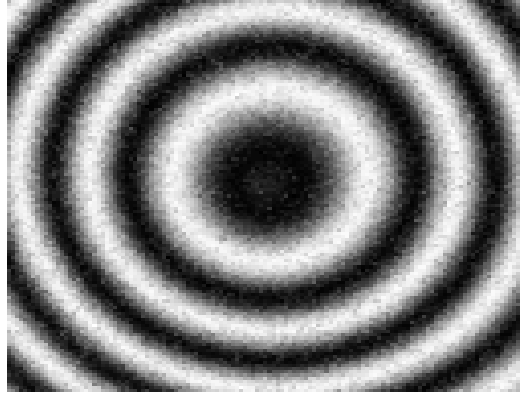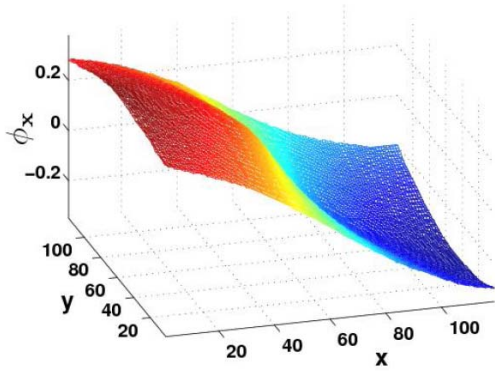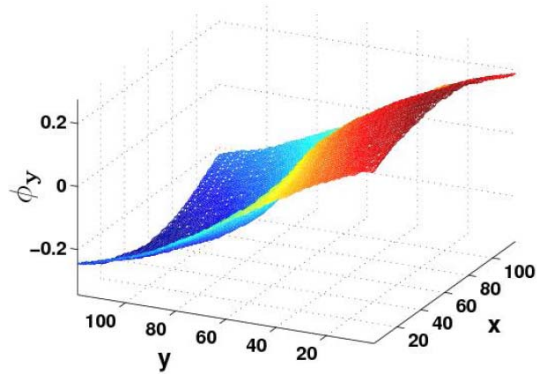
Fig. 4.2. (a) Experimental fringe pattern. (b) Estimated phase derivative with respect to x in radians/pixel. (c) Estimated phase derivative with respect to y in radians/pixel.

4.4 Summary

This chapter proposed a 2D-PSWVD method for the direct estimation of phase derivative in digital holographic interferometry without requiring any unwrapping or filtering operations. The major strength of the method is its high robustness against noise. In addition, the method enables simultaneous retrieval of phase derivatives with respect to both spatial directions. The applicability of the proposed method is validated using simulation and experimental results.

Chapter 5

Complex-lag distribution method

5.1   Introduction

In the previous chapters, methods were developed to estimate first order phase derivatives from fringe patterns. However, for many practical applications, the higher order derivatives are also required. For instance, in deformation analysis, the second order phase derivative corresponds to the curvature distribution of a deformed object. This chapter introduces a generalized approach based on complex-lag distributions for the estimation of arbitrary order phase derivatives.

5.2   Theory

The complex reconstructed interference field in DHI can be expressed using Eq.(2.1) as

$$\Gamma(x, y) = a(x, y) \exp[j\phi(x, y)] + \eta(x, y) \tag{5.1}$$

For a given row y, the above equation could be written as

$$\Gamma(x) = a(x) \exp[j\phi(x)] + \eta(x) \tag{5.2}$$

The mth order phase derivative $\phi^{(m)}(x)$ with respect to x is given as

$$\phi^{(m)}(x) = \frac{\partial^m \phi(x)}{\partial x^m} \tag{5.3}$$

For the estimation of $\phi^{(m)}(x)$, a generalized complex-lag moment (GCM) [110] based approach is proposed. From $\Gamma(x)$, the GCM is computed as,

$$\mathrm{GCM}_N^m[\Gamma](x, \tau) = h(\tau) \prod_{k=0}^{N-1} \Gamma^{\omega_{N,k}^{N-m}} \left(x + \omega_{N,k} \sqrt[m]{\frac{m!}{N}\tau} \right) \tag{5.4}$$

where $\omega_{N,k} = \exp[j2\pi k/N]$, N is a parameter such that $N \geq m$ and h is a real symmetric window having a low-pass behavior. For the simplicity of analysis, the amplitude term within the window region is assumed constant and neglected along with the noise term. So we have,

$$\text{GCM}_N^m[\Gamma](x,\tau) = h(\tau) \exp\left[j \sum_{k=0}^{N-1} \phi\left(x + \omega_{N,k} \sqrt[m]{\frac{m!}{N}}\tau \right) \omega_{N,k}^{N-m} \right] \tag{5.5}$$

Using Taylor series expansion, we have

$$\phi\left(x + \omega_{N,k} \sqrt[m]{\frac{m!}{N}}\tau \right) = \sum_{p=0}^{\infty} \phi^{(p)}(x) \frac{\omega_{N,k}^p}{p!} \left(\sqrt[m]{\frac{m!}{N}}\tau \right)^p \tag{5.6}$$

and Eq.(5.5) becomes

$$\text{GCM}_N^m[\Gamma](x,\tau) = h(\tau) \exp\left[j \sum_{k=0}^{N-1} \sum_{p=0}^{\infty} \phi^{(p)}(x) \frac{\omega_{N,k}^{p+N-m}}{p!} \left(\sqrt[m]{\frac{m!}{N}}\tau \right)^p \right] \tag{5.7}$$

Noting $\omega_{N,k}^{p+N-m} = \exp[j2\pi k(p+N-m)/N]$, we have

$$\sum_{k=0}^{N-1} \omega_{N,k}^{p+N-m} = \begin{cases} N, & \text{if } p = 0 \text{ and } N = m \\ N, & \text{if } p = Nr + m \\ 0, & \text{otherwise} \end{cases}$$

where r is an integer such that $r = 0, 1, 2, \ldots$ etc. Consequently, the argument of GCM in Eq.(5.7) vanishes unless $p = Nr + m$ or $p = 0$ and $N = m$.

Considering the case when $N \neq m$, we have,

$$\text{GCM}_N^m[\Gamma](x,\tau) = h(\tau) \exp\left[jN \sum_{r=0}^{\infty} \frac{\phi^{(Nr+m)}(x)}{(Nr+m)!} \left(\sqrt[m]{\frac{m!}{N}}\tau \right)^{Nr+m} \right]$$
$$= h(\tau) \exp\left[j\phi^{(m)}(x)\tau \right] \exp[jU(x,\tau)] \tag{5.8}$$

where $\phi^{(m)}(x)$ is the desired phase derivative and

$$U(x,\tau) = N \sum_{r=1}^{\infty} \frac{\phi^{(Nr+m)}(x)}{(Nr+m)!} \left(\sqrt[m]{\frac{m!}{N}}\tau \right)^{Nr+m} \tag{5.9}$$

Within the given window region, the phase usually varies slowly and its $(Nr+m)^{th}$ order derivatives i.e. $\phi^{(Nr+m)}(x)$ are negligible for $r \geq 1$. Hence, $U(x,\tau) \approx 0$ and Eq.(5.8) can be written as

$$\text{GCM}_N^m[\Gamma](x,\tau) = h(\tau) \exp\left[j\phi^{(m)}(x)\tau \right] \tag{5.10}$$

The Fourier transform (FT) of the GCM provides the generalized complex-lag distribution (GCD),

$$\text{GCD}_N^m[\Gamma](x, \Omega) = \int_{-\infty}^{\infty} h(\tau) \exp\left[j\phi^{(m)}(x)\tau\right] \exp[-j\Omega\tau]\, d\tau \tag{5.11}$$

which is essentially the FT of $h(\tau)$ modulated by the term $\exp[j\phi^{(m)}(x)\tau]$. If the FT of the window $h(\tau)$ is denoted as $\hat{H}(\Omega)$, the frequency shifting property of the Fourier transform yields

$$\text{GCD}_N^m[\Gamma](x, \Omega) = \hat{H}(\Omega - \phi^{(m)}(x)) \tag{5.12}$$

Since the window function is chosen to have a low-pass behavior, GCD is maximum for $\hat{H}(0)$ i.e. when $\Omega = \phi^{(m)}(x)$. Hence the mth order phase derivative $\phi^{(m)}(x)$ can be obtained by finding the frequency Ω at which the GCD spectrum attains its maximum. So we have,

$$\phi^{(m)}(x) = \arg\max_{\Omega} |\text{GCD}_N^m[\Gamma](x, \Omega)| \tag{5.13}$$

These equations were obtained for the case $N \neq m$. When $N = m$, an extra phase term corresponding to $p = 0$ in Eq.(5.7) would arise and consequently, Eq.(5.8), Eq.(5.10) and Eq.(5.12) are modified as,

$$\text{GCM}_N^m[\Gamma](x, \tau) = h(\tau) \exp\left[j\phi^{(m)}(x)\tau\right] \exp[jN\phi(x)] \exp[jU(x, \tau)] \tag{5.14}$$

$$\text{GCM}_N^m[\Gamma](x, \tau) = h(\tau) \exp\left[j\phi^{(m)}(x)\tau\right] \exp[jN\phi(x)] \tag{5.15}$$

$$\text{GCD}_N^m[\Gamma](x, \Omega) = \exp[jN\phi(x)]\hat{H}(\Omega - \phi^{(m)}(x)) \tag{5.16}$$

The above equations show that the additional scaling term $\exp[jN\phi(x)]$ appears when $N = m$. However, it has no effect on the peak-detection strategy of the GCD since the scaling term is independent of τ and $|\exp[jN\phi(x)]| = 1$. Hence Eq.(5.13) remains valid.

So, the proposed method can be summarized in the following steps

1. The complex reconstructed interference field of an arbitrary row or column is considered as in Eq.(5.2).

2. The GCM for the desired phase derivative order m is computed using Eq.(5.4).

3. The GCD is obtained through the Fourier transform of the GCM as in Eq.(5.11).

4. The mth order phase derivative is calculated by tracing the peak of the GCD using Eq.(5.13).

5. The above steps are repeated for all rows or columns to obtain the overall phase derivative.

(a)

(b)

(c)

(d)

(e)

(f)
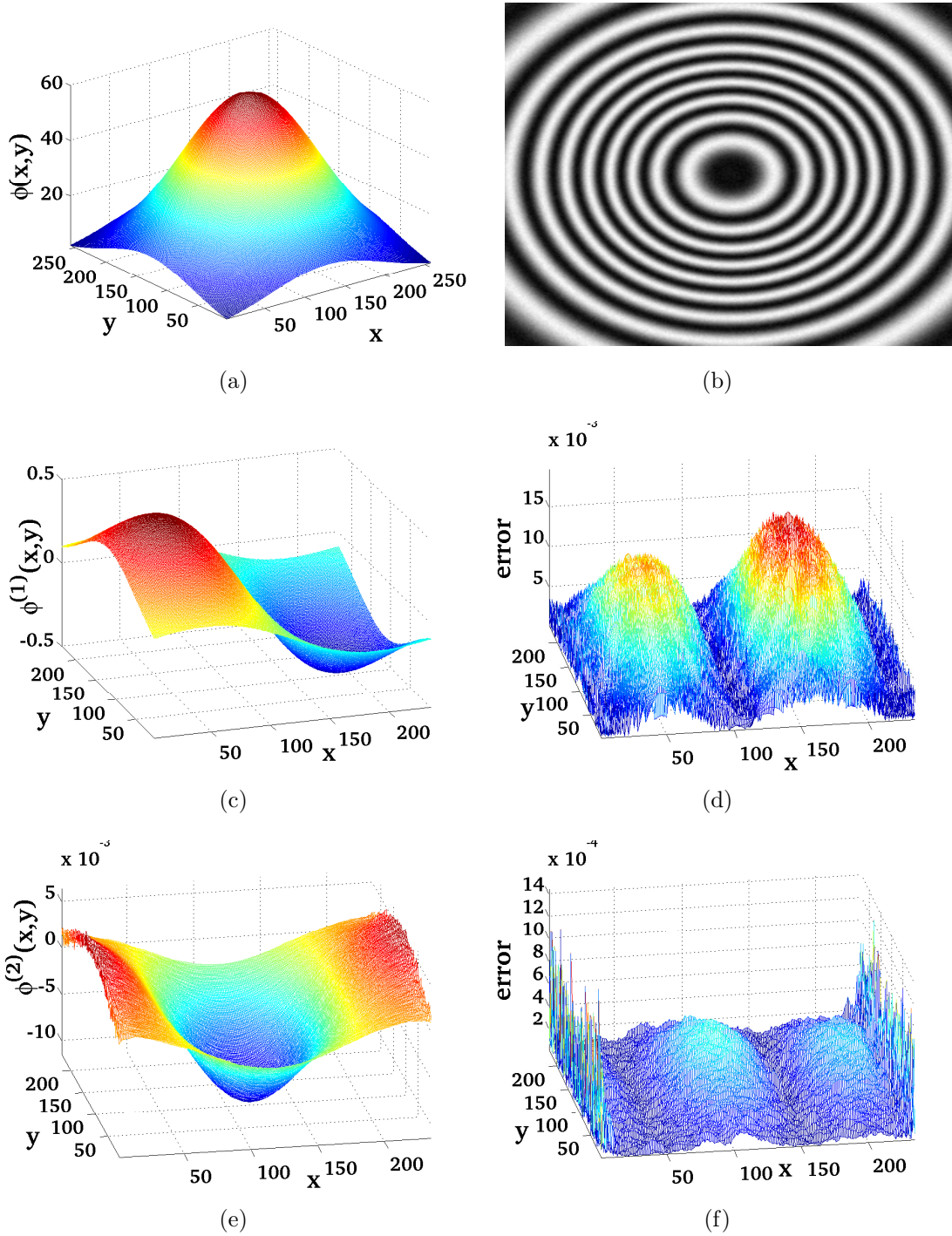
Fig. 5.1. (a) Original phase $\phi(x,y)$ in radians. (b) Fringe pattern. (c) Estimated first order phase derivative $\phi^{(1)}(x,y)$ in radians/pixel. (d) First order phase derivative estimation error. (e) Estimated second order phase derivative $\phi^{(2)}(x,y)$ in radians/pixel^2. (f) Second order phase derivative estimation error.

5.3 Simulation and Experimental Analysis

The proposed method was analyzed for the estimation of the first and second order phase derivatives. A complex reconstructed interference field signal (size 256×256 pixels) of the following form was simulated in MATLAB,

$$\Gamma(x, y) = \exp[j\phi(x, y)] \tag{5.17}$$

and noise was added at a signal to noise ratio (SNR) of 25 dB using MATLAB's 'awgn' function. The original phase $\phi(x, y)$ in radians is shown in Fig.5.1(a). The corresponding fringe pattern constituted by the real part of the complex reconstructed interference field is shown in Fig.5.1(b). For the estimation of first order phase derivative $\phi^{(1)}(x, y)$, we used $m = 1$ and $N = 2$ to compute the GCM in Eq.(5.4). So, the corresponding GCM is given as

$$\text{GCM}_2^1[\Gamma](x, \tau) = h(\tau)\Gamma(x + \tau/2)\Gamma^{-1}(x - \tau/2) \tag{5.18}$$

This expression leads to a pseudo Wigner-Ville-like distribution of the second chapter. Hence, pseudo Wigner-Ville distribution could be considered a special case of the generalized complex-lag distribution. Similarly, for the estimation of the second order phase derivative $\phi^{(2)}(x, y)$, we used $m = 2$ and $N = 2$ and the corresponding GCM is given as

$$\text{GCM}_2^2[\Gamma](x, \tau) = h(\tau)\Gamma(x + \sqrt{\tau})\Gamma(x - \sqrt{\tau}) \tag{5.19}$$

For the analysis, a Gaussian window of length 65 samples was generated using MATLAB's 'gausswin' function. The estimated first order phase derivative and the corresponding absolute estimation errors in radians/pixel are shown in Fig.5.1(c) and Fig.5.1(d). Similarly, the estimated second order phase derivative and the corresponding absolute estimation errors in radians/pixel^2 are shown in Fig.5.1(e) and Fig.5.1(f). The root mean square errors for the estimation of the first and second order phase derivatives using the proposed method were 0.008 radians/pixel and 2.443×10^{-4} radians/pixel^2. The pixels near the borders were neglected for the analysis.

To test the practical applicability in DHI, the proposed method was applied on an experimental fringe pattern as shown in Fig.5.2(a). The estimated first order phase derivative in radians/pixel after median filtering is shown in Fig.5.2(b). Finally, the estimated second order phase derivative in radians/pixel^2 after median filtering is shown in Fig.5.2(c).

5.4 Summary

This chapter presented a complex-lag distribution based method for the estimation of phase derivatives of arbitrary order in DHI. The method provides a generalized approach to design distributions based on the desired phase derivative order. This enables direct retrieval of the required phase derivative. In addition, the proposed method does not require
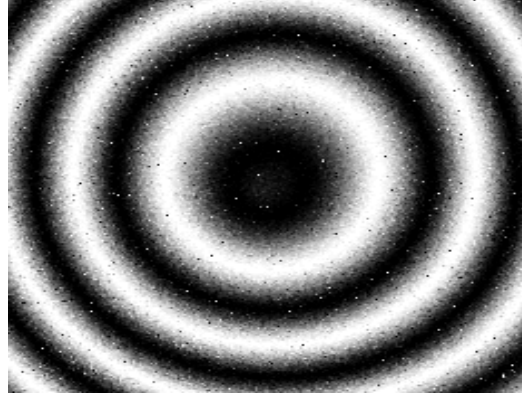
(a)
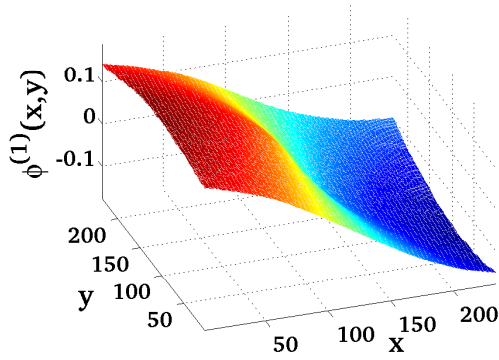
(b)
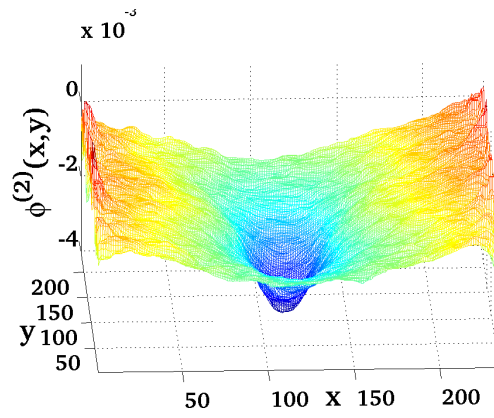
(c)

Fig. 5.2. (a) Experimental fringe pattern. (b) Estimated first order phase derivative in radians/pixel. (c) Estimated second order phase derivative in radians/pixel^2.

phase unwrapping or numerical differentiation operations. Simulation and experimental results validate the strength of the proposed method.

Chapter 6

Applications

6.1 Introduction

In the previous chapters, the pseudo Wigner-Ville distribution method was introduced for phase derivative estimation from fringe patterns. This chapter presents some of the applications of the PSWVD method in digital holographic interferometry and fringe projection.

6.2 Defect detection

For many applications such as quality control and industrial inspection, the automated detection of defects or faults like cracks, debonds etc. from fringe patterns is desired. A defect or fault is characterized by rapid fringe density variations in the fringe pattern. The classification of different types of faults occurring in fringe patterns is detailed in [111]. Various methods based on fringe density estimation [112, 113], pattern classification [114–117], discontinuity tracking [118], wavelet transform [119], windowed Fourier transform [49] etc. have been proposed for the detection of defects from fringe patterns.

6.2.1 Theory

The complex reconstructed interference field in DHI can be expressed using Eq.(2.1) as

$$\Gamma(x, y) = a(x, y) \exp[j\phi(x, y)] + \eta(x, y) \tag{6.1}$$

The real part of the reconstructed interference field constitutes a fringe pattern.

In the proposed method, two fringe patterns i.e. one defect-free (reference) and the other with defects are considered. Such fringe patterns commonly arise in non-destructive testing applications like condition monitoring where fringe evolution over time is monitored for defects and consequently, a sequence of fringe patterns is captured [111]. Between the two fringe patterns, the change of phase is abrupt near the defect. Effectively, in the vicinity of the defect, the difference in the phase derivatives corresponding to the two fringe patterns is pronounced compared to other regions. Hence, by using the information about the phase derivatives, the defect could be identified.

To obtain the phase derivatives from $\Gamma(x, y)$, two dimensional pseudo Wigner-Ville distribution (2D-PSWVD) was applied. The 2D-PSWVD is given as,

$$G(x, y, \omega_1, \omega_2) = \int_{-\infty}^{\infty} \int_{-\infty}^{\infty} w(\tau_1, \tau_2) \Gamma(x + \tau_1, y + \tau_2) \Gamma^*(x - \tau_1, y - \tau_2)$$
$$\exp[-2j(\omega_1 \tau_1 + \omega_2 \tau_2)] \, \mathrm{d}\tau_1 \mathrm{d}\tau_2 \qquad (6.2)$$

where w is a real symmetric window and '*' denotes the complex conjugate. The phase derivatives with respect to x and y i.e. $[\phi_x = \partial \phi / \partial x, \phi_y = \partial \phi / \partial y]$ correspond to the spatial frequencies $[\omega_1, \omega_2]$ at which the 2D-PSWVD attains its peak. So we have,

$$[\phi_x, \phi_y] = \arg \max_{\omega_1, \omega_2} G(x, y, \omega_1, \omega_2) \qquad (6.3)$$

Denoting the phases corresponding to the reference and defect-containing fringe patterns as ϕ_1 and ϕ_2, the respective phase derivatives $[\phi_{1x}, \phi_{1y}]$ and $[\phi_{2x}, \phi_{2y}]$ are computed using the 2D-PSWVD as shown above.

To design a suitable detection criterion for locating defects, the relative change or difference in the phase derivatives corresponding to the two fringe patterns is considered. Treating the phase derivatives with respect to x and y as vectors in a Euclidean space i.e. $\vec{\phi}_{1d} = [\phi_{1x}, \phi_{1y}]$ and $\vec{\phi}_{2d} = [\phi_{2x}, \phi_{2y}]$, the phase derivative change can be analogously interpreted as the distance between the two vectors which is computed by the vector norm. Accordingly, the *relative* phase derivative difference can be computed as

$$\rho(x, y) = \frac{||\vec{\phi}_{2d} - \vec{\phi}_{1d}||_2}{||\vec{\phi}_{1d}||_2}$$
$$= \frac{\sqrt{(\phi_{2x}(x, y) - \phi_{1x}(x, y))^2 + (\phi_{2y}(x, y) - \phi_{1y}(x, y))^2}}{\sqrt{\phi_{1x}^2(x, y) + \phi_{1y}^2(x, y)}} \qquad (6.4)$$

where '$|| \ ||_2$' denotes the vector norm. Finally, by selecting a threshold value say *thr*, the defect region can be identified by the following algorithm

if $\rho(x,y) \geq thr$

$\quad\quad x,y \in$ defect region

else

$\quad\quad x,y \in$ defect-free region

Accordingly, the steps involved in the detection of defects using the proposed method can be summarized as,

1. The 2D-PSWVD is computed for the reference and defect-containing fringe patterns using Eq.(6.2)

2. The phase derivatives are obtained for the two fringe patterns using Eq.(6.3).

3. The relative phase derivative difference ρ for the two fringe patterns is measured using Eq.(6.4).

4. For each pixel with spatial coordinates (x,y) in the fringe pattern, $\rho(x,y)$ is compared with certain threshold value; if the relative phase derivative difference exceeds the threshold, the pixel corresponds to a defect.

For the analysis, the threshold value was selected as 30%. However, it needs to be emphasized that the choice of the threshold depends on various factors such as fringe quality, noise etc. and could be varied based on the application.

6.2.2 Simulation Analysis

For the analysis, reconstructed interference field ($N \times N$ pixels) corresponding to the reference fringe pattern was simulated as

$$\Gamma(x,y) = \exp[j\omega_0 x] + \eta(x,y) \quad \forall\, x,y \in [1, N = 256] \tag{6.5}$$

where $\omega_0 = 30/N$ and $\eta(x,y)$ is the additive white Gaussian noise added using MATLAB's 'awgn' function at SNR of 20 dB. The real part of $\Gamma(x,y)$ i.e. the reference fringe pattern is shown in Fig.6.1(a). Similarly, the simulated fringe pattern containing defects of various sizes ($L \times L$ pixels with L= 19, 23 and 33) is shown in Fig.6.1(b).

The proposed method was applied to locate the defects. For the 2D-PSWVD calculations, a 11×11 Gaussian window was used. For the analysis, the pixels near the borders of the fringe patterns were neglected to ignore the phase derivative estimation errors at the edges. The computed relative phase difference i.e. $\rho(x,y)$ is shown in Fig.6.1(c). From the figure, it is clear that near the defects, the relative phase derivative difference shows a pronounced increase compared to other neighboring regions. Using the detection algorithm of the proposed method, the defect regions were identified as shown in Fig.6.1(d). To improve

(a)

(b)

(c)

(d)

(e)
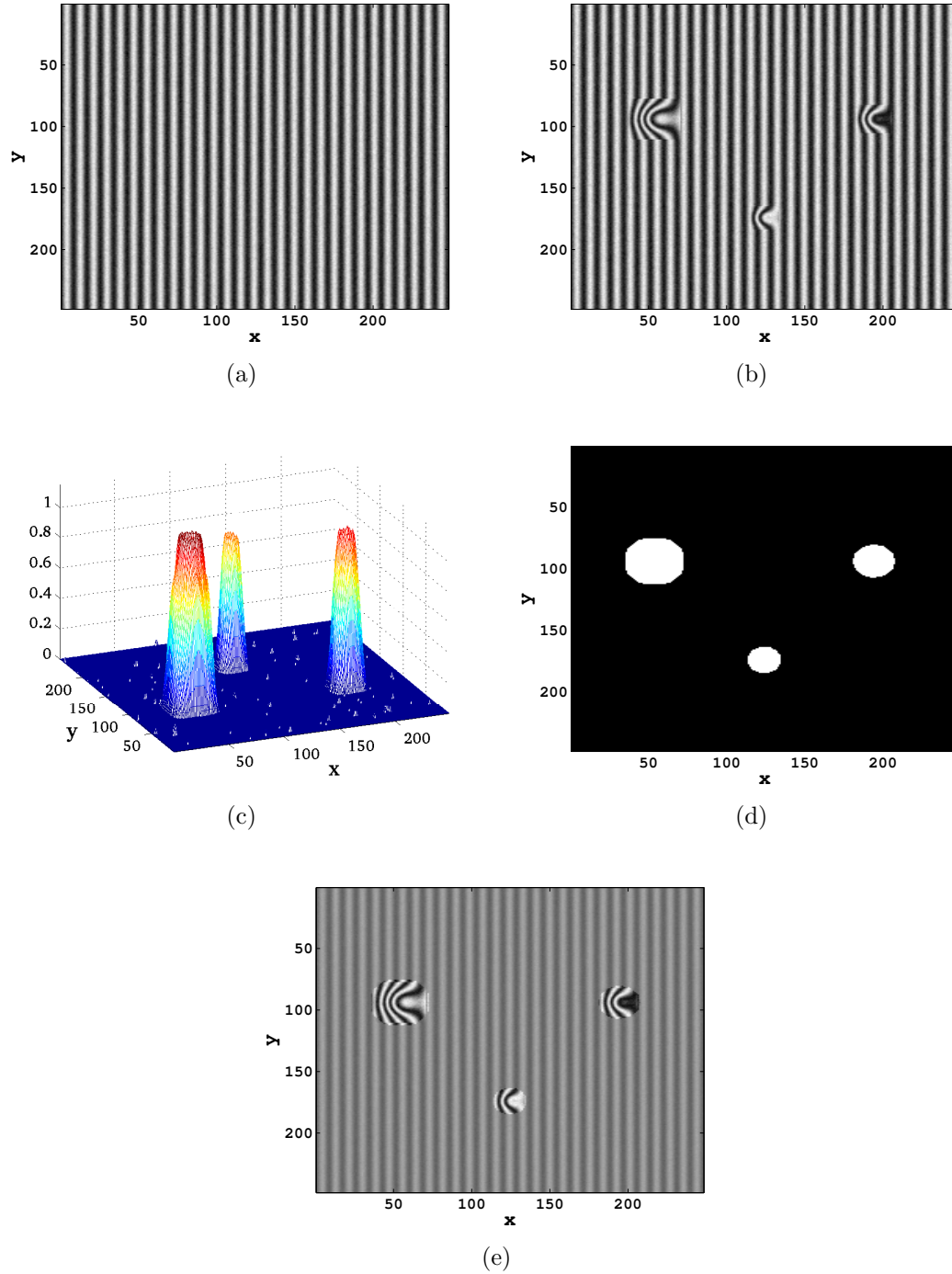
Fig. 6.1. (a) Reference fringe pattern. (b) Fringe pattern with defects. (c) Relative phase derivative difference. (d) Identified defect regions. (e) Highlighted defect regions.

44
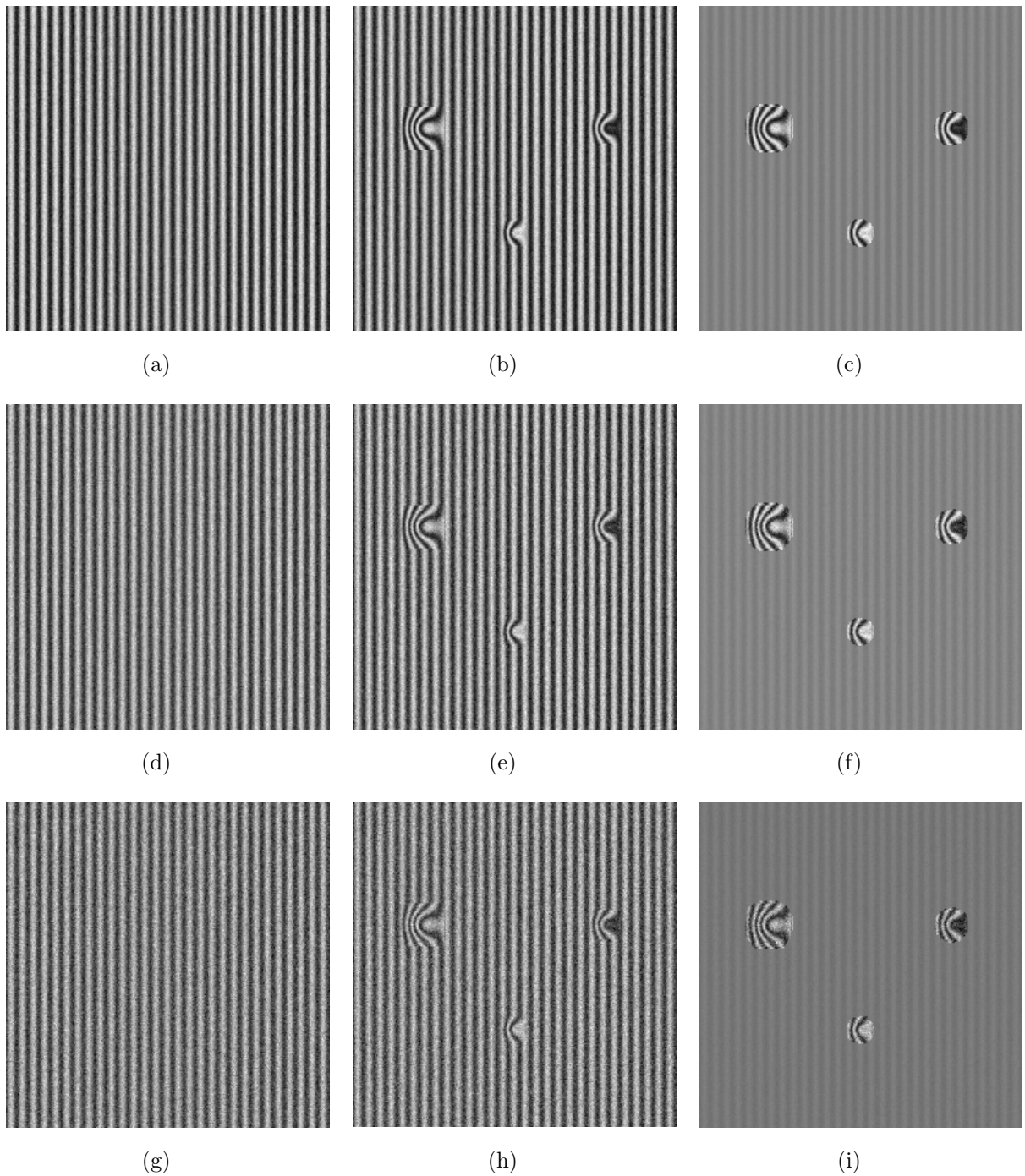
Fig. 6.2. Reference fringe pattern, defect-containing fringe pattern and the highlighted defects at SNR of 16 dB for (a), (b) and (c); 12 dB for (d), (e) and (f); 8 dB for (g), (h) and (i).

detection accuracy, the pixels surrounded by a defect region's pixels were also considered part of the defect region. Finally, the highlighted defect regions in the fringe pattern are shown in Fig.6.1(e). The results show that the proposed method is capable of identifying multiple defects of varying sizes from the fringe patterns.

To test the robustness of the proposed method against noise for defect detection, different fringe patterns with and without defects were simulated at varying levels of SNR. For an SNR of 16 dB, the reference fringe pattern, defect-containing fringe pattern and the highlighted defect regions using the proposed method are shown in Fig.6.2(a-c). Similarly, the corresponding figures for SNRs of 12 dB and 8 dB are shown in Fig.6.2(d-f) and Fig.6.2(g-i). These figures demonstrate that the proposed method provides reliable identification of defects even in the presence of high noise.

The results clearly demonstrate the potential of the proposed method for identifying defects in fringe patterns. The main advantages of the proposed method are the ability to identify defects of varying sizes and robustness against noise. The results demonstrate the potential of the proposed method for non-destructive testing and evaluation applications.

6.3 Temporal measurement of surface slopes using fringe projection

For several applications which involve transient phenomena such as crack propagation and impulse loading, the evolution of the displacement derivative with time is usually required [120–125]. In this section, the pseudo Wigner-Ville distribution method is applied in fringe projection technique [3] for dynamic measurement of the displacement derivative.

The fringe projection technique involves projecting a structured pattern (usually a sinusoidal fringe pattern) on an object and recording the image of the fringe pattern, phase modulated by the surface profile of the object. The main advantages of the fringe projection technique are equipment affordability, relative ease of implementation, ability to work with objects of different sizes, and whole-field measurement capability. In addition, fringe projection techniques usually do not require sophisticated instruments like lasers and are hence suitable for factory floor conditions. These techniques have been used for many scientific and industrial applications like MEMS component characterization [126], surface roughness measurement [127], corrosion analysis [128], reverse engineering [129] etc.

6.3.1 Theory

If a carrier fringe pattern is projected on the undeformed object, the reflected intensity recorded by the CCD camera has the following form:

$$I_1(x, y) = a_1(x, y) + b_1(x, y) \cos[\omega_0 x + \phi_R(x, y)] + \eta_1(x, y) \qquad (6.6)$$

where $\phi_R(x, y)$ is the reference phase which corresponds to the surface profile of the undeformed object, ω_0 is the carrier frequency, $a_1(x, y)$ is the background intensity or the d.c. term, $b_1(x, y)$ is the fringe amplitude and $\eta_1(x, y)$ is the noise term assumed to be additive white Gaussian noise. Here, x and y refer to the pixels along horizontal and vertical directions for the $N \times N$ image. This fringe pattern corresponding to the undeformed object would be referred to as the reference fringe pattern in the rest of the paper. Eq.(6.6) can be equivalently written as

$$I_1(x, y) = a_1(x, y) + \frac{1}{2} b_1(x, y) \exp[-j(\omega_0 x + \phi_R(x, y))]$$
$$+ \frac{1}{2} b_1(x, y) \exp[j(\omega_0 x + \phi_R(x, y))] + \eta_1(x, y) \qquad (6.7)$$

From Eq.(6.7), it is clear that the spectrum of $I_1(x, y)$ has contribution from $a_1(x, y)$ around the d.c. or low frequencies and around $-\omega_0$ and ω_0 due to the contribution from the second and third terms.

For a dynamically deformed object, a carrier fringe pattern is projected on the object's surface and the reflected light intensity is recorded as a sequence of say M frames or images. The frames are numbered from 1 to M in steps of unity where each frame number corresponds to the particular time instant at which the frame was captured. For k^{th} frame where $k \in [1, M]$, the recorded intensity can be given as

$$I_2(x, y, k) = a_2(x, y, k) + b_2(x, y, k) \cos[\omega_0 x + \phi_D(x, y, k)] + \eta_2(x, y, k) \tag{6.8}$$

where $\phi_D(x, y, k)$ contains information about the surface profile of the object for k^{th} frame. The above equation can be equivalently written as

$$I_2(x, y, k) = a_2(x, y, k) + \frac{1}{2} b_2(x, y, k) \exp[-j(\omega_0 x + \phi_D(x, y, k))]$$
$$+ \frac{1}{2} b_2(x, y, k) \exp[j(\omega_0 x + \phi_D(x, y, k))] + \eta_2(x, y, k) \tag{6.9}$$

Filtering the spectra of $I_1(x, y)$ and $I_2(x, y, k)$ around ω_0 thereby removing the contribution of d.c. terms and the negative part of the spectra , we obtain

$$\Gamma_1(x, y) = b_1(x, y) \exp[j(\omega_0 x + \phi_R(x, y))] + \eta_1'(x, y) \tag{6.10}$$

$$\Gamma_2(x, y, k) = b_2(x, y, k) \exp[j(\omega_0 x + \phi_D(x, y, k))] + \eta_2'(x, y, k) \tag{6.11}$$

Multiplying the complex conjugate of $\Gamma_1(x, y)$ with $\Gamma_2(x, y, k)$, we have

$$\Gamma(x, y, k) = \Gamma_2(x, y, k)\Gamma_1^*(x, y) \tag{6.12}$$

which can be approximated as

$$\Gamma(x, y, k) = b(x, y, k) \exp[j\phi(x, y, k)] + \eta(x, y, k) \tag{6.13}$$

Here '*' denotes the complex conjugate, $\eta(x, y, k)$ is the noise term and

$$b(x, y, k) = b_1(x, y)b_2(x, y, k) \tag{6.14}$$

$$\phi(x, y, k) = \phi_D(x, y, k) - \phi_R(x, y) \tag{6.15}$$

Since $\phi(x, y, k)$ corresponds to the difference between the surface profiles of the object before and after deformation, it actually relates to the out-of-plane displacement experienced by the object under deformation for k^{th} frame. Accordingly, the spatial phase derivative given by

$$\omega_x(x, y, k) = \frac{\partial \phi(x, y, k)}{\partial x} \tag{6.16}$$

corresponds to the displacement derivative for the particular frame. For an arbitrary row y in the kth frame, Eq.(6.13) can be written as

$$\Gamma(x, k) = b(x, k) \exp[j\phi(x, k)] + \eta(x, k) \tag{6.17}$$

(a)   (b)
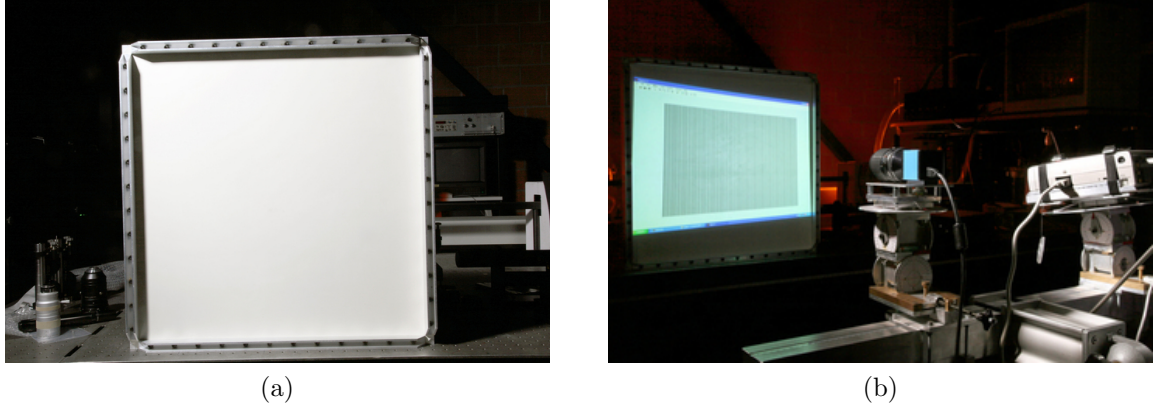
Fig. 6.3. (a) Membrane (b) Experimental setup

For the estimation of the phase derivative, the PSWVD is applied using Eq.(2.6) as,

$$W(x, \Omega, k) = \sum_{\tau=-\infty}^{\infty} w(\tau)\Gamma(x+\tau, k)\Gamma^*(x-\tau, k)\exp(-j2\Omega\tau) \qquad (6.18)$$

where w is a Gaussian window. The phase derivative $\omega_x(x, k)$ is given as,

$$\omega_x(x, k) = \arg\max_{\Omega} W(x, \Omega, k) \qquad (6.19)$$

The above equation gives the phase derivative estimate along x for a given row y. The above procedure can be applied for all rows $y \in [1, N]$ to estimate the overall phase derivative $\omega_x(x, y, k)$ with respect to x for the kth frame. Proceeding in a similar manner, the phase derivative estimates can be obtained for all $k \in [1, M]$ and thus the temporal evolution of the phase derivative can be determined.

It needs to be emphasized that a continuous distribution of the phase derivative is directly obtained without relying on any unwrapping operation since no 'arctan' operator is involved in the above procedure. Since the phase derivative has to be estimated for each frame, the low computational footprint of the PSWVD method accompanied by the non-requirement of unwrapping operation plays an important role in the overall computational cost of the temporal evolution analysis.

6.3.2   Experimental Results

To test the practical applicability of the proposed method, a fringe projection experiment was conducted to analyze a dynamically deformed object. A white leather membrane (60 × 60 cm) clamped on four sides was taken as the object as shown in Fig.6.3(a). The fringe projection experimental setup is shown in Fig.6.3(b). An EPSON EMP-710 projector was used to project fringes on the membrane and an IMAGINGSOURCE DFK
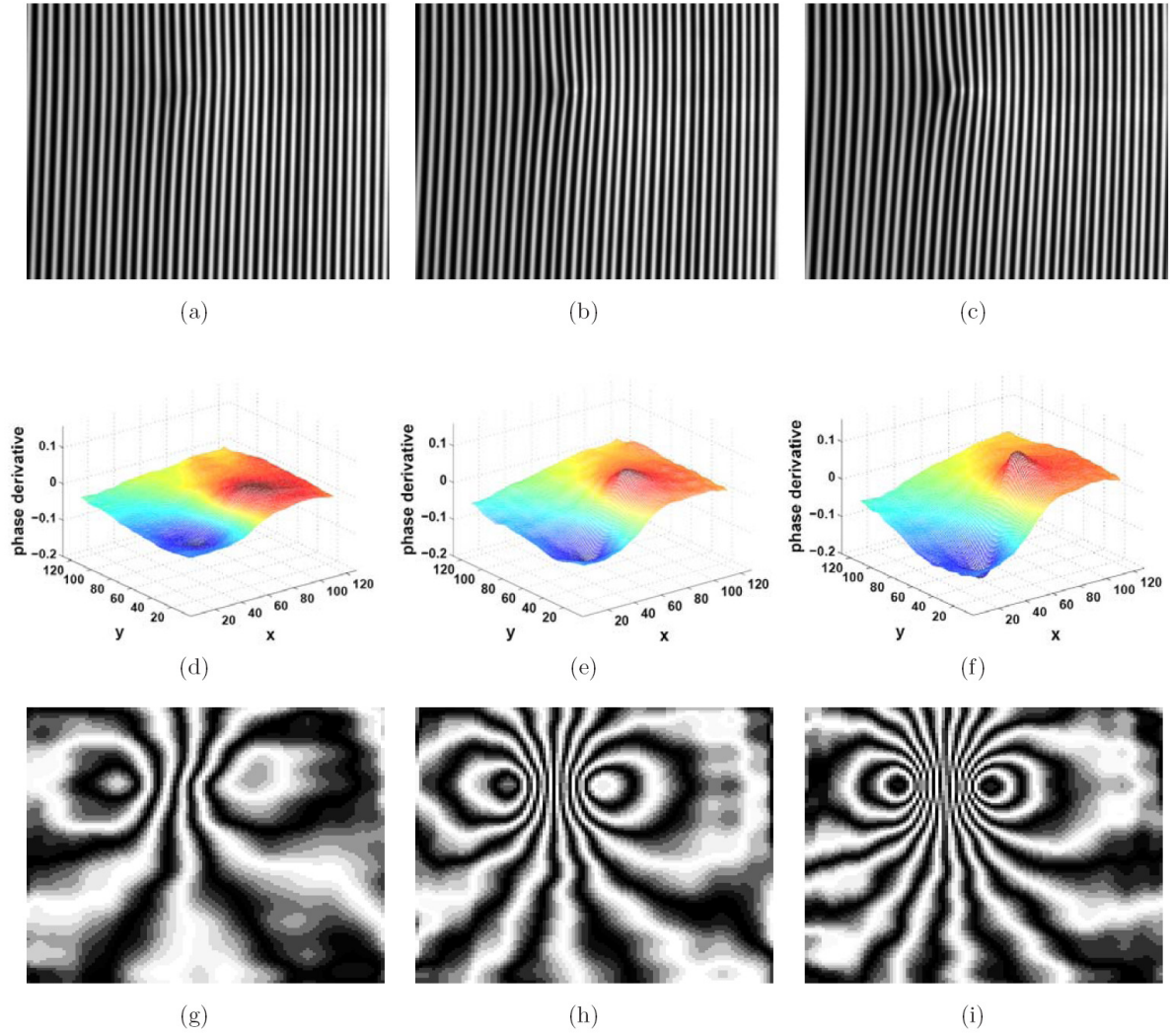
Fig. 6.4. Experimental fringe patterns for frames (a) k = 5, (b) k = 15 and (c) k = 30. Estimated phase derivative in radians/pixel for frames (d) k = 5, (e) k = 15 and (f) k = 30. The cosine fringes of the estimated phase derivative for frames (g) k = 5, (h) k = 15 and (i) k = 30.

50

31AF03 Firewire CCD camera was used to record the fringe patterns. The membrane was dynamically deformed by applying a variable load.

As the membrane was being deformed, fringe patterns corresponding to different deformation states of the membrane were recorded in the form of a video by the CCD camera. The frame rate of the camera was 15 frames/second. For the analysis, 36 frames were used and the fringe patterns corresponding to frames k = 5, 15 and 30 are shown in Fig.6.4(a)-(c). The estimated phase derivatives in radians/pixel using the proposed method for the corresponding frames are shown in Fig.6.4(d)-(f). The cosine fringes of the estimated phase derivatives are shown in Fig.6.4(g)-(i). The change in the phase derivative is evident from these figures as the applied load is increased with time. Also, the increasing concentration of the cosine fringes of the phase derivative near the location of loading show the increasing nature of deformation.

The results validate the applicability of the proposed method for measurement of dynamically varying displacement derivatives. In addition, the computational efficiency of the PSWVD makes the method suitable for applications involving transient phenomena. The proposed method also exhibits the inherent advantages of the fringe projection techniques enabling its use in an industrial environment.

6.4 Dual color DHI for simultaneous multi-dimensional measurements

Simultaneous measurement of the multi-dimensional displacement derivatives is of great practical significance in DHI. In this section, the 2D-PSWVD method is used in a multi-color setup [130–132] to directly estimate the multiple phase derivatives related to the in-plane and out-of-plane displacement derivatives in DHI without requiring any unwrapping or differentiation operations. The technique relies on multi-directional illumination of the object with lasers of different wavelengths and digital recording of holograms using a three charge-coupled device (CCD) sensor camera i.e. 3-Color CCD with red, green and blue (RGB) channels. Since each channel records only the intensity associated with the corresponding wavelength, digital processing of the recorded hologram provides a reconstructed interference field along each channel. The phase derivative is subsequently obtained from the reconstructed interference field using 2D-PSWVD.

6.4.1 Theory

In the proposed method, a dual-beam illumination of the diffuse object is considered where red and green beams with wavelengths λ_r and λ_g are incident on the object as shown in Fig.6.5. The 3-color CCD camera is located at a distance d from the object. Every channel of the camera records the hologram formed by the superposition of the reference and object beams of the corresponding wavelength. Denoting the reference and object waves in the CCD plane $x'y'$ as $R_r(x',y')$ and $O_r(x',y')$ for red wavelength and $R_g(x',y')$ and $O_g(x',y')$ for green wavelength, the intensities recorded at the red and green channels of the CCD are given as

$$
\begin{aligned}
I_r(x',y') &= |R_r(x',y') + O_r(x',y')|^2 \\
&= I_{r0}(x',y') + R_r(x',y')O_r^*(x',y') + R_r^*(x',y')O_r(x',y')
\end{aligned}
\tag{6.20}
$$

$$
\begin{aligned}
I_g(x',y') &= |R_g(x',y') + O_g(x',y')|^2 \\
&= I_{g0}(x',y') + R_g(x',y')O_g^*(x',y') + R_g^*(x',y')O_g(x',y')
\end{aligned}
\tag{6.21}
$$

where $*$ denotes the complex conjugate, $I_{r0} = |R_r(x',y')|^2 + |O_r(x',y')|^2$ and $I_{g0} = |R_g(x',y')|^2 + |O_g(x',y')|^2$. The object wave-field at the object plane xy is numerically reconstructed using the Fresnel transform as [83]

$$
\begin{aligned}
\Gamma_{k0}(x,y) = {}& \frac{j}{\lambda_k d} \exp\left[\frac{-j\pi}{\lambda_k d}(x^2 + y^2)\right] \exp\left[\frac{-j2\pi d}{\lambda_k}\right] \\
& \int_{-\infty}^{\infty}\int_{-\infty}^{\infty} R_k(x',y')I_k(x',y') \exp\left[\frac{-j\pi}{\lambda_k d}(x'^2 + y'^2)\right] \exp\left[\frac{j2\pi}{\lambda_k d}(xx' + yy')\right] \text{dx'dy'}
\end{aligned}
\tag{6.22}
$$
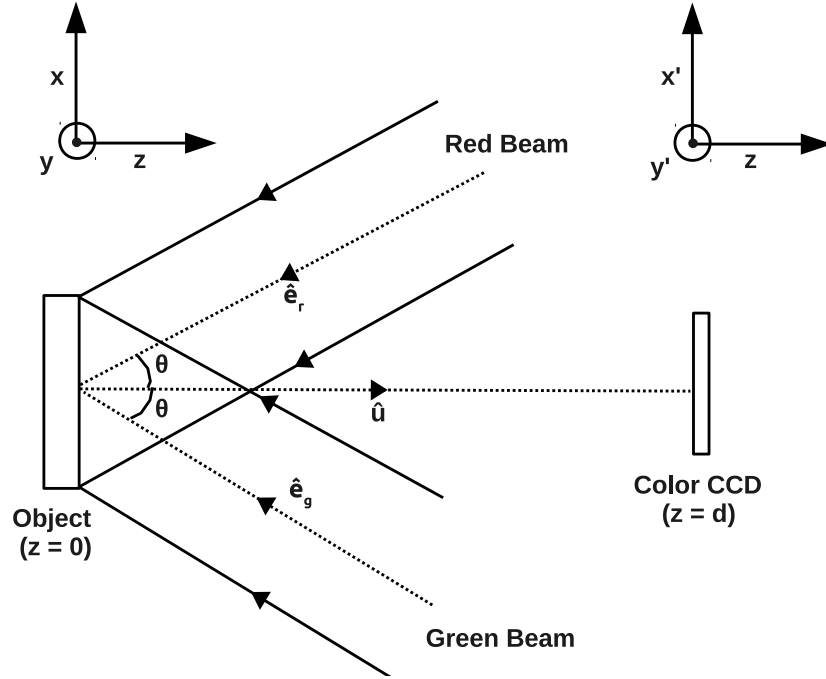
Fig. 6.5. Dual-beam illumination with red and green wavelengths.

where Γ_{k0} denotes the complex amplitude before object deformation. Here, the subscript k is used to indicate a particular color and $k = r$ or g depending on the red or green wavelength. For our analysis, the terms outside the integral can be neglected since they don't affect the overall interference phase and the above equation can be modified as

$$\Gamma_{k0}(x,y) = \int_{-\infty}^{\infty} \int_{-\infty}^{\infty} R_k(x',y') I_k(x',y') \exp\left[\frac{-j\pi}{\lambda_k d}(x'^2 + y'^2)\right] \exp\left[\frac{j2\pi}{\lambda_k d}(xx' + yy')\right] \mathrm{dx'dy'} \tag{6.23}$$

For a $N_x \times N_y$ pixels CCD camera with pixel sizes $\Delta x'$ and $\Delta y'$ along horizontal and vertical directions, the above equation can be discretized using a two-dimensional inverse Fourier transform and expressed as [83]

$$\Gamma_{k0}(m\Delta x_k, n\Delta y_k) = \sum_{p=0}^{N_x-1} \sum_{q=0}^{N_y-1} R_k(p\Delta x', q\Delta y') I_k(p\Delta x', q\Delta y') \exp\left[\frac{-j\pi}{\lambda_k d}((p\Delta x')^2 + (q\Delta y')^2)\right]$$

$$\exp\left[j2\pi\left(\frac{pm}{N_x} + \frac{qn}{N_y}\right)\right] \quad \forall\, m \in [0, N_x - 1], n \in [0, N_y - 1] \tag{6.24}$$

where Δx_k and Δy_k are the spatial resolutions in the xy plane and are given as

$$\Delta x_k = \frac{\lambda_k d}{N_x \Delta x'} \tag{6.25}$$

$$\Delta y_k = \frac{\lambda_k d}{N_y \Delta y'} \tag{6.26}$$

From the above equations, it is clear that the spatial resolutions Δx_k and Δy_k are functions of wavelength and are hence different for the red and green beams. Using the same procedure for numerical reconstruction as above, the complex amplitude of the object wave after deformation i.e. Γ_{k1} is calculated. Finally, the complex reconstructed interference field Γ_k is obtained by multiplying the post-deformation complex amplitude with the conjugate of pre-deformation complex amplitude. Substituting $x_k = m\Delta x_k$ and $y_k = n\Delta y_k$, we have,

$$\begin{aligned}
\Gamma_k(x_k, y_k) &= \Gamma_{k1}(x_k, y_k)\Gamma_{k0}^*(x_k, y_k) \\
&= a_k(x_k, y_k)\exp[j\phi_k(x_k, y_k)]
\end{aligned} \tag{6.27}$$

where a_k is the amplitude and ϕ_k is the interference phase for a given wavelength λ_k.

In Fig.6.5, the illumination unit vectors are $\hat{\mathbf{e}}_\mathbf{r}$ and $\hat{\mathbf{e}}_\mathbf{g}$ for the red and green beams and the observation unit vector is $\hat{\mathbf{u}}$. Hence, using Eq.(1.7), we have

$$\begin{aligned}
\phi_r &= \frac{2\pi}{\lambda_r}\vec{\mathbf{d}} \cdot (\hat{\mathbf{u}} - \hat{\mathbf{e}}_\mathbf{r}) \\
&= \frac{2\pi}{\lambda_r}[d_z(1 + \cos(\theta)) + d_x\sin(\theta)]
\end{aligned} \tag{6.28}$$

and

$$\begin{aligned}
\phi_g &= \frac{2\pi}{\lambda_g}\vec{\mathbf{d}} \cdot (\hat{\mathbf{u}} - \hat{\mathbf{e}}_\mathbf{g}) \\
&= \frac{2\pi}{\lambda_g}[d_z(1 + \cos(\theta)) - d_x\sin(\theta)]
\end{aligned} \tag{6.29}$$

Here d_x and d_z are the in-plane and out-of-plane displacement components. The spatial derivatives with respect to y could be written as

$$\frac{\partial\phi_r}{\partial y} = \frac{2\pi}{\lambda_r}\left[\frac{\partial d_z}{\partial y}(1 + \cos(\theta)) + \frac{\partial d_x}{\partial y}\sin(\theta)\right] \tag{6.30}$$

$$\frac{\partial\phi_g}{\partial y} = \frac{2\pi}{\lambda_g}\left[\frac{\partial d_z}{\partial y}(1 + \cos(\theta)) - \frac{\partial d_x}{\partial y}\sin(\theta)\right] \tag{6.31}$$

From the above two equations, we have

$$\lambda_r\frac{\partial\phi_r}{\partial y} + \lambda_g\frac{\partial\phi_g}{\partial y} = 4\pi\frac{\partial d_z}{\partial y}(1 + \cos(\theta)) \tag{6.32}$$

$$\lambda_r\frac{\partial\phi_r}{\partial y} - \lambda_g\frac{\partial\phi_g}{\partial y} = 4\pi\frac{\partial d_x}{\partial y}\sin(\theta) \tag{6.33}$$

The above equations clearly indicate that the in-plane and out-of-plane displacement derivatives can be estimated from the spatial phase derivatives $\partial\phi_r/\partial y$ and $\partial\phi_g/\partial y$ for the red and green beams. To obtain the phase derivative from the reconstructed interference field Γ_k, the 2D-PSWVD is used which is given using Eq.(4.3) as,

$$G_k(x_k, y_k, \omega_1, \omega_2) = \int_{-\infty}^{\infty}\int_{-\infty}^{\infty} w(\tau_1, \tau_2)\Gamma_k(x_k + \tau_1, y_k + \tau_2)\Gamma_k^*(x_k - \tau_1, y_k - \tau_2)$$
$$\exp[-2j(\omega_1\tau_1 + \omega_2\tau_2)]\,\mathrm{d}\tau_1\mathrm{d}\tau_2 \tag{6.34}$$

Here w is a real symmetric window function. For the analysis, a 33×33 Gaussian window was used. For 2D-PSWVD, the spatial frequencies $[\omega_1, \omega_2]$ at which the distribution attains its maximum correspond to the phase derivatives. In other words,

$$\left[\frac{\partial\phi_k(x_k, y_k)}{\partial x_k}, \frac{\partial\phi_k(x_k, y_k)}{\partial y_k}\right] = \arg\max_{\omega_1, \omega_2} G_k(x_k, y_k, \omega_1, \omega_2) \tag{6.35}$$

Using the above equation, the phase derivative can be estimated for the red and green wavelengths, i.e. for $k = r$ and g. Since the derivative is directly obtained, there is no further requirement of unwrapping or numerical differentiation operations. For the sake of convenience, the phase derivative would be henceforth denoted as ω_k in the chapter, where $\omega_k = \partial\phi_k/\partial y$.

It needs to be emphasized that the phase derivative ω_k is evaluated at spatial coordinates (x_k, y_k), which are different for the red and green beams since the spatial resolution $[\Delta x_k, \Delta y_k]$ depends on the wavelength λ_k. Consequently, the phase derivatives for the two wavelengths are evaluated on different grids and hence cannot be directly superimposed as in Eq.(6.32) and Eq.(6.33). This problem originates due to the use of the discrete Fourier transform in Eq.(6.24) which transforms the $(N_x - 1)\Delta x' \times (N_y - 1)\Delta y'$ grid in CCD plane to a $(N_x - 1)\Delta x_k \times (N_y - 1)\Delta y_k$ grid in the reconstruction plane with the grid resolution proportional to wavelength.

To mitigate this problem, an interpolation scheme is used in the proposed method since the spatial coordinates or grid points (x_k, y_k) are known for both wavelengths. Accordingly, the phase derivative obtained for the red wavelength is interpolated on the grid points corresponding to the green wavelength. With $\omega_g(x_g, y_g)$ and $\omega_r(x_r, y_r)$ as the estimated phase derivatives for the green and red wavelengths, the interpolated derivative $\omega_{\text{interp}}(x_g, y_g)$ is obtained by using MATLAB's 'interp2' function and can be written as

$$\omega_{\text{interp}}(x_g, y_g) = \text{interp2}(x_r, y_r, \omega_r(x_r, y_r), x_g, y_g, \text{'spline'}) \tag{6.36}$$

The 'interp2' function in the above equation interpolates the function $\omega_r(x_r, y_r)$ over the $x_g y_g$ grid using cubic spline interpolation in two-dimensions. After the interpolation, the phase derivative estimates for both wavelengths correspond to the same grid. Using Eq.(6.32) and Eq.(6.33), the information about out-of-plane and in-plane components of displacement derivative can be then obtained as,

$$\frac{\lambda_r\omega_{\text{interp}} + \lambda_g\omega_g}{4\pi(1 + \cos(\theta))} = \frac{\partial d_z}{\partial y} \tag{6.37}$$

55
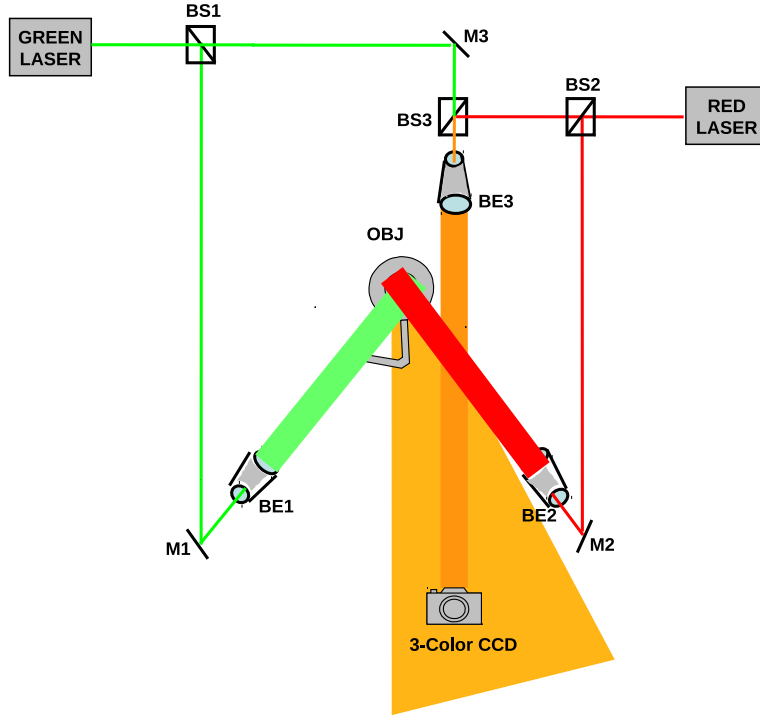
Fig. 6.6. Schematic of DHI setup with dual-color illumination. BS1-BS3: Beam splitters, BE1-BE3: Beam Expanders, M1-M3: Mirrors, OBJ: Object

$$\frac{\lambda_r \omega_{\mathrm{interp}} - \lambda_g \omega_g}{4\pi \sin(\theta)} = \frac{\partial d_x}{\partial y} \tag{6.38}$$

6.4.2   Experimental Results

The schematic (not drawn to scale) of the optical configuration is shown in Fig.6.6. The green and red beams from the lasers are split by the beam splitters BS1 and BS2 to obtain individual reference and object illumination beams. The reference beams for the red and green colors are combined via beam splitter BS3. For hologram recording, a 3-color CCD camera is used. The red and green channels of the camera store the intensity information related to the interference of the reference and object beams of the corresponding color. Effectively, each color channel records the hologram associated with the corresponding color at the same time, which permits simultaneous multi-color illumination of the object in the optical configuration.

To analyze the proposed method, a DHI experiment was performed where a clamped object was subjected to external loading and in-plane rotation. A Helium-Neon laser (633 nm) and a Coherent Verdi laser (532 nm) were used to generate the red and green

(a)

(b)

(c)

(d)

(e)

(f)
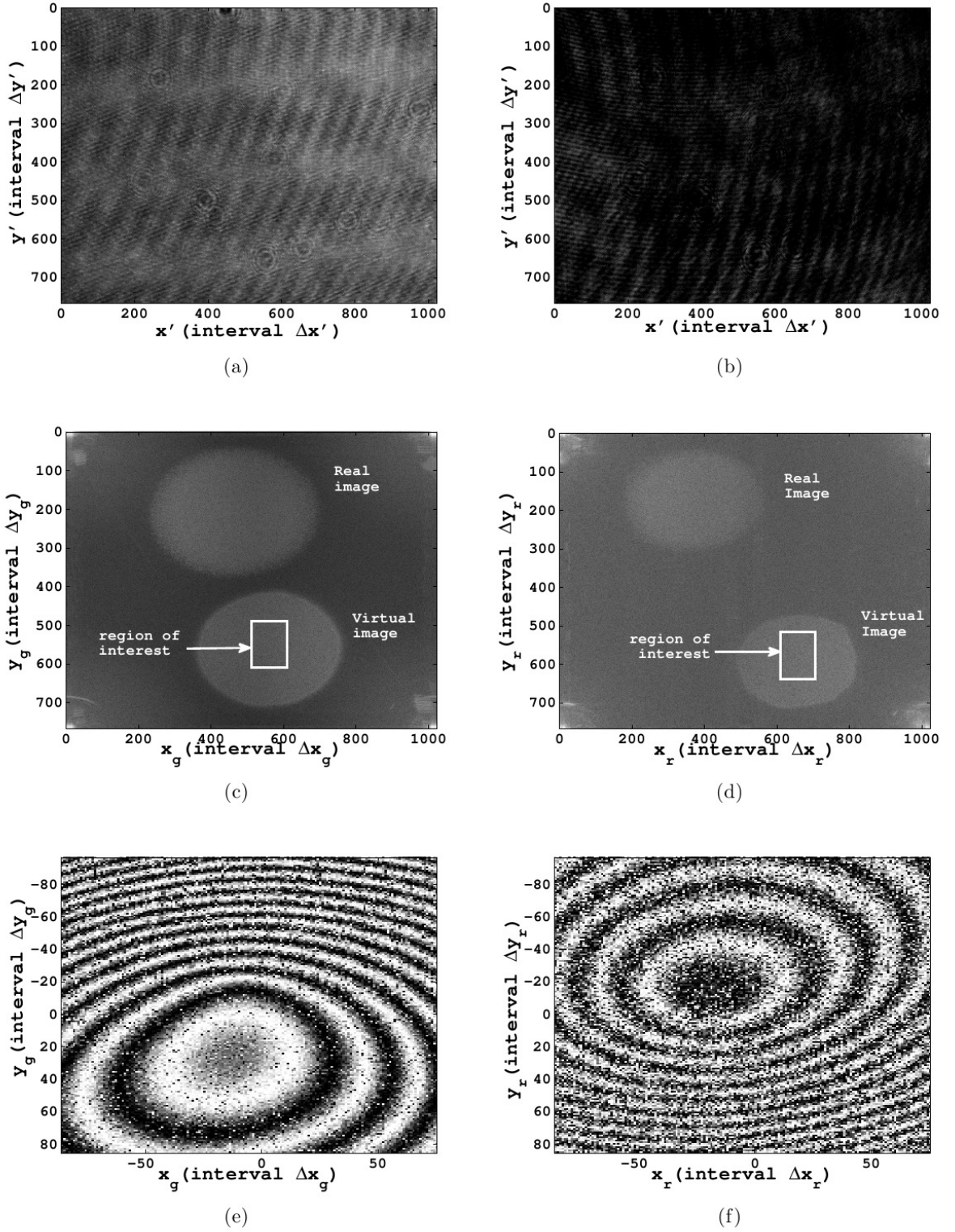
Fig. 6.7. (a) Intensity recorded in green channel. (b) Intensity recorded in red channel. (c) $|\Gamma_{g0}(x_g, y_g)|^2$ (d) $|\Gamma_{r0}(x_r, y_r)|^2$ (e) Fringe pattern for green wavelength. (f) Fringe pattern for red wavelength.

57

(a)

(b)

(c)

(d)

(e)
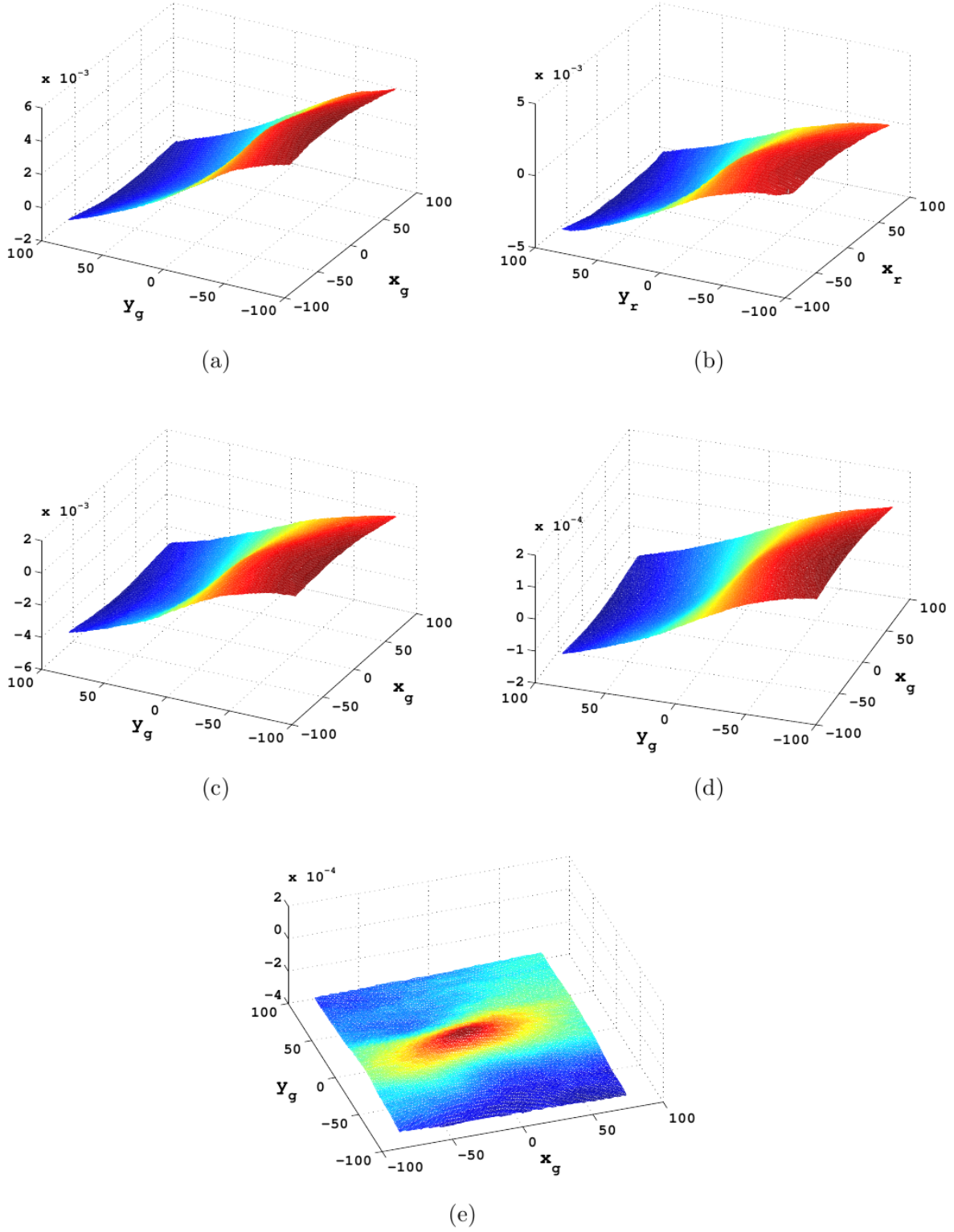
Fig. 6.8. Phase derivatives (a) $\omega_g(x_g, y_g)$, (b) $\omega_r(x_r, y_r)$ and (c) $w_{\text{interp}}(x_g, y_g)$ in radians/μm. (d) Out-of-plane displacement derivative. (e) In-plane displacement derivative.

58

beams. A JAI-M9-CL 3-CCD camera (1024 (horizontal) $\times$ 768 (vertical) pixels) with pixel resolution $[\Delta x', \Delta y'] = [4.65~\mu m, 4.65~\mu m]$ was used to record the holograms before and after object deformation. Because of the three color channels, every image recorded by the camera can be expressed in the form of a three-dimensional array of size 768 $\times$ 1024 $\times$ 3 where the third dimension signifies red, green or blue color information.

The intensities recorded in the green and red channels before object deformation are shown in Fig.6.7(a) and Fig.6.7(b). The complex amplitudes Γ_{g0} and Γ_{r0} are obtained for the green and red channels using discrete Fresnel transform and the corresponding intensities are shown in Fig.6.7(c) and Fig.6.7(d). The real and virtual images of the object are clearly visible in the figures. For the analysis, regions of interest were selected from the virtual images of the object for both wavelengths. The centre of the object served as the common origin i.e. spatial coordinate $(0, 0)$ for both regions though any other reference location such as a marked point on the object could be equivalently used. The reconstructed interference fields $\Gamma_g(x_g, y_g)$ and $\Gamma_r(x_r, y_r)$ were calculated using Eq.(6.27) and their real parts which constitute the fringe patterns are shown in Fig.6.7(e) and Fig.6.7(f) for the selected regions. In the above figures, the coordinates x_g and y_g for the green wavelength vary in steps or intervals of Δx_g and Δy_g whereas x_r and y_r for the red wavelength vary in intervals of Δx_r and Δy_r.

The phase derivative estimates $\omega_g(x_g, y_g)$ and $\omega_r(x_r, y_r)$ in radians/μm using 2D-PSWVD for the green and red wavelengths are shown in Fig.6.8(a) and Fig.6.8(b). The interpolated phase derivative for the red wavelength i.e. $\omega_{interp}(x_g, y_g)$ is shown in Fig.6.8(c). The out-of-plane and in-plane displacement derivatives obtained using Eq.(6.37) and Eq.(6.38) with $\theta = 30°$ are shown in Fig.6.8(d) and Fig.6.8(e).

The utility of the proposed method for practical applications is validated through the experimental results. The major advantage of the proposed method is the feasibility of simultaneous measurement of in-plane and out-of-plane displacement derivatives. In addition, the method directly provides phase derivative without requiring unwrapping operations, numerical differentiation and multiple data-frames.

6.5   Summary

This chapter highlighted some important applications of the PSWVD method in digital holographic interferometry and fringe projection. The robust performance of the method in these applications indicates its potential applicability in areas such as non-destructive testing and evaluation, condition monitoring, dynamic deformation analysis and quality assessment.

Chapter 7

Digital holographic moiré

7.1 Introduction

In the previous chapter, a multi-color optical configuration was presented for multi-dimensional deformation analysis in digital holographic interferometry. Though the setup permits simultaneous measurements, the experimental complexity might be high for some practical applications due to the requirement of lasers with different wavelengths and 3-color CCD camera. In addition, the cross-talk between the different color channels of the CCD poses challenges for accurate measurements. To address these limitations, the chapter introduces the concept of holographic moiré in DHI for simultaneous multi-dimensional deformation analysis. The holographic moiré configuration [133, 134] was originally proposed in classical holographic interferometry for the simultaneous measurement of in-plane and out-of-plane displacement components [135–145].

In the digital holographic moiré method, only a single reference beam and multiple object beams are required in an off-axis DHI configuration to record a hologram. By digital processing of the recorded holograms before and after deformation, moiré fringes are obtained which contain information about multiple interference phases corresponding to the different object beams. Demodulation of the moiré fringe pattern and subsequent use of sensitivity vectors enables multi-dimensional measurements.

7.2 Theory

To analyze multi-directional illumination of a diffuse object, consider Fig.7.1 where the object is illuminated by two light beams. The beams are assumed to be incident symmetrically on the object with respect to the observation direction. The CCD camera is located at a distance d from the object. In the proposed method, a single reference beam is used in conjunction with the diffusely scattered multiple object beams to record the

hologram at the CCD plane $x'y'$. Denoting the reference and object waves at the CCD as $R(x', y')$, $O_1(x', y')$ and $O_2(x', y')$, the intensity recorded at the CCD camera is given as

$$
\begin{aligned}
I &= |R + O_1 + O_2|^2 \\
&= I_0 + R(O_1^* + O_2^*) + R^*(O_1 + O_2)
\end{aligned}
\tag{7.1}
$$

where $I_0 = |R|^2 + |O_1|^2 + |O_2|^2 + O_1 O_2^* + O_1^* O_2$ and '*' denotes the complex conjugate. Here the spatial coordinate (x', y') is omitted for the sake of brevity. The complex amplitude of the object wave at the xy plane is provided by the Fresnel transformation and is given as [83]

$$
\begin{aligned}
\Gamma_0(x, y) =&\frac{j}{\lambda d} \exp\left[\frac{-j2\pi d}{\lambda}\right] \int_{-\infty}^{\infty} \int_{-\infty}^{\infty} R(x', y') I(x', y') \\
&\exp\left[\frac{-j\pi}{\lambda d}((x - x')^2 + (y - y')^2)\right] \mathrm{dx'dy'}
\end{aligned}
\tag{7.2}
$$

Using Eq.(7.1), we have

$$
\begin{aligned}
\Gamma_0(x, y) =&\frac{j}{\lambda d} \exp\left[\frac{-j2\pi d}{\lambda}\right] \int_{-\infty}^{\infty} \int_{-\infty}^{\infty} [RI_0 + R^2(O_1^* + O_2^*) + |R|^2(O_1 + O_2)] \\
&\exp\left[\frac{-j\pi}{\lambda d}((x - x')^2 + (y - y')^2)\right] \mathrm{dx'dy'}
\end{aligned}
\tag{7.3}
$$

For an off-axis configuration, the contributions arising from the terms RI_0, $R^2(O_1^* + O_2^*)$ and $|R|^2(O_1 + O_2)$ while calculating the intensity $|\Gamma_0(x, y)|^2$ would be spatially separable. This case is similar to the separability of the d.c., real and virtual images in off-axis digital holography due to the inclination of the reference beam with respect to the optical axis of the object [1]. Hence, focusing on the contribution from $|R|^2(O_1 + O_2)$, the complex amplitude before deformation can be written as,

$$
\Gamma_1(x, y) = a_1(x, y) \exp[j\psi_1(x, y)] + a_2(x, y) \exp[j\psi_2(x, y)]
\tag{7.4}
$$

Here $\psi_1(x, y)$ and $\psi_2(x, y)$ are random phases corresponding to the two scattered object waves. After object deformation, the complex amplitude can be written as,

$$
\Gamma_2(x, y) = a_1(x, y) \exp[j(\psi_1(x, y) + \phi_1(x, y))] + a_2(x, y) \exp[j(\psi_2(x, y) + \phi_2(x, y))]
\tag{7.5}
$$

where $\phi_1(x, y)$ and $\phi_2(x, y)$ are the phase changes in the two object waves due to deformation and are usually referred as *interference phases* in DHI. Subsequently, the reconstructed interference field can be obtained by multiplying the post-deformation complex amplitude of the object wave with the complex conjugate of pre-deformation complex amplitude. In other words, we have

$$
\begin{aligned}
\Gamma(x, y) =& \Gamma_2(x, y) \Gamma_1^*(x, y) \\
=& a_1^2(x, y) \exp[j\phi_1(x, y)] + a_2^2(x, y) \exp[j\phi_2(x, y)] \\
&+ a_1(x, y) a_2(x, y) \exp[j(\phi_1(x, y) + \psi_1(x, y) - \psi_2(x, y))] \\
&+ a_1(x, y) a_2(x, y) \exp[j(\phi_2(x, y) + \psi_2(x, y) - \psi_1(x, y))]
\end{aligned}
\tag{7.6}
$$
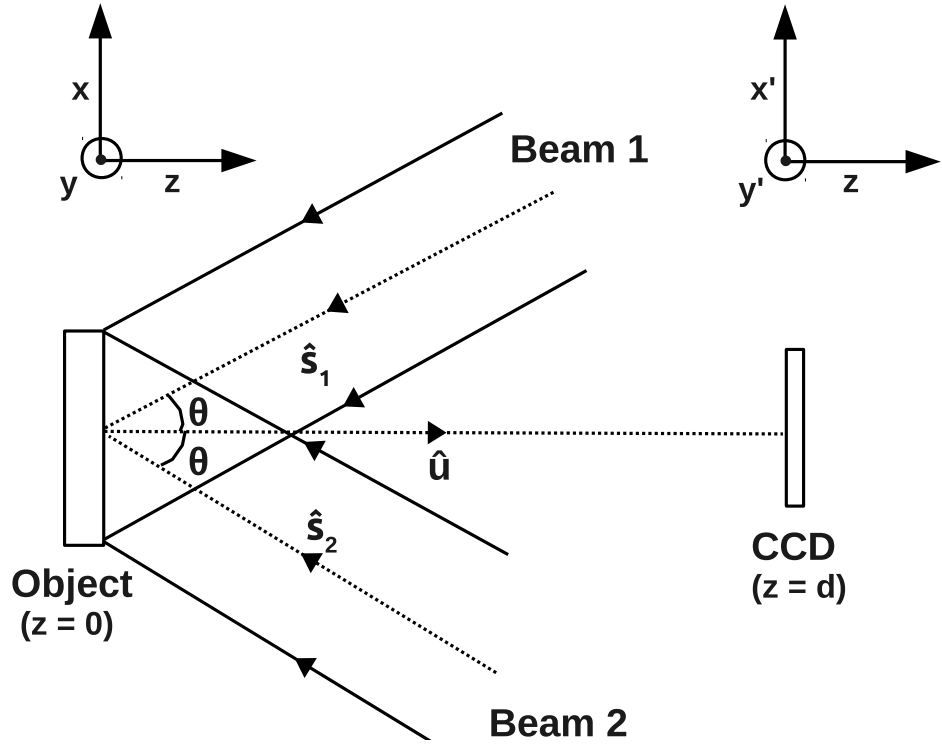
Fig. 7.1. Multi-beam illumination of the object

Here, the last two terms exhibit random behavior due to the presence of random phases $\psi_1(x, y)$ and $\psi_2(x, y)$ and hence can be considered as part of noise. Finally, the reconstructed interference field in the above equation can be modeled as

$$\Gamma(x, y) = a(x, y) \exp[j\phi_1(x, y)] + b(x, y) \exp[j\phi_2(x, y)] + \eta(x, y) \tag{7.7}$$

where $\eta(x, y)$ is the noise term. The reconstructed interference field $\Gamma(x, y)$ could be interpreted as the sum of two complex signals whose arguments are the interference phases. Hence, the real part of $\Gamma(x, y)$ constitutes a moiré fringe pattern which encodes information about the two interference phases $\phi_1(x, y)$ and $\phi_2(x, y)$.

In Fig.7.1, $\hat{\mathbf{s}}_1$ and $\hat{\mathbf{s}}_2$ denote the unit vectors along the illumination directions whereas $\hat{\mathbf{u}}$ indicates the unit vector along the observation direction. For the simplicity of analysis, a two-dimensional case is considered where all the unit vectors are limited to xz plane. So we have,

$$\hat{\mathbf{s}}_1 = -\sin(\theta)\hat{\mathbf{x}} - \cos(\theta)\hat{\mathbf{z}} \tag{7.8}$$

$$\hat{\mathbf{s}}_2 = \sin(\theta)\hat{\mathbf{x}} - \cos(\theta)\hat{\mathbf{z}} \tag{7.9}$$

$$\hat{\mathbf{u}} = \hat{\mathbf{z}} \tag{7.10}$$

Here $\hat{\mathbf{x}}$ and $\hat{\mathbf{z}}$ denote the unit vectors along x and z. The displacement of the object is denoted by the vector $\vec{\mathbf{d}} = d_x\hat{\mathbf{x}} + d_z\hat{\mathbf{z}}$ with d_z and d_x as the out-of-plane and in-plane components. Using Eq.(1.7), we have

$$\begin{aligned} \phi_1 &= \frac{2\pi}{\lambda}\vec{\mathbf{d}} \cdot (\hat{\mathbf{u}} - \hat{\mathbf{s}}_\mathbf{1}) \\ &= \frac{2\pi}{\lambda}\left[d_z(1 + \cos(\theta)) + d_x \sin(\theta)\right] \end{aligned} \tag{7.11}$$

and

$$\begin{aligned} \phi_2 &= \frac{2\pi}{\lambda}\vec{\mathbf{d}} \cdot (\hat{\mathbf{u}} - \hat{\mathbf{s}}_\mathbf{2}) \\ &= \frac{2\pi}{\lambda}\left[d_z(1 + \cos(\theta)) - d_x \sin(\theta)\right] \end{aligned} \tag{7.12}$$

From the above equations, we have

$$\phi_1 + \phi_2 = \frac{4\pi}{\lambda}d_z(1 + \cos(\theta)) \tag{7.13}$$

$$\phi_1 - \phi_2 = \frac{4\pi}{\lambda}d_x \sin(\theta) \tag{7.14}$$

It is clear from above equations that the out-of-plane and in-plane displacement components d_z and d_x can be estimated from the sum and difference of the interference phases encoded in the moiré fringe pattern. So, the problem of measurement of multi-dimensional displacement components boils down to demodulation of digital holographic moiré (DHM) fringes.

Reliable estimation of $\phi_1(x, y)$ and $\phi_2(x, y)$ from Eq.(7.7) is a challenging task. The usual 'arctan' operation in DHI for finding the interference phase i.e. $\arctan\left[\frac{\text{Im}\{\Gamma(x,y)\}}{\text{Re}\{\Gamma(x,y)\}}\right]$ with 'Im' and 'Re' indicating the imaginary and real parts would be unreliable since $\Gamma(x, y)$ is the sum of two complex signals. Similarly, analysis in the frequency domain by calculating the Fourier transform (FT) of $\Gamma(x, y)$ would be error-prone due to the overlap between the spectra of the two complex signals. However, this problem could be solved by introducing a spatial carrier in one of the object beams by tilting a mirror in the path of the object beam for one deformation state. For instance, if the spatial carrier is introduced in the first object beam while recording the hologram in one object state, say after deformation, then Eq.(7.5) is modified as

$$\begin{aligned} \Gamma_2(x, y) &= a_1(x, y)\exp[j(\omega_1 x + \omega_2 y + \psi_1(x, y) + \phi_1(x, y))] \\ &\quad + a_2(x, y)\exp[j(\psi_2(x, y) + \phi_2(x, y))] \end{aligned} \tag{7.15}$$

where $[\omega_1, \omega_2]$ is the introduced carrier frequency. Consequently, Eq.(7.7) is modified as

$$\Gamma(x, y) = a(x, y)\exp[j(\omega_1 x + \omega_2 y + \phi_1(x, y))] + b(x, y)\exp[j\phi_2(x, y)] + \eta(x, y) \tag{7.16}$$

64

By taking the two-dimensional FT, we have

$$
\begin{aligned}
G(\omega_x, \omega_y) &= \mathrm{FT}\{\Gamma(x,y)\} \\
&= G_1(\omega_x - \omega_1, \omega_y - \omega_2) + G_2(\omega_x, \omega_y) + N(\omega_x, \omega_y)
\end{aligned}
\tag{7.17}
$$

where

$$
G_1(\omega_x, \omega_y) = \mathrm{FT}\{a(x,y)\exp[j(\phi_1(x,y))]\}
\tag{7.18}
$$

$$
G_2(\omega_x, \omega_y) = \mathrm{FT}\{b(x,y)\exp[j\phi_2(x,y)]\}
\tag{7.19}
$$

$$
N(\omega_x, \omega_y) = \mathrm{FT}\{\eta(x,y)\}
\tag{7.20}
$$

Due to the presence of carrier frequency $[\omega_1, \omega_2]$, the Fourier spectra corresponding to $G_1(\omega_x - \omega_1, \omega_y - \omega_2)$ and $G_2(\omega_x, \omega_y)$ are separated in the frequency domain and concentrated around $[\omega_1, \omega_2]$ and zero frequencies. Hence by spectral filtering and inverse Fourier transform [24], we obtain the individual complex signals $g_1(x,y) = a(x,y)\exp[j(\phi_1(x,y))]$ and $g_2(x,y) = b(x,y)\exp[j(\phi_2(x,y))]$. Subsequently, the interference phases can be obtained using,

$$
\begin{aligned}
\phi_1(x,y) &= \mathrm{angle}\{g_1(x,y)\} \\
&= \arctan\left[\frac{\mathrm{Im}\{g_1(x,y)\}}{\mathrm{Re}\{g_1(x,y)\}}\right]
\end{aligned}
\tag{7.21}
$$

and

$$
\begin{aligned}
\phi_2(x,y) &= \mathrm{angle}\{g_2(x,y)\} \\
&= \arctan\left[\frac{\mathrm{Im}\{g_2(x,y)\}}{\mathrm{Re}\{g_2(x,y)\}}\right]
\end{aligned}
\tag{7.22}
$$

It is to be noted that the estimates obtained using above equations are wrapped and hence unwrapping operation is required to obtain continuous phase distributions.

In addition to phase, estimation of the multiple phase derivatives from a moiré fringe pattern is highly desired. Since the individual complex signals $g_1(x,y)$ and $g_2(x,y)$ are available after spectral filtering, the pseudo Wigner-Ville distribution (PSWVD) method is applied to estimate the individual phase derivatives. It needs to be emphasized that, unlike phase estimation above, the PSWVD method provides direct estimates of the phase derivatives without the need of unwrapping operation.

7.3 Simulation Analysis

To analyze the proposed method, a complex reconstructed interference field was simulated as,

$$
\begin{aligned}
\Gamma(x,y) &= g_1(x,y) + g_2(x,y) \\
&= \exp[j\phi_1(x,y)] + \exp[j\phi_2(x,y)]
\end{aligned}
\tag{7.23}
$$

(a) (b)

(c) (d)
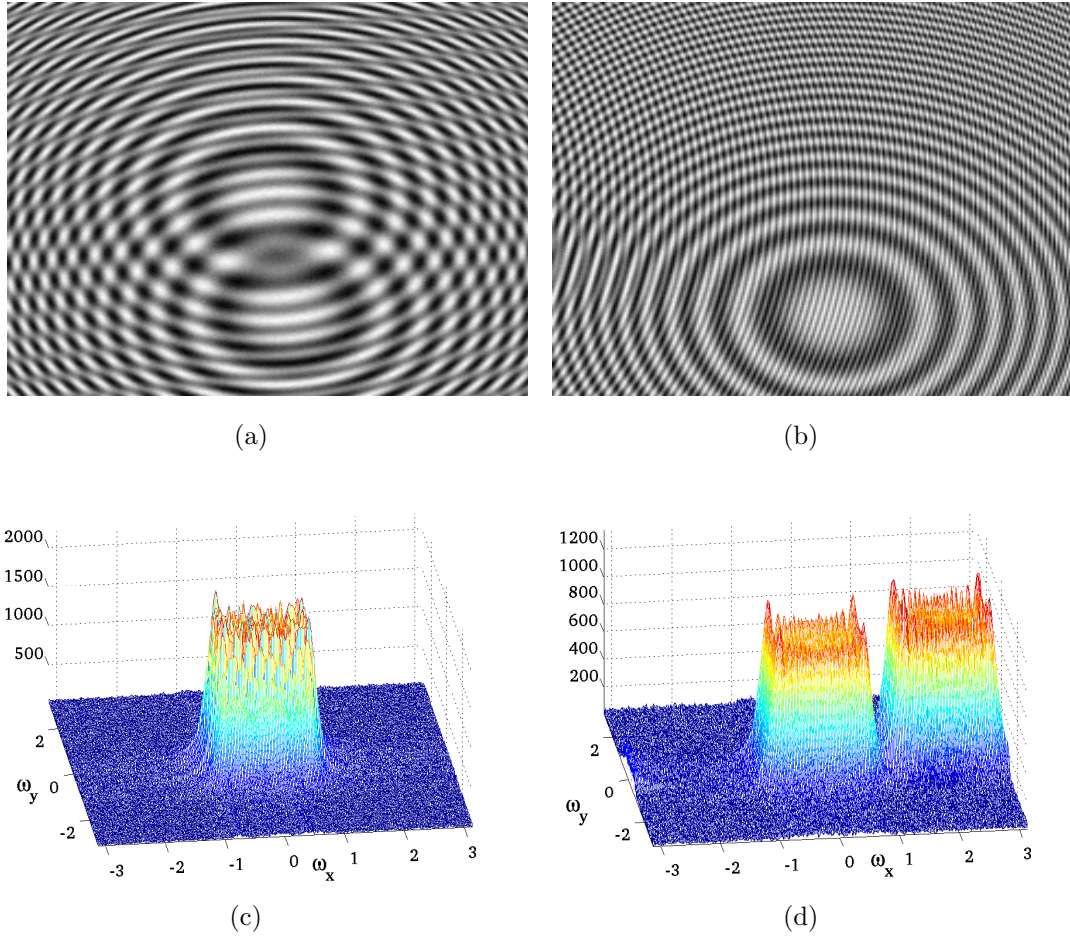
Fig. 7.2. (a) Moiré fringe pattern corresponding to $\Gamma(x, y)$. (b) Moiré fringe pattern corresponding to $\Gamma_c(x, y)$. (c) Fourier spectrum of $\Gamma(x, y)$. (d) Fourier spectrum of $\Gamma_c(x, y)$

which could be interpreted as the sum of two components $g_1(x, y)$ and $g_2(x, y)$. Here x and y denote the pixels along the horizontal and vertical directions. Similarly, another complex signal was generated by associating a spatial carrier with frequency $[\omega_1, 0]$ to $g_1(x, y)$ as,

$$
\begin{aligned}
\Gamma_c(x, y) &= g_1(x, y) \exp[j\omega_1 x] + g_2(x, y) \\
&= \exp[j(\omega_1 x + \phi_1(x, y))] + \exp[j\phi_2(x, y)]
\end{aligned} \tag{7.24}
$$

For the analysis, noise was added at SNR of 20 dB using MATLAB's 'awgn' function.

The real part of $\Gamma(x, y)$ which constitutes the moiré fringe pattern is shown in Fig.7.2(a). Similarly, the real part of $\Gamma_c(x, y)$ which corresponds to the moiré fringe pattern in presence of carrier is shown in Fig.7.2(b). The two-dimensional Fourier spectra corresponding to $\Gamma(x, y)$ and $\Gamma_c(x, y)$ are shown in Fig.7.2(c) and Fig.7.2(d). It is clear that the spectra of $g_1(x, y)$ and $g_2(x, y)$ overlap in Fig.7.2(c) whereas their spectra are quite separable in
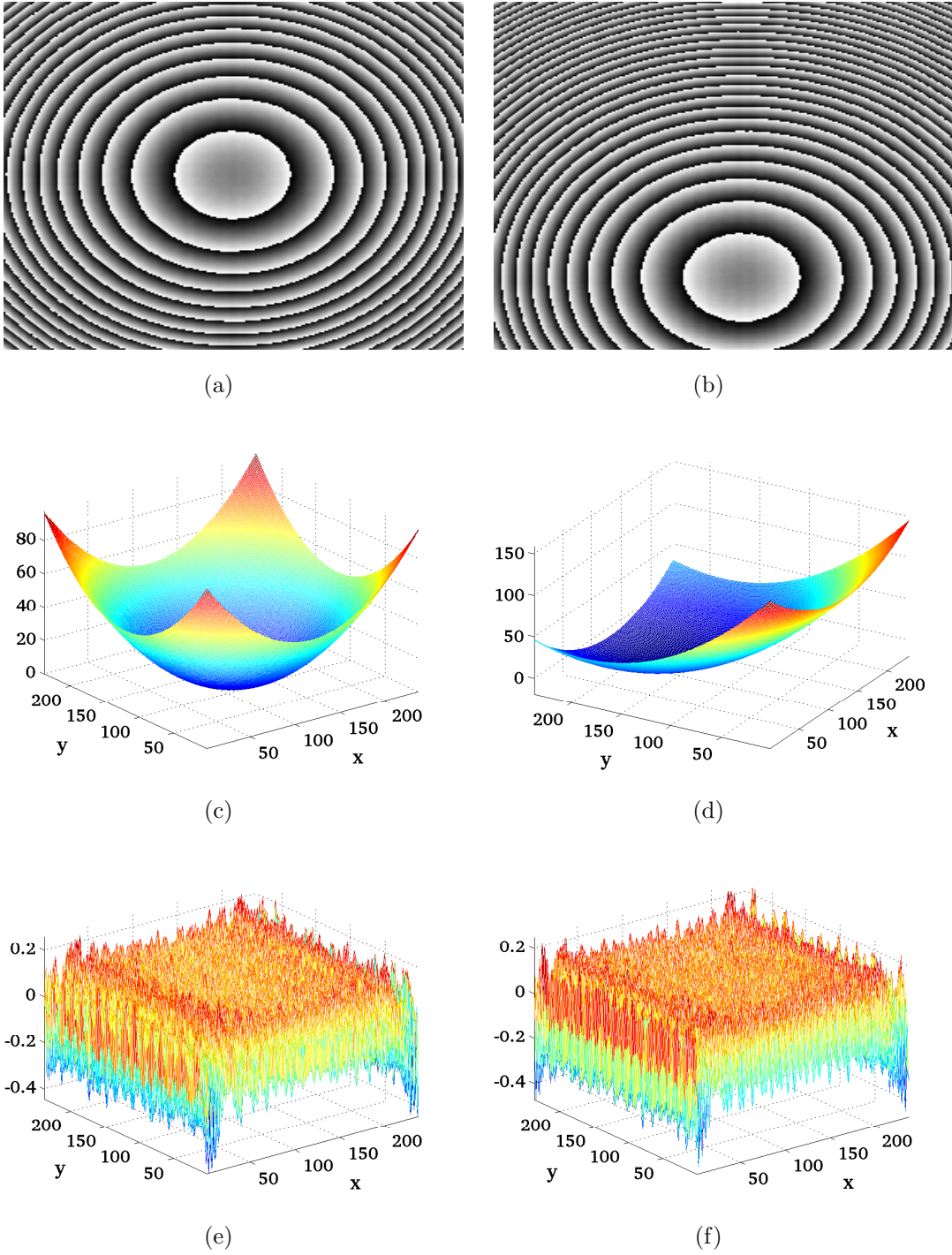
Fig. 7.3. (a) Wrapped estimate of first phase $\phi_1(x, y)$. (b) Wrapped estimate of second phase $\phi_2(x, y)$ in radians. (c) Unwrapped $\phi_1(x, y)$ in radians. (d) Unwrapped $\phi_2(x, y)$ in radians. (e) Estimation error for first phase in radians. (f) Estimation error for second phase in radians.

67
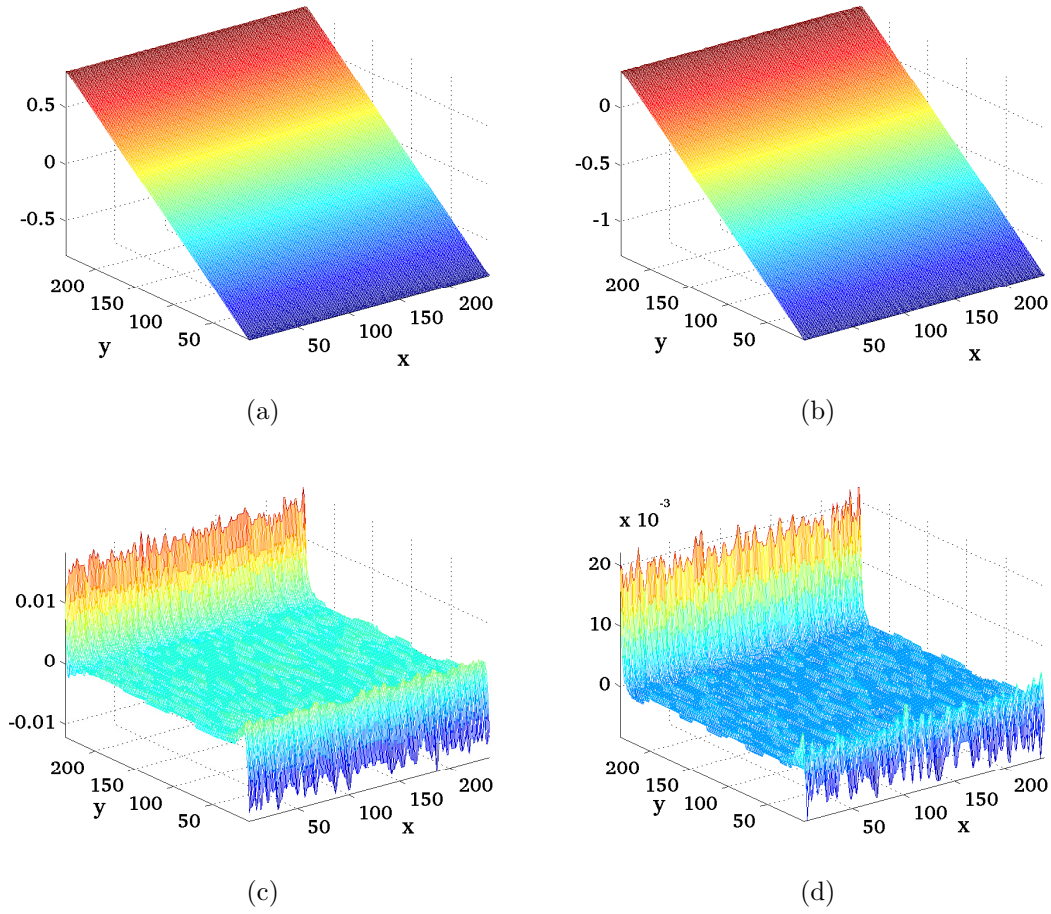
Fig. 7.4. (a) Estimated first phase derivative $\phi_{1y}(x,y)$ in radians/pixel. (b) Estimated second phase derivative $\phi_{2y}(x,y)$ in radians/pixel. (c) Estimation error for the first phase derivative in radians/pixel. (d) Estimation error for the second phase derivative in radians/pixel.

Fig.7.2(d) due to the presence of a spatial carrier. The main advantage of inclusion of carrier in one of the components is the ensuing spectral separability in frequency domain, which permits the retrieval of individual components.

By Fourier filtering and inverse Fourier transform, the components $g_1(x,y)$ and $g_2(x,y)$ are recovered and their corresponding wrapped phases are obtained using Eq.(7.21) and Eq.(7.22). The wrapped estimates of $\phi_1(x,y)$ and $\phi_2(x,y)$ are shown in Fig.7.3(a) and Fig.7.3(b). The continuous phase distributions in radians after unwrapping are shown in Fig.7.3(c) and Fig.7.3(d). The root mean square errors for the estimation of the phases $\phi_1(x,y)$ and $\phi_2(x,y)$ were 0.0820 and 0.0808 radians.

Applying the PSWVD method, the estimated phase derivatives $\phi_{1y}(x,y)$ and $\phi_{2y}(x,y)$ in radians/pixel are shown in Fig.7.4(a) and Fig.7.4(b). The corresponding estimation errors are shown in Fig.7.4(c) and Fig.7.4(d). The root mean square errors for the estimation
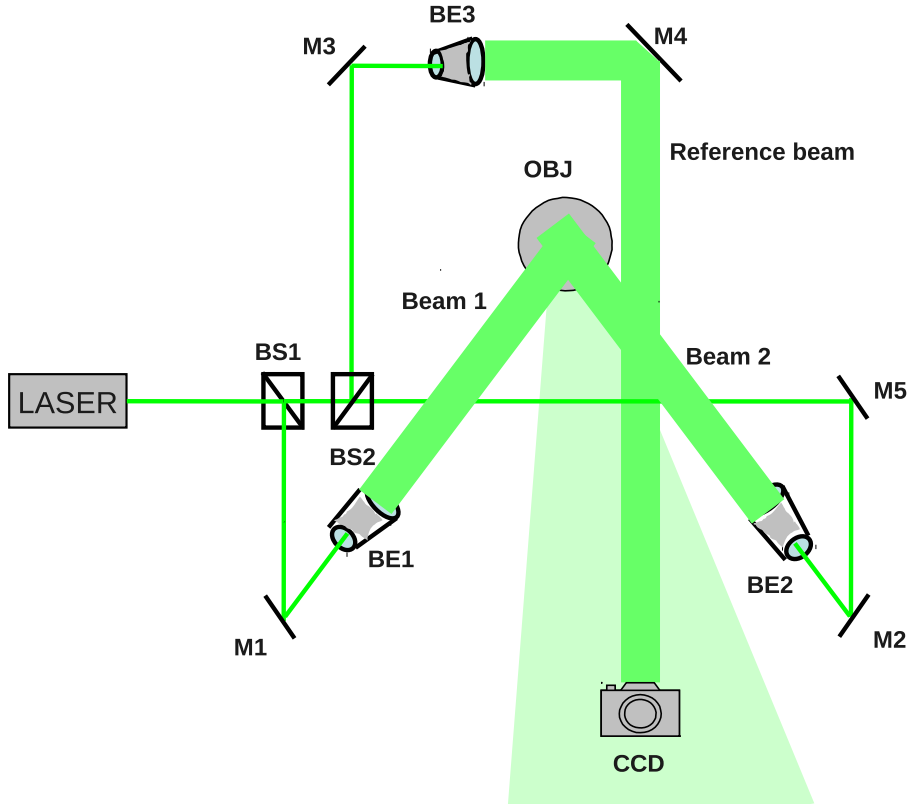
Fig. 7.5. DHM schematic (BS1-BS2: Beam Splitters, BE1-BE3: Beam Expanders, M1-M5: Mirrors, OBJ: Diffuse Object).

of the phase derivatives $\phi_{1y}(x, y)$ and $\phi_{2y}(x, y)$ were 0.0017 and 0.0016 radians/pixel.

7.4 Experimental Results

The general schematic (not drawn to scale) of the DHM optical configuration is shown in Fig.7.5. The light from the laser is divided by the beam splitter (BS1) into two beams. One beam is incident on mirror M1 to be used as the object illumination beam 1 through the path M1-BE1-OBJ. The second beam passes through another beam splitter (BS2) to be further divided into another two beams to be used as the reference beam (through M3-BE3-M4-CCD) and the object illumination beam 2 (through M5-M2-BE2-OBJ). The illumination beams are diffusely scattered by the object. The CCD records the hologram formed by the superposition of the reference and diffusely scattered object beams.

For the experiment, a Coherent Verdi laser (532 nm) was used as the light source. A SONY XCL-U1000 (1600 × 1200 pixels) CCD camera was used for the recording of holograms.

69

(a)

(b)

(c)

(d)
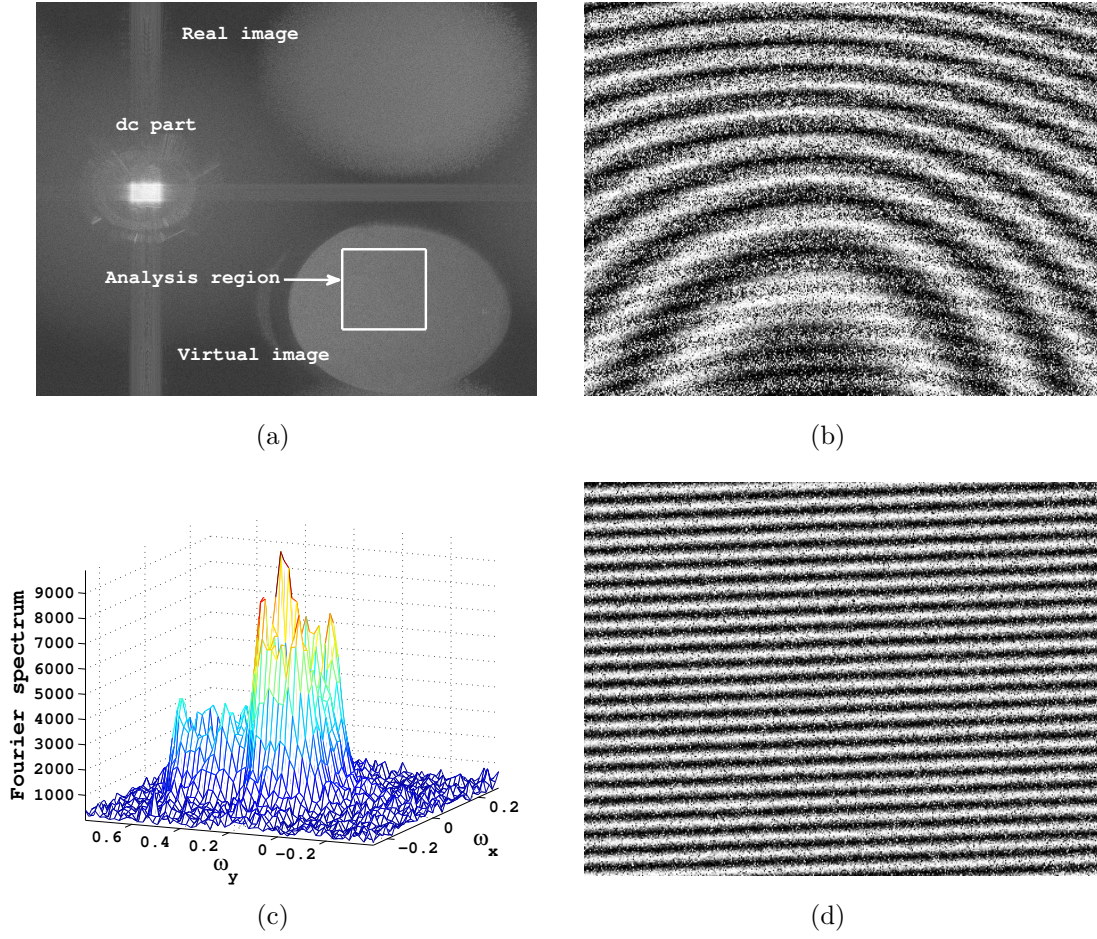
Fig. 7.6. (a) Intensity of the numerically reconstructed hologram using discrete Fresnel transform. (b) DHM fringe pattern. (c) 2D FT of $\Gamma(x,y)$. (d) Carrier fringes.

The object was deformed by applying external load as well as in-plane rotation. The carrier was introduced in the first object wave by the tilt of the mirror M1. Two holograms were recorded corresponding to the object states before and after deformation. The numerical reconstruction was performed using discrete Fresnel transform [83] to obtain the complex amplitudes $\Gamma_1(x,y)$ and $\Gamma_2(x,y)$.

The intensity of the complex amplitude before deformation i.e. $|\Gamma_1(x,y)|^2$ is shown in Fig.7.6(a) where the d.c part (undiffracted pattern) and the real and virtual images of the object are visible. Without loss of generality, a finite region was selected from the virtual image for analysis as shown in Fig.7.6(a). The complex reconstructed interference field i.e. $\Gamma(x,y)$ was obtained by multiplying the post-deformation complex amplitude with the complex conjugate of pre-deformation complex amplitude. The real part of the reconstructed interference field constitutes the DHM fringe pattern shown in Fig.7.6(b). The DHM fringes encode information about the desired phases $\phi_1(x,y)$ and $\phi_2(x,y)$. To recover the phase information, the 2D Fourier transform of $\Gamma(x,y)$ was calculated and the

70
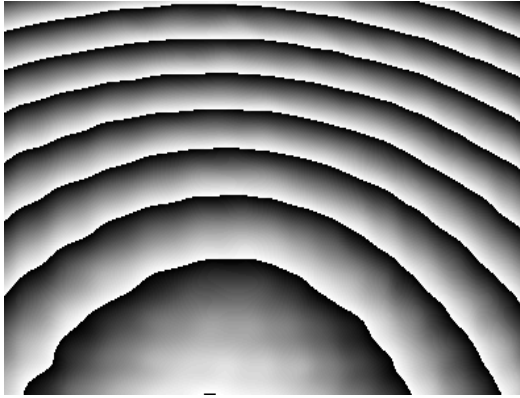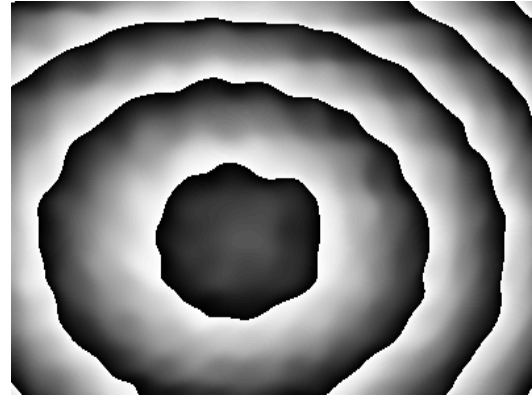
(a)   (b)
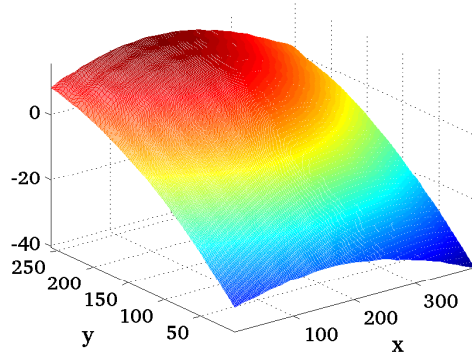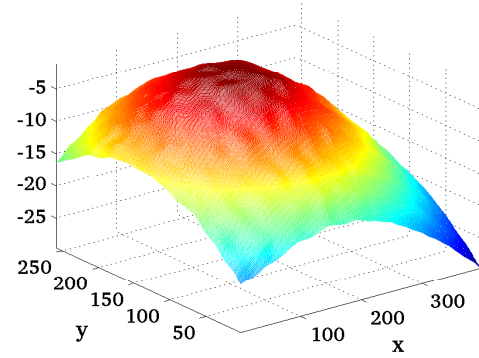
(c)   (d)
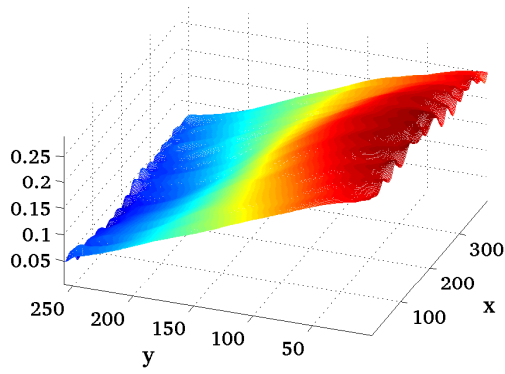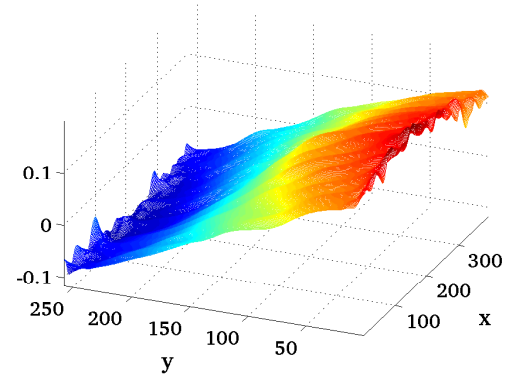
(e)   (f)

Fig. 7.7. (a) Wrapped estimate of $\phi_1(x,y)$. (b) Wrapped estimate of $\phi_2(x,y)$. (c) Unwrapped $\phi_1(x,y)$ in radians. (d) Unwrapped $\phi_2(x,y)$ in radians. (e) Estimated $\phi_{1y}(x,y)$ in radians/pixel. (f) Estimated $\phi_{2y}(x,y)$ in radians/pixel.

71

corresponding spectrum is shown in Fig.7.6(c) where two distinct spectral regions due to individual components are visible.

To separate the spectra of individual components efficiently, the carrier frequency was also estimated in the experiment. Since the carrier was introduced in only one of the object waves by the tilt of the mirror, it was estimated by recording two holograms before and after tilting the mirror for the same object state with the second object wave blocked and subsequently using numerical reconstruction to generate the complex signals. The carrier signal was then obtained by multiplying the post-tilt complex signal with the conjugate of pre-tilt complex signal. Mathematically speaking, this operation is equivalent to setting $b(x, y) = 0$ (since second object wave was blocked) and $\phi_1(x, y) = 0$ (since both holograms were recorded for the same object state) in Eq.(7.16) to obtain a complex carrier signal $c(x, y) = a(x, y) \exp[j(\omega_1 x + \omega_2 y)]$ from which the carrier frequency could be estimated using Fourier transform. The carrier fringes constituted by the real part of the complex carrier signal thus obtained are shown in Fig.7.6(d) for the sake of illustration. It needs to be emphasized that the carrier estimation procedure needs to be performed only once and the obtained information about the carrier frequency could be used for many subsequent deformation measurements of the object as long as the optical configuration remains the same.

Subsequently, the individual components $g_1(x, y)$ and $g_2(x, y)$ were obtained by spatial filtering and inverse Fourier transform and the wrapped phase estimates of $\phi_1(x, y)$ and $\phi_2(x, y)$ obtained using Eq.(7.21) and Eq.(7.22) are shown in Fig.7.7(a) and Fig.7.7(b). The corresponding continuous phase distributions in radians obtained after unwrapping are shown in Fig.7.7(c) and Fig.7.7(d). Similarly, the estimated phase derivatives $\phi_{1y}(x, y)$ and $\phi_{2y}(x, y)$ in radians/pixel are shown in Fig.7.7(e) and Fig.7.7(f).

7.5   Summary

In the chapter, the holographic moiré technique is presented for multi-dimensional deformation analysis in digital holographic interferometry. The simulation and experimental results validate the potential of the proposed technique. In comparison with the existing state-of-the-art techniques for multi-dimensional deformation measurements in DHI, the proposed technique enjoys the following advantages:

1. The proposed method does not require multiple reference beams or CCDs for recording holograms. This simplifies the optical configuration for multi-dimensional deformation measurements.

2. In the proposed technique, information about multiple phases and their derivatives is extracted without requiring multiple data-frames, in contrast with the phase-shifting technique based methods. This improves robustness against vibrations and external disturbances.

3. The proposed technique enables *simultaneous* estimation of multiple phases and derivatives which makes it highly suitable for measurements where multiple components of the displacement or its derivatives have to be measured at the same time.

The feasibility of multi-dimensional deformation analysis from DHM fringes provided by the proposed method could have a strong impact on the use of digital holographic interferometry for many practical applications in areas such as experimental mechanics and non-destructive testing.

Chapter 8

Multi-component polynomial phase formulation

8.1 Introduction

In the previous chapter, the concept of digital holographic moiré was introduced, where a single moiré fringe pattern encodes information about multiple phases, which are related to the multi-dimensional displacement components. The individual phase signals were separated through spectral filtering using a spatial carrier. However, such approach requires careful control of the carrier in the experimental setup to ensure sufficient spectral separation, which might be difficult in practice. In this chapter, a novel approach based on piecewise multi-component polynomial phase formulation is introduced which is capable of estimation of multiple phases and their derivatives from a moiré fringe pattern without the requirement of an additional spatial carrier.

8.2 Theory

As discussed in the previous chapter, the reconstructed interference field in DHM is given as

$$\Gamma(x,y) = A_1(x,y) \exp[j\phi_1(x,y)] + A_2(x,y) \exp[j\phi_2(x,y)] + \eta(x,y) \tag{8.1}$$

where $A_1(x,y)$ and $A_2(x,y)$ represent the amplitudes assumed to be slowly varying, $\eta(x,y)$ denotes the noise and $\phi_1(x,y)$ and $\phi_2(x,y)$ are the interference phases corresponding to the respective beams. Estimation of the individual phases $\phi_1(x,y)$ and $\phi_2(x,y)$ in Eq.(8.1) is a challenging problem since $\Gamma(x,y)$ is the sum of two complex signals. The applicability of the popular spatial fringe analysis methods based on Fourier transform [24], windowed Fourier transform [82] and wavelet transform [78] is limited to extracting a single phase

distribution from a fringe pattern and their accuracy would be strongly affected for the retrieval of dual phases due to the spectral overlap of the two complex signals in absence of a spatial carrier.

In the proposed method, the reconstructed interference field $\Gamma(x, y)$ is modeled as a piecewise multi-component polynomial phase signal to directly estimate the phases $\phi_1(x, y)$ and $\phi_2(x, y)$ and their derivatives. Accordingly, a given column/row of $\Gamma(x, y)$ is divided into say N_w segments and the phase of each component in every segment is approximated as a polynomial. Hence, for a given column x and segment i where $i \in [1, N_w]$, we have

$$\phi_{1i}(y) = \sum_{m=0}^{M} a_{im} y^m \tag{8.2}$$

$$\phi_{2i}(y) = \sum_{m=0}^{M} b_{im} y^m \tag{8.3}$$

$$\Gamma_i(y) = A_{1i}(y) \exp\left[j\left(\sum_{m=0}^{M} a_{im} y^m\right)\right] + A_{2i}(y) \exp\left[j\left(\sum_{m=0}^{M} b_{im} y^m\right)\right] + \eta_i(y) \tag{8.4}$$

Eq.(8.4) represents a multi-component polynomial phase signal of order M and the phases $\phi_{1i}(y)$ and $\phi_{2i}(y)$ in the ith segment can be obtained from the polynomial coefficients $[a_{i0}, \cdots, a_{iM}]$ and $[b_{i0}, \cdots, b_{iM}]$. Also, the phase derivatives can be given as,

$$\frac{\partial \phi_{1i}(y)}{\partial y} = \sum_{m=0}^{M} m a_{im} y^{m-1} \tag{8.5}$$

$$\frac{\partial \phi_{2i}(y)}{\partial y} = \sum_{m=0}^{M} m b_{im} y^{m-1} \tag{8.6}$$

To estimate these coefficients, product high-order ambiguity function (PHAF) [146] is used. The main advantage of using PHAF lies in its ability to suppress the unwanted interference caused due to multiple components, which leads to robust estimation of the desired coefficients.

The mth order PHAF is computed through the following steps [146]:

1. Initially, the high-order instantaneous moment (HIM) of mth order is calculated from $\Gamma_i(y)$ using a recursive operation,

$$x_1(y) = \Gamma_i(y),$$
$$x_2(y; \tau_{k,1}) = x_1(y) x_1^*(y - \tau_{k,1}),$$
$$\vdots$$
$$x_m(y; \tau_{k,m-1}) = x_{m-1}(y; \tau_{k,m-2}) x_{m-1}^*(y - \tau_{k,m-1}; \tau_{k,m-2}) \tag{8.7}$$

where '*' denotes complex conjugate and $\tau_{k,m-1}$ is the kth lag parameter.

2. Subsequently, the high-order ambiguity function (HAF) is obtained from the discrete Fourier transform (DFT) of the HIM as

$$X_m(\omega; \tau_{k,m-1}) = \text{DFT}[x_m(y; \tau_{k,m-1})]$$
$$= \sum_{y=0}^{N-1} x_m(y; \tau_{k,m-1}) \exp[-j\omega y] \tag{8.8}$$

   where N is the sample size. The obtained m^{th} order HAF i.e. $X_m(\omega; \tau_{k,m-1})$ corresponds to a particular lag parameter $\tau_{k,m-1}$.

3. The above steps are repeated for K different lag parameters i.e. $[\tau_{1,m-1}, \cdots, \tau_{K,m-1}]$ to obtain different HAFs corresponding to $k \in [1, K]$.

4. Finally, the multiple HAFs are scaled in frequency domain by the scaling factor $P_m(\tau_{k,m-1}, \tau_{1,m-1})$ and subsequently multiplied to obtain the mth order PHAF of $\Gamma_i(y)$ as

$$X_{K,m}(\omega) = \prod_{k=1}^{K} X_m(P_m(\tau_{k,m-1}, \tau_{1,m-1})\omega, \tau_{k,m-1}) \tag{8.9}$$

   where

$$P_m(\tau_{k,m-1}, \tau_{1,m-1}) = \left[\frac{\tau_{k,m-1}}{\tau_{1,m-1}}\right]^{m-1} \tag{8.10}$$

For the multi-component case, the interesting property of mth order PHAF is that its spectrum exhibits peaks corresponding to the mth order polynomial coefficients. For the dual component case of $\Gamma_i(y)$ in Eq.(8.4), if the maxima of the PHAF spectrum $|X_{K,m}(\omega)|$ occur at ω_{max}, then the coefficients a_{im} and b_{im} are given as,

$$a_{im}, b_{im} = \frac{\omega_{max}}{m!(\tau_{1,m-1})^{m-1}} \tag{8.11}$$

To comprehend the working of PHAF, consider a multi-component signal with cubic phases i.e. $M = 3$,

$$\Gamma(y) = A_1 \exp[j(a_0 + a_1 y + a_2 y^2 + a_3 y^3)]$$
$$+ A_2 \exp[j(b_0 + b_1 y + b_2 y^2 + b_3 y^3)] \quad \forall y \in [1, N], N = 256 \tag{8.12}$$

where the coefficients are $[a_3, a_2, a_1, a_0] = $ [-0.00002, 0.008, 0.5, 0] for the first component and $[b_3, b_2, b_1, b_0] = $ [0.00001, -0.006, -0.5, 0] for the second component. For the mth order PHAF, the optimal lag parameter $\tau_{k,m-1} \approx N/m$ [146] and hence, we used the integer values of $[\tau_{1,2}, \tau_{2,2}, \tau_{3,2}] = [N/3, N/3 - 10, N/3 + 10]$ for $K = 3$, $m = 3$ and $[\tau_{1,1}, \tau_{2,1}] = [N/2 - 10, N/2 + 10]$ for $K = 2$, $m = 2$ in the analysis.
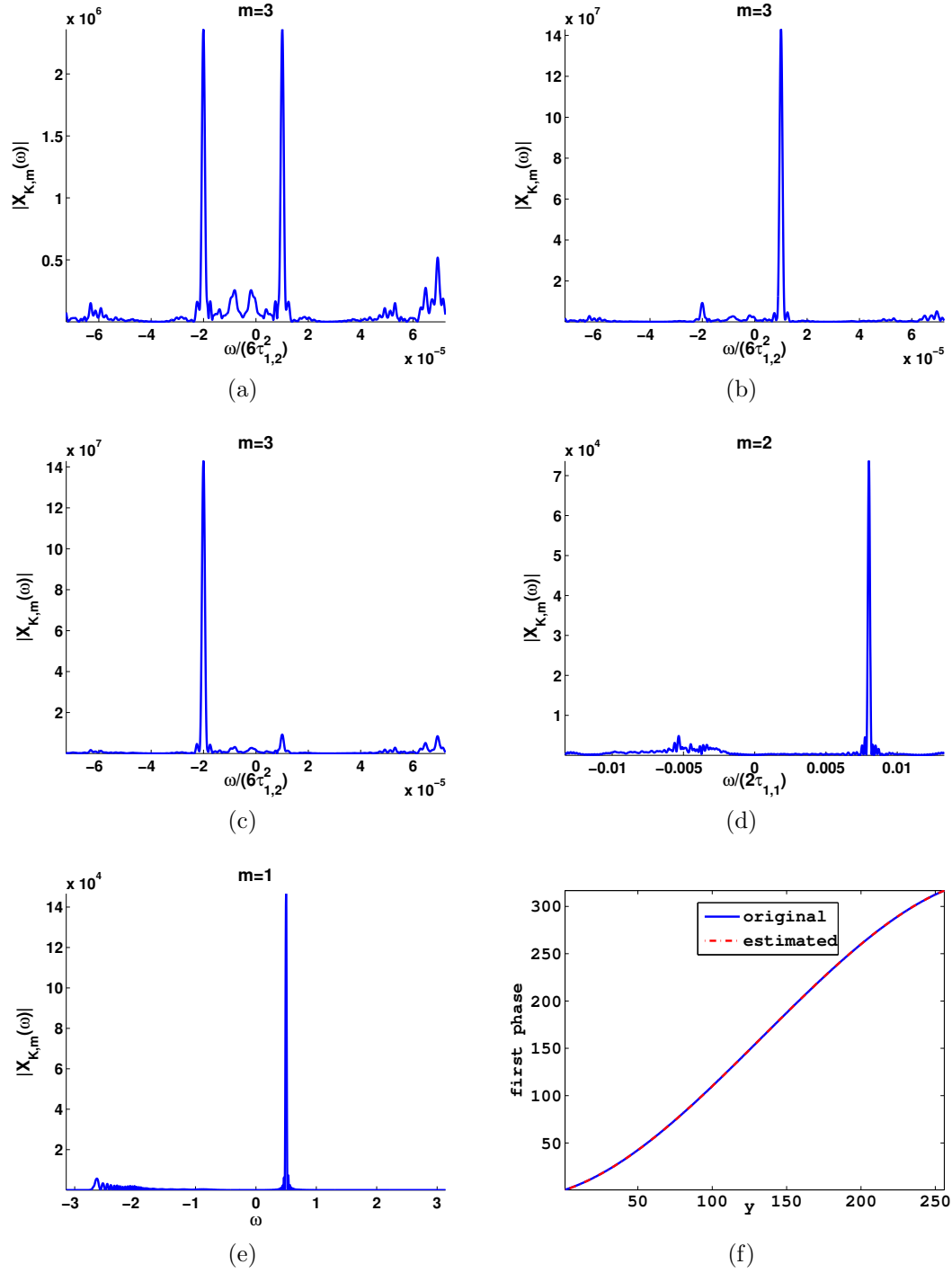
Fig. 8.1. (a) Third order ($m = 3$) PHAF spectrum for (a) $A_1 = A_2$, (b) $A_1 < A_2$ and (c) $A_1 > A_2$. (d) Second order ($m = 2$) PHAF spectrum. (e) First order ($m = 1$) PHAF spectrum. (f) Original vs estimated first phase in radians.

To obtain the highest order coefficients i.e. a_3 and b_3, the third order ($m = 3$) PHAF is computed and its spectrum $|X_{K,m}(\omega)|$ is shown in Fig.8.1(a) for the case of equal amplitudes i.e. $A_1 = A_2$. As the mth order polynomial coefficient is related to the frequency through Eq.(8.11), all PHAF plots in the chapter are shown on a frequency scaled axis, i.e. $\omega/(m!\tau_{1,m-1}^{m-1})$ instead of ω so that the coefficients a_m and b_m directly correspond to the peaks in the PHAF spectrum. From Fig.8.1(a), it is clear that two distinct peaks are visible corresponding to $\omega/(6\tau_{1,2}^2) = $ -0.00002 and 0.00001 i.e. the third order coefficients.

However, for the equal amplitude case, the main difficulty lies in matching the estimated coefficients with their respective components i.e. deciding whether the peak corresponds to a_3 or b_3. To resolve this, unequal amplitudes could be used so that the PHAF peak corresponding to the stronger component is dominant. This is shown in Fig.8.1(b) and Fig.8.1(c) for the cases $A_1 = 1, A_2 = 1.5$ and vice-versa. Consequently, m^{th} order PHAF peak detection would yield the mth order polynomial coefficient for the stronger component.

For the case $A_1 = 1.5, A_2 = 1$ i.e. $A_1 > A_2$, tracing the peak of the third order ($m = 3$) PHAF spectrum as shown in Fig.8.1(c) provides the estimate $\hat{a}_3$ for the stronger component. Subsequently, to obtain the second order coefficient a_2, a peeling operation is carried out to decrement the polynomial order of the stronger component,

$$\begin{aligned}
\Gamma_2(y) &= \Gamma(y)\exp[-j\hat{a}_3y^3] \\
&\approx A_1\exp[j(a_0 + a_1y + a_2y^2)] + A_2\exp[j(b_0 + b_1y + b_2y^2 + (b_3 - \hat{a}_3)y^3)]
\end{aligned}$$
(8.13)

The stronger component in $\Gamma_2(y)$ is reduced to a second order polynomial. Consequently, peak detection of the second order ($m = 2$) PHAF yields the estimate of a_2. The corresponding PHAF spectrum for $\Gamma_2(y)$ is shown in Fig.8.1(d) where the peak corresponds to $\hat{a}_2$. Subsequently, to estimate the first order coefficient a_1, an additional peeling operation is carried out,

$$\begin{aligned}
\Gamma_1(y) &= \Gamma_2(y)\exp[-j\hat{a}_2y^2] \\
&\approx A_1\exp[j(a_0 + a_1y)] + A_2\exp[j(b_0 + b_1y + (b_2 - \hat{a}_2)y^2 + (b_3 - \hat{a}_3)y^3)]
\end{aligned}$$ (8.14)

Since the stronger component in $\Gamma_1(y)$ is now a first order polynomial, the peak of the first order ($m = 1$) PHAF provides estimate of a_1. The corresponding PHAF spectrum for $\Gamma_1(y)$ is shown in Fig.8.1(e) where the peak corresponds to $\hat{a}_1$. Finally, the contribution of first order coefficient is removed from $\Gamma_1(y)$ to obtain,

$$\begin{aligned}
\Gamma_0(y) &= \Gamma_1(y)\exp[-j\hat{a}_1y] \\
&\approx A_1\exp[ja_0] + A_2\exp[j(b_0 + (b_1 - \hat{a}_1)y + (b_2 - \hat{a}_2)y^2 + (b_3 - \hat{a}_3)y^3)]
\end{aligned}$$ (8.15)

The term $A_1\exp[ja_0]$ in the above equation is a constant and does not vary with y. It can be separated by taking the mean of $\Gamma_0(y)$ and hence the zeroth order coefficient a_0

and the amplitude A_1 can be approximately estimated as,

$$\hat{a}_0 = \text{angle}\left[\frac{1}{N}\sum_{y=1}^{N}\Gamma_0(y)\right] \tag{8.16}$$

$$\hat{A}_1 = \left|\frac{1}{N}\sum_{y=1}^{N}\Gamma_0(y)\right| \tag{8.17}$$

The above procedure estimates the first or stronger component's polynomial coefficients iteratively from the highest order to the lowest. The estimates are $[\hat{a}_3, \hat{a}_2, \hat{a}_1, \hat{a}_0, \hat{A}_1] = [-0.00002, 0.008, 0.5001, -0.0650, 1.4956]$. Effectively, all the parameters i.e. the polynomial coefficients and the amplitude of the first component are now known. Subsequently, the contribution of the first component is removed from $\Gamma(y)$ to obtain the second component,

$$\begin{aligned}\Gamma'(y) &= \Gamma(y) - \hat{A}_1 \exp[j(\hat{a}_0 + \hat{a}_1 y + \hat{a}_2 y^2 + \hat{a}_3 y^3)] \\ &\approx A_2 \exp[j(b_0 + b_1 y + b_2 y^2 + b_3 y^3)]\end{aligned} \tag{8.18}$$

$\Gamma'(y)$ behaves as a third order polynomial phase signal. Accordingly, its third order PHAF spectrum, as shown in Fig.8.2(a), exhibits a dominant peak at $\omega/(6\tau_{1,2}^2) = 0.00001$ which corresponds to the third order coefficient b_3. The remaining coefficients for $\Gamma'(y)$ are obtained in the same way as for the stronger component using successive polynomial order reduction by peeling and corresponding PHAF peak detection. The PHAF spectra for $m = 2$ and $m = 1$ are shown in Fig.8.2(b) and Fig.8.2(c). The estimated coefficients for the second component are $[\hat{b}_3, \hat{b}_2, \hat{b}_1, \hat{b}_0] = [0.00001, -0.0060, -0.5001, -0.0562]$.

The phases for the first and second components are constructed from the polynomial coefficients as in Eq.(8.2) and Eq.(8.3). The original vs estimated first phase in radians is shown in Fig.8.1(f). Similarly, the original vs estimated second phase in radians is shown in Fig.8.2(d). The corresponding estimation errors in radians for the first and second phases are shown in Fig.8.2(e) Fig.8.2(f).

The above procedure, though shown for a third order multi-component signal, can be easily generalized for other polynomial orders. For the Mth order multi-component signal $\Gamma_i(y)$ of Eq.(8.4), the two sets of polynomial coefficients i.e. $[a_{i0}, \cdots, a_{iM}]$ and $[b_{i0}, \cdots, b_{iM}]$ in the ith segment are computed using the PHAF based estimation scheme discussed above. To minimize the errors due to noise and cross-component influence, these coefficient estimates are further refined using a multi-component optimization routine based on Nelder-Mead simplex algorithm [147]. Using these coefficients, the multiple phases are constructed for the ith segment using Eq.(8.2) and Eq.(8.3) and the corresponding phase derivatives are estimated using Eq.(8.5) and Eq.(8.6). Though the estimates obtained along a column are unwrapped, a phase-stitching procedure [148] between adjacent columns is used to obtain continuous phase distributions.
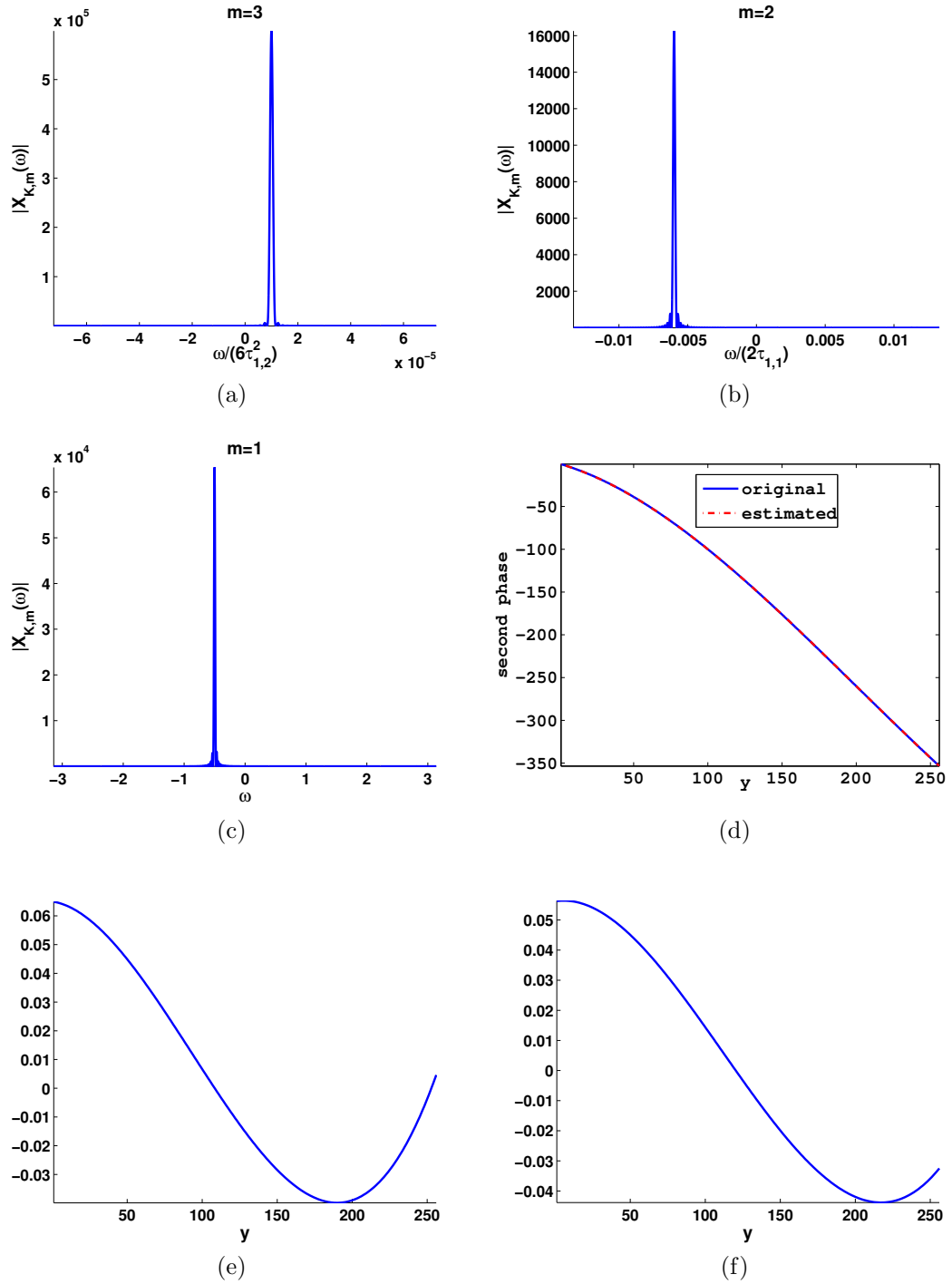
Fig. 8.2. (a) Third order ($m = 3$) PHAF spectrum. (b) Second order ($m = 2$) PHAF spectrum. (c) First order ($m = 1$) PHAF spectrum. (d) Original vs estimated second phase in radians. (e) Estimation error in radians for first phase. (f) Estimation error in radians for second phase.

It needs to be emphasized that the amplitude based separability criterion ensures proper matching of the estimated coefficients to the respective components in each segment. From an experimental perspective, the amplitude inequality between the two components could be achieved in DHI by controlling the relative intensities of the individual object beams.

Finally, the proposed method to retrieve multiple phase distributions can be summarized as

1. Each column of the reconstructed interference field $\Gamma(x, y)$ is divided into N_w segments to obtain $\Gamma_i(y)$.

2. In each segment, $\Gamma_i(y)$ is modeled as a multi-component polynomial phase signal as in Eq.(8.4).

3. The coefficients $[a_{i0}, \cdots, a_{iM}]$ of the stronger component are estimated by successive application of the PHAF peak detection and subsequent peeling operation as shown in Eq.(8.11-8.17).

4. The second component is obtained by removing the contribution of the first component from $\Gamma_i(y)$ using Eq.(8.18).

5. The coefficients $[b_{i0}, \cdots, b_{iM}]$ of the second component are estimated in a similar manner as step 3.

6. The phases $\phi_{1i}(y)$ and $\phi_{2i}(y)$ for the ith segment are obtained using Eq.(8.2) and Eq.(8.3) from the refined coefficients. Similarly, the phase derivatives are obtained using Eq.(8.5) and Eq.(8.6).

7. The above steps are repeated for all segments and subsequently for all columns to obtain the overall multiple phase distributions and their derivatives.

8.3 Simulation Analysis

To analyze the proposed method, a reconstructed interference field with multiple phases was simulated in MATLAB,

$$\Gamma(x, y) = A_1 \exp[j\phi_1(x, y)] + A_2 \exp[j\phi_2(x, y)] \tag{8.19}$$

with $A_1 = 2$ and $A_2 = 1$ i.e. amplitude ratio of 2:1. Noise was added at signal-to-noise ratio (SNR) of 20 dB using MATLAB's 'awgn' function. The real part of $\Gamma(x, y)$ which constitutes the moirè fringe pattern (256×256 pixels) is shown in Fig.8.3(a).

To highlight the problem of spectral overlap in the absence of a spatial carrier, the Fourier transform of $\Gamma(x, y)$ was calculated as,

$$\gamma(\omega_x, \omega_y) = \text{DFT}[\Gamma(x, y)] \tag{8.20}$$
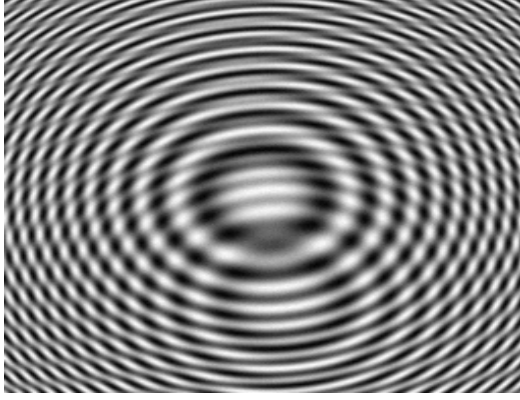
(a)
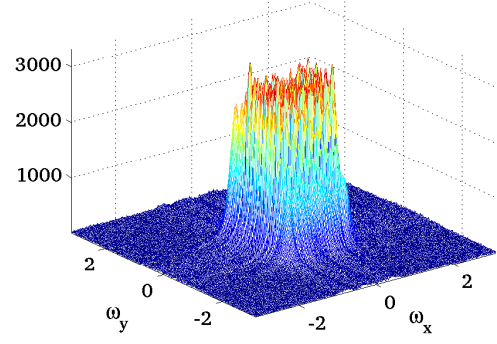
(b)
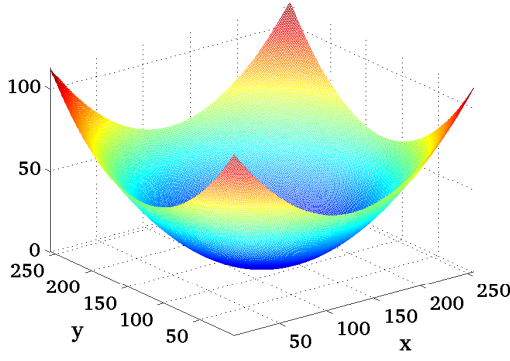
(c)
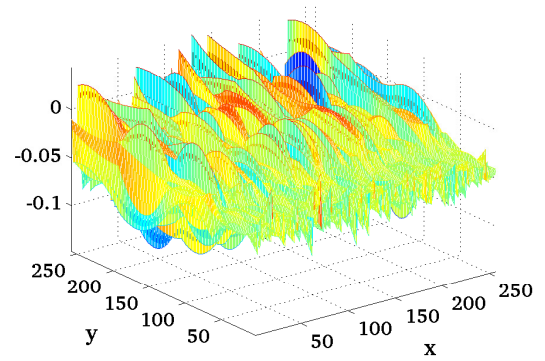
(d)
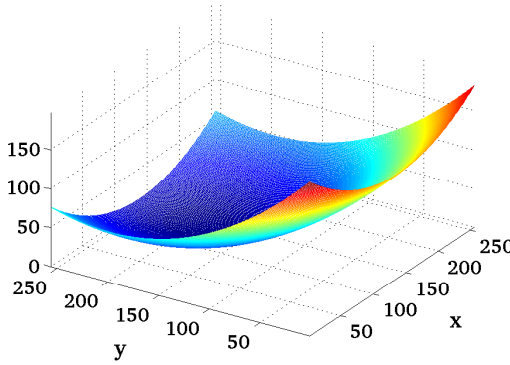
(e)
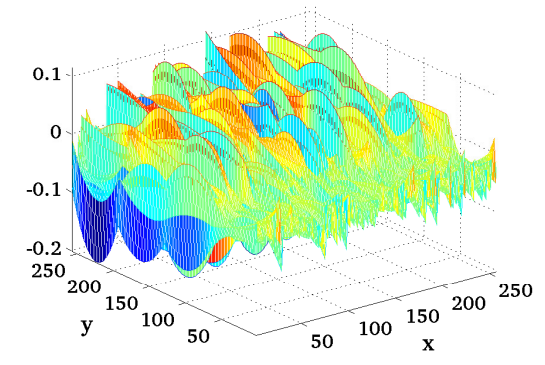
(f)

Fig. 8.3. (a) Moiré fringe pattern. (b) Fourier spectrum $|\gamma(\omega_x, \omega_y)|$. (c) Estimated $\phi_1(x, y)$ in radians. (d) Estimation error for first phase in radians. (e) Estimated $\phi_2(x, y)$ in radians. (f) Estimation error for second phase in radians.

83

(a)

(b)

(c)

(d)
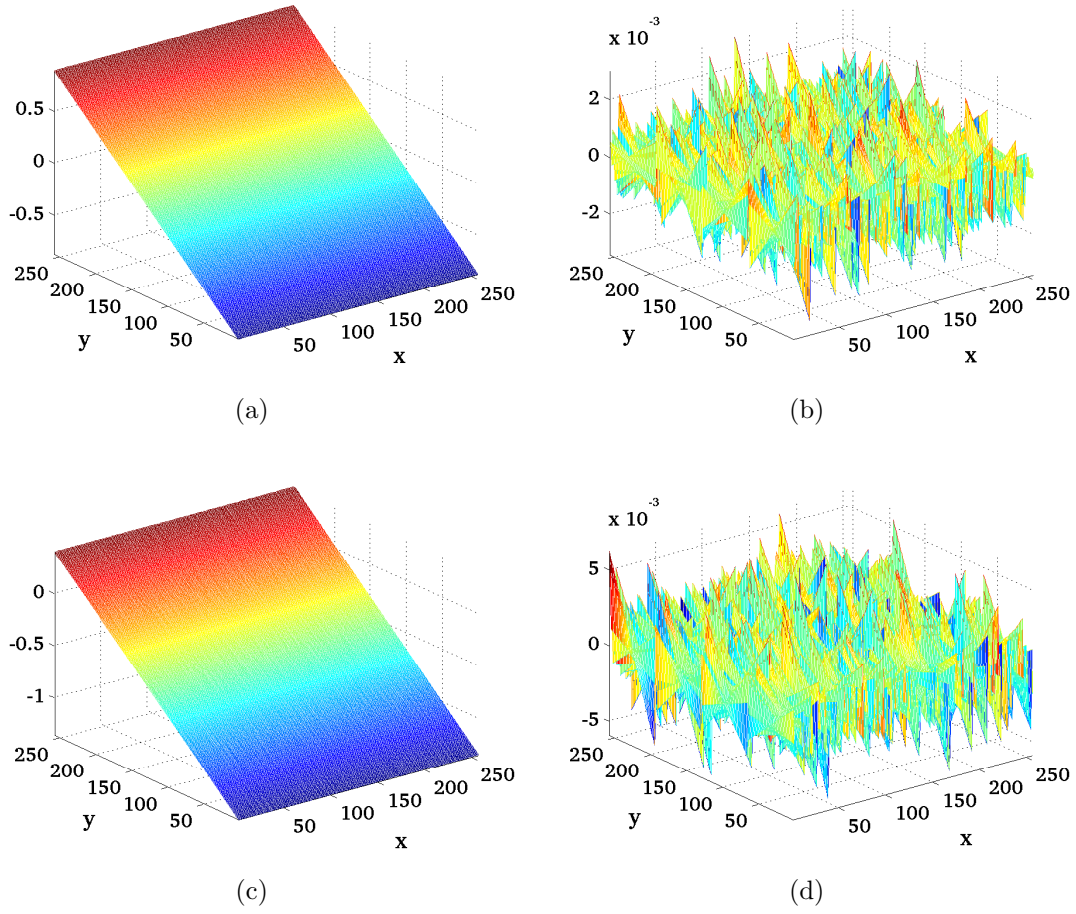
Fig. 8.4. (a) Estimated first phase derivative in radians/pixel. (b) Corresponding esti-
mation error in radians/pixel. (c) Estimated second phase derivative in radians/pixel.
(d) Corresponding estimation error in radians/pixel.

The Fourier spectrum i.e. $|\gamma(\omega_x, \omega_y)|$ is shown in Fig.8.3(b). From the figure, it is clear
that the spectra of the two components are overlapped and not well separated. Due to the
spectral overlap, the individual components with the phases $\phi_1(x, y)$ and $\phi_2(x, y)$ cannot
be efficiently filtered in the frequency domain using the Fourier transform. Hence, in the
absence of a spatial carrier, retrieval of multiple phases and their derivatives is difficult
using current fringe analysis methods.

To estimate the phases $\phi_1(x, y)$ and $\phi_2(x, y)$ and their derivatives from $\Gamma(x, y)$, the pro-
posed method was applied. For the analysis, we used $N_w = 4$ and $M = 2$. The esti-
mated first phase $\phi_1(x, y)$ and the corresponding estimation error in radians are shown
in Fig.8.3(c) and Fig.8.3(d). The estimated second phase $\phi_2(x, y)$ and the corresponding
estimation error in radians are shown in Fig.8.3(e) and Fig.8.3(f). Similarly, the estimated
first phase derivative $\partial\phi_1/\partial y$ and the corresponding estimation error in radians/pixel are
shown in Fig.8.4(a) and Fig.8.4(b). The estimated second phase derivative $\partial\phi_2/\partial y$ and

the corresponding estimation error in radians/pixel are shown in Fig.8.4(c) and Fig.8.4(d). The RMSEs for the estimation of the phases $\phi_1(x, y)$ and $\phi_2(x, y)$ were 0.0479 and 0.0595 radians. The RMSEs for the estimation of the phase derivatives $\partial\phi_1/\partial y$ and $\partial\phi_2/\partial y$ were 0.0006 and 0.0012 radians/pixel. From the analysis, it is clear that the proposed method is capable of reliable estimation of multiple phases and their derivatives from a single fringe pattern.

8.4 Summary

This chapter introduced a piecewise multi-component polynomial phase approximation based method for direct retrieval of multiple phases and their derivatives, which is highly desired for the simultaneous in-plane and out-of-plane deformation measurements in DHI. The major advantage of the proposed method lies in its ability to extract information about multiple components from a single fringe pattern without the need of spatial carrier and spectral filtering, which is a significant advancement compared to the current state-of-the-art spatial fringe analysis methods. In addition, the method provides continuous phase distributions and does not require complex unwrapping algorithms. The proposed method has potential to significantly enhance the applicability of DHI for simultaneous multi-dimensional measurements.

Chapter 9

Conclusions

The thesis explored some novel techniques for the estimation of phase gradients or derivatives in fringe analysis. The developed techniques alleviate the limitations imposed by the current state-of-the-art methods for measuring single or multiple phase derivatives from a fringe pattern. The unique advantages such as high estimation accuracy, computational efficiency, robustness against noise and non-requirement of multiple fringe patterns, filtering and unwrapping operations highlight the suitability and utility of these techniques for fringe analysis.

The pseudo Wigner-Ville distribution method introduced in chapter 2 provides an elegant approach for estimating phase derivatives from fringe patterns obtained in digital holographic interferometry. Compared to the other popular phase derivative estimation techniques, the PSWVD method exhibits better accuracy and less computational burden. To further improve the applicability of the PSWVD method, an adaptive windowing approach based on intersection of confidence intervals algorithm was proposed in chapter 3. By adaptively selecting the optimum window length, the approach significantly extends the effectiveness of the PSWVD method to estimate phase derivatives with rapid variations.

Chapter 4 proposed the two-dimensional PSWVD to handle fringe patterns with severe noise. The presence of a 2D window enhances the robustness of the method against noise and also allows the simultaneous estimation of the phase derivatives with respect to both the horizontal and vertical spatial coordinates. These advantages enhance the utility of the method in digital holographic interferometry for many practical and industrial applications.

The above developed techniques allow direct estimation of the first order phase derivative only, whereas, higher order derivatives of phase are also strongly desired for many applications in non-destructive testing and experimental mechanics. To address this problem, a complex-lag distribution based method was proposed in chapter 5. The method provides a generalized approach for estimating phase derivatives of arbitrary order in digital

holographic interferometry.

Chapter 6 outlined some applications of the developed phase derivative estimation techniques. The pseudo Wigner-Ville distribution based method was applied for locating defects in a fringe pattern. The feasibility of detecting faults and defects provided by the proposed method is of great significance in applications such as quality assessment and reliability testing. Similarly, the PSWVD method was applied in a fringe projection setup for analyzing the temporal evolution of surface slopes of a deformed object subjected to dynamic loading. The high computational efficiency of the method enhances its potential for studying transient phenomena. Finally, a dual-wavelength configuration was proposed in digital holographic interferometry for the simultaneous measurement of in-plane and out-of-plane displacement derivatives in a deformed object.

Chapter 7 introduced the concept of digital holographic moiré for simultaneous multi-dimensional deformation analysis. In this approach, the information about the in-plane and out-of-plane displacements is encoded in the form of multiple phases of a moiré fringe pattern. Thus, the problem of multi-dimensional measurements in digital holographic interferometry is reduced to estimating the multiple phases and their derivatives from moiré fringes. Compared to the other popular techniques, the proposed method does not require multiple reference beams and CCD cameras and is capable of simultaneous multi-dimensional measurements from a single fringe pattern.

Chapter 8 presented the multi-component polynomial phase formulation for demodulating moiré fringes in digital holographic interferometry. The proposed method enables estimation of multiple phases and their derivatives from a single fringe pattern without the need of an external spatial carrier, filtering and unwrapping operations which is hitherto not possible with the current state-of-the-art fringe analysis methods.

For future work, the applicability of the proposed techniques could be investigated for other interferometric techniques such as digital speckle pattern interferometry. Further, the feasibility of using graphics processing units (GPU) for improving the computational performance of the proposed techniques needs to be analyzed. This could have significant impact on the use of these techniques for real-time applications. Finally, the area of multi-component fringe analysis presents challenging and exciting opportunities with immense application potential and should be further explored.

Bibliography

[1] T. Kreis, *Handbook of Holographic Interferometry: Optical and Digital Methods* (Wiley-VCH, 2005).

[2] P. K. Rastogi, ed., *Digital Speckle Pattern Interferometry and Related Techniques* (John Wiley, Chichester, 2000).

[3] S. S. Gorthi and P. Rastogi, "Fringe projection techniques: Whither we are ?" Opt. Laser Eng. **48**, 133–140 (2010).

[4] K. Creath, "Phase-measurement interferometry," Progress in Optics, E. Wolf, ed. (North-Holland, Amsterdam), **Vol.5**, 349–393 (1988).

[5] P. Carré, "Installation et utilisation du comparateur photoélectrique et interférentiel du bureau international des poids et mesures," Metrologia **2**, 13–23 (1966).

[6] J. H. Bruning, D. R. Herriott, J. E. Gallagher, D. P. Rosenfeld, A. D. White, and D. J. Brangaccio, "Digital wavefront measuring interferometer for testing optical surfaces and lenses," Appl. Opt. **13**, 2693–2703 (1974).

[7] J. Greivenkamp and J. H. Bruning, *"Phase Shifting Interferometers" in Optical Shop Testing, D. Malacara, ed.* (Wiley,New York, 1992).

[8] C. J. Morgan, "Least-squares estimation in phase-measurement interferometry," Opt. Lett. **7**, 368–370 (1982).

[9] Y. Surrel, "Design of algorithms for phase measurements by the use of phase stepping," Appl. Opt. **35**, 51–60 (1996).

[10] M. Miranda, B. V. Dorrío, J. Blanco, J. Diz-Bugarín, and F. Ribas, "Characteristic polynomial theory of two-stage phase shifting algorithms," Opt. Laser Eng. **50**, 522–528 (2012).

[11] K. G. Larkin and B. F. Oreb, "Design and assessment of symmetrical phase-shifting algorithms," J. Opt. Soc. Am. A **9**, 1740–1748 (1992).

[12] P. Hariharan, "Phase-shifting interferometry: Minimization of systematic errors," Opt. Eng. **39**, 967–969 (2000).

[13] J. Schwider, R. Burow, K. E. Elssner, J. Grzanna, R. Spolaczyk, and K. Merkel, "Digital wave-front measuring interferometry: some systematic error sources," Appl. Opt. **22**, 3421–3432 (1983).

[14] P. Hariharan, B. F. Oreb, and T. Eiju, "Digital phase-shifting interferometry: a simple error-compensating phase calculation algorithm," Appl. Opt. **26**, 2504–2506 (1987).

[15] J. van Wingerden, H. J. Frankena, and C. Smorenburg, "Linear approximation for measurement errors in phase shifting interferometry," Appl. Opt. **30**, 2718–2729 (1991).

[16] Y. Surrel, "Phase stepping: a new self-calibrating algorithm," Appl. Opt. **32**, 3598–3600 (1993).

[17] C. Joenathan, "Phase-measuring interferometry: new methods and error analysis," Appl. Opt. **33**, 4147–4155 (1994).

[18] J. Schmit and K. Creath, "Extended averaging technique for derivation of error-compensating algorithms in phase-shifting interferometry," Appl. Opt. **34**, 3610–3619 (1995).

[19] K. Hibino, B. F. Oreb, D. I. Farrant, and K. G. Larkin, "Phase shifting for nonsinusoidal waveforms with phase-shift errors," J. Opt. Soc. Am. A **12**, 761–768 (1995).

[20] P. de Groot, "Derivation of algorithms for phase-shifting interferometry using the concept of a data-sampling window," Appl. Opt. **34**, 4723–4730 (1995).

[21] K. Hibino, B. F. Oreb, D. I. Farrant, and K. G. Larkin, "Phase-shifting algorithms for nonlinear and spatially nonuniform phase shifts," J. Opt. Soc. Am. A **14**, 918–930 (1997).

[22] J. Schwider, T. Dresel, and B. Manzke, "Some considerations of reduction of reference phase error in phase-stepping interferometry," Appl. Opt. **38**, 655–659 (1999).

[23] B. Pan, Q. Kemao, L. Huang, and A. Asundi, "Phase error analysis and compensation for nonsinusoidal waveforms in phase-shifting digital fringe projection profilometry," Opt. Lett. **34**, 416–418 (2009).

[24] M. Takeda, H. Ina, and S. Kobayashi, "Fourier-transform method of fringe-pattern analysis for computer-based topography and interferometry," J. Opt. Soc. Am. **72**, 156–160 (1982).

[25] J. Zhong and J. Weng, "Dilating gabor transform for the fringe analysis of 3-d shape measurement," Opt. Eng. **43**, 895–899 (2004).

[26] M. Afifi, A. Fassi-Fihri, M. Marjane, K. Nassim, M. Sidki, and S. Rachafi, "Paul wavelet-based algorithm for optical phase distribution evaluation," Opt. Commun. **211**, 47–51 (2002).

[27] Q. Kemao, "Windowed fourier transform for fringe pattern analysis," Appl. Opt. **43**, 2695–2702 (2004).

[28] S. Ozder, O. Kocahan, E. Coskun, and H. Goktas, "Optical phase distribution evaluation by using an s-transform," Opt. Lett. **32**, 591–593 (2007).

[29] D. C. Ghiglia and M. D. Pritt, *Two-Dimensional Phase Unwrapping: Theory, Algorithms, and Software* (Wiley-Interscience, 1998).

[30] R. Cusack, J. M. Huntley, and H. T. Goldrein, "Improved noise-immune phase-unwrapping algorithm," Appl. Opt. **34**, 781–789 (1995).

[31] D. C. Ghiglia and L. A. Romero, "Robust two-dimensional weighted and unweighted phase unwrapping that uses fast transforms and iterative methods," J. Opt. Soc. Am. A **11**, 107–117 (1994).

[32] J. R. Buckland, J. M. Huntley, and S. R. E. Turner, "Unwrapping noisy phase maps by use of a minimum-cost-matching algorithm," Appl. Opt. **34**, 5100–5108 (1995).

[33] A. Asundi and Z. Wensen, "Fast phase-unwrapping algorithm based on a gray-scale mask and flood fill," Appl. Opt. **37**, 5416–5420 (1998).

[34] B. Gutmann and H. Weber, "Phase unwrapping with the branch-cut method: Role of phase-field direction," Appl. Opt. **39**, 4802–4816 (2000).

[35] R. M. Goldstein, H. A. Zebker, and C. L. Werner, "Satellite radar interferometry: two-dimensional phase unwrapping," Radio Sci. **23**, 713–720 (1988).

[36] J. M. B. Dias and J. M. N. Leitao, "The zpim algorithm: A method for interferometric image reconstruction in sar/sas," IEEE Trans. Image Proc. **11**, 408–422 (2002).

[37] J. Strand and T. Taxt, "Two-dimensional phase unwrapping using robust derivative estimation and adaptive integration," IEEE Trans. Image Proc. **11**, 1192–1200 (2002).

[38] A. Baldi, "Phase unwrapping by region growing," Appl. Opt. **42**, 2498–2505 (2003).

[39] J. Meneses, T. Gharbi, and P. Humbert, "Phase-unwrapping algorithm for images with high noise content based on a local histogram," Appl. Opt. **44**, 1207–1215 (2005).

[40] M. J. Huang and Z. N. He, "Phase unwrapping through region-referenced algorithm and window-patching method," Opt. Commun. **203**, 225–241 (2002).

[41] Z. Huang, A. J. Shih, and J. Ni, "Phase unwrapping for large depth-of-field 3d laser holographic interferometry measurement of laterally discontinuous surfaces," Meas. Sci. Tech. **17**, 3110–3119 (2006).

[42] S. Zhang, X. Li, and S. Yau, "Multilevel quality-guided phase unwrapping algorithm for real-time three-dimensional shape reconstruction," Appl. Opt. **46**, 50–57 (2007).

[43] B. Jose, V. Katkovnik, J. Astola, and K. Egiazarian, "Absolute phase estimation: adaptive local denoising and global unwrapping," Appl. Opt. **47**, 5358–5369 (2008).

[44] V. Katkovnik, J. Astola, and K. Egiazarian, "Phase local approximation (phasela) technique for phase unwrap from noisy data," IEEE Trans. Image Proc. **17**, 833–846 (2008).

[45] Y. Y. Hung and C. Y. Liang, "Image-shearing camera for direct measurement of surface strains," Appl. Opt. **18**, 1046–1051 (1979).

[46] P. K. Rastogi, "Measurement of curvature and twist of a deformed object by electronic speckle-shearing pattern interferometry," Opt. Lett. **21**, 905–907 (1996).

[47] W. Steinchen, L. Yang, M. Schuth, and G. Kupfer, "Application of shearography to quality assurance," Journal of Materials Processing Technology **52**, 141 – 150 (1995).

[48] M. Hung, K. Long, and J. Wang, "Measurement of residual stress by phase shift shearography," Opt. Laser Eng. **27**, 61 – 73 (1997).

[49] K. Qian, H. S. Seah, and A. Asundi, "Fault detection by interferometric fringe pattern analysis using windowed fourier transform," Meas. Sci. Tech. **16**, 1582–1587 (2005).

[50] Y. Y. Hung and D. Shi, "Technique for rapid inspection of hermetic seals of microelectronic packages using shearography," Opt. Eng. **37**, 1406 (1998).

[51] Y.Y. and Hung, "Shearography for non-destructive evaluation of composite structures," Opt. Laser Eng. **24**, 161 – 182 (1996).

[52] P. Zaslansky, J. D. Currey, A. A. Friesem, and S. Weiner, "Phase shifting speckle interferometry for determination of strain and young's modulus of mineralized biological materials: A study of tooth dentin compression in water," J. Biomed. Opt. **10**, 1–13 (2005).

[53] J. R. Tyrer, C. Heras-Palou, and T. Slater, "Three-dimensional human femoral strain analysis using espi," Opt. Laser Eng. **23**, 291–303 (1995).

[54] L. Yang, P. Zhang, S. Liu, P. R. Samala, M. Su, and H. Yokota, "Measurement of strain distributions in mouse femora with 3d-digital speckle pattern interferometry," Opt. Laser Eng. **45**, 843–851 (2007).

[55] S. J. Kirkpatrick and M. J. Cipolla, "High resolution imaged laser speckle strain gauge for vascular applications," J. Biomed. Opt. **5**, 62–71 (2000).

[56] P. K. Rastogi, "An electronic pattern speckle shearing interferometer for the measurement of surface slope variations of three-dimensional objects," Opt. Laser Eng. **26**, 93–100 (1997).

[57] R. Oven, "Measurement of two dimensional refractive index profiles of channel waveguides using an interferometric technique," Appl. Opt. **48**, 5704–5712 (2009).

[58] G. H. Kaufmann and G. E. Galizzi, "Evaluation of a method to determine interferometric phase derivatives," Opt. Laser Eng. **27**, 451–465 (1997).

[59] Y. Y. Hung, "A speckle-shearing interferometer: A tool for measuring derivatives of surface displacements," Opt. Commun. **11**, 132–135 (1974).

[60] Y. Y. Hung, "Shearography: A new optical method for strain measurement and nondestructive testing." Opt. Eng. **21**, 391–395 (1982).

[61] C. J. Tay, S. L. Toh, H. M. Shang, and Q. Y. Lin, "Direct determination of second-order derivatives in plate bending using multiple-exposure shearography," Opt. Laser Tech. **26**, 91–98 (1994).

[62] F. S. Chau and J. Zhou, "Direct measurement of curvature and twist of plates using digital shearography," Opt. Laser Eng. **39**, 431–440 (2003).

[63] F. Labbe, R. R. Cordero, A. Martínez, and R. Rodríguez-Vera, "Measuring displacement derivatives by electronic speckle pattern shearing interferometry (espsi)," Meas. Sci. Tech. **16**, 1677–1683 (2005).

[64] J. Politch and S. Gryc, "Second derivative of displacement on cylindrical shells by projection moire," Appl. Opt. **28**, 111–118 (1989).

[65] S. K. Bhadra, S. K. Sarkar, R. N. Chakraborty, and A. Basuray, "Coherent moire technique for obtaining slope and curvature of stress patterns," Opt. Eng. **33**, 3359–3363 (1994).

[66] G. Subramanian and A. Subramanian, "Curvature contours of flexed plates by a multiple illumination moire shearing interferometer," Strain **32**, 59–62 (1996).

[67] B. Chen and C. Basaran, "Automatic full strain field moire interferometry measurement with nano-scale resolution," Exp. Mech. **48**, 665–673 (2008).

[68] D. K. Sharma, R. S. Sirohi, and M. P. Kothiyal, "Simultaneous measurement of slope and curvature with a three-aperture speckle shearing interferometer," Appl. Opt. **23**, 1542–1546 (1984).

[69] K. F. Wang, A. K. Tieu, and M. H. Gao, "Measurement of curvature distribution using digital speckle three-shearing aperture interferometry," Opt. Laser Tech. **39**, 926–928 (2007).

[70] B. Bhaduri, M. P. Kothiyal, and N. Krishna Mohan, "Curvature measurement using three-aperture digital shearography and fast fourier transform," Opt. Laser Eng. **45**, 1001–1004 (2007).

[71] H. Singh and J. S. Sirkis, "Direct extraction of phase gradients from fourier-transform and phase-step fringe patterns," Appl. Opt. **33**, 5016–5020 (1994).

[72] M. Facchini and P. Zanetta, "Derivatives of displacement obtained by direct manipulation of phase-shifted interferograms," Appl. Opt. **34**, 7202–7206 (1995).

[73] K. Qian, S. H. Soon, and A. Asundi, "Phase-shifting windowed fourier ridges for determination of phase derivatives," Opt. Lett. **28**, 1657–1659 (2003).

[74] G. K. Bhat, "A fourier transform technique to obtain phase derivatives in interferometry," Opt. Commun. **110**, 279–286 (1994).

[75] S. Mallat, *A Wavelet Tour of Signal Processing, Third Edition: The Sparse Way* (Academic Press, 2008).

[76] C. A. Sciammarella and T. Kim, "Frequency modulation interpretation of fringes and computation of strains," Exp. Mech. **45**, 393–403 (2005).

[77] C. A. Sciammarella and T. Kim, "Determination of strains from fringe patterns using space-frequency representations," Opt. Eng. **42**, 3182–3193 (2003).

[78] L. R. Watkins, S. M. Tan, and T. H. Barnes, "Determination of interferometer phase distributions by use of wavelets," Opt. Lett. **24**, 905–907 (1999).

[79] Q. Kemao, S. H. Soon, and A. Asundi, "Instantaneous frequency and its application to strain extraction in moire interferometry," Appl. Opt. **42**, 6504–6513 (2003).

[80] M. A. Gdeisat, A. Abid, D. R. Burton, M. J. Lalor, F. Lilley, C. Moore, and M. Qudeisat, "Spatial and temporal carrier fringe pattern demodulation using the one-dimensional continuous wavelet transform: Recent progress, challenges, and suggested developments," Opt. Laser Eng. **47**, 1348–1361 (2009).

[81] A. Federico and G. H. Kaufmann, "Phase retrieval in digital speckle pattern interferometry by use of a smoothed space-frequency distribution," Appl. Opt. **42**, 7066–7071 (2003).

[82] Q. Kemao, "Two-dimensional windowed fourier transform for fringe pattern analysis: Principles, applications and implementations," Opt. Laser Eng. **45**, 304–317 (2007).

[83] U. Schnars and W. P. O. Juptner, "Digital recording and numerical reconstruction of holograms," Meas. Sci. Tech. **13**, R85–R101 (2002).

[84] Y. Zou, G. Pedrini, and H. Tiziani, "Derivatives obtained directly from displacement data," Opt. Commun. **111**, 427–432 (1994).

[85] U. Schnars and W. P. O. Juptner, "Digital recording and reconstruction of holograms in hologram interferometry and shearography," Appl. Opt. **33**, 4373–4377 (1994).

[86] C. Liu, "Simultaneous measurement of displacement and its spatial derivatives with a digital holographic method," Opt. Eng. **42**, 3443–3446 (2003).

[87] C. Quan, C. J. Tay, and W. Chen, "Determination of displacement derivative in digital holographic interferometry," Opt. Commun. **282**, 809–815 (2009).

[88] W. Chen, C. Quan, and C. J. Tay, "Measurement of curvature and twist of a deformed object using digital holography," Appl. Opt. **47**, 2874–2881 (2008).

[89] G. Pedrini and H. J. Tiziani, "Digital double-pulse holographic interferometry using fresnel and image plane holograms," Measurement **15**, 251–260 (1995).

[90] E. Kolenovic, W. Osten, R. Klattenhoff, S. Lai, C. von Kopylow, and W. Juptner, "Miniaturized digital holography sensor for distal three-dimensional endoscopy," Appl. Opt. **42**, 5167–5172 (2003).

[91] S. Okazawa, M. Fujigaki, Y. Morimoto, and T. Matui, "Simultaneous measurement of out-of-plane and in-plane displacements by phase-shifting digital holographic interferometry," Applied Mechanics and Materials **3-4**, 223–228 (2005).

[92] Y. Morimoto, T. Matui, M. Fujigaki, and A. Matsui, "Three-dimensional displacement analysis by windowed phase-shifting digital holographic interferometry," Strain **44**, 49–56 (2008).

[93] Y. Morimoto, T. Matui, and M. Fujigaki, "Application of three-dimensional displacement and strain distribution measurement by windowed phase-shifting digital holographic interferometry," Advanced Material Research **47-50**, 1262–1265 (2008).

[94] M. De La Torre-Ibarra, F. Mendoza-Santoyo, C. Perez-Lopez, and T. Saucedo-A, "Detection of surface strain by three-dimensional digital holography," Appl. Opt. **44**, 27–31 (2005).

[95] M. De la Torre-Ibarra, F. Mendoza Santoyo, C. Perez-Lopez, T. Saucedo Anaya, and D. D. Aguayo, "Surface strain distribution on thin metallic plates using 3-d digital holographic interferometry," Opt. Eng. **45** (2006).

[96] G. Pedrini and H. J. Tiziani, "Quantitative evaluation of two-dimensional dynamic deformations using digital holography," Opt. Laser Tech. **29**, 249–256 (1997).

[97] G. Pedrini, Y. L. Zou, and H. J. Tiziani, "Simultaneous quantitative evaluation of in-plane and out-of-plane deformations by use of a multidirectional spatial carrier," Appl. Opt. **36**, 786–792 (1997).

[98] S. Schedin, G. Pedrini, H. J. Tiziani, and F. Mendoza Santoyo, "Simultaneous three-dimensional dynamic deformation measurements with pulsed digital holography," Appl. Opt. **38**, 7056–7062 (1999).

[99] P. Picart, E. Moisson, and D. Mounier, "Twin-sensitivity measurement by spatial multiplexing of digitally recorded holograms," Appl. Opt. **42**, 1947–1957 (2003).

[100] C. Kohler, M. R. Viotti, and J. G. Armando Albertazzi, "Measurement of three-dimensional deformations using digital holography with radial sensitivity," Appl. Opt. **49**, 4004–4009 (2010).

[101] L. Cohen, *Time Frequency Analysis* (Prentice hall, 1995).

[102] Q. Kemao, "On window size selection in the windowed fourier ridges algorithm," Opt. Laser Eng. **45**, 1186–1192 (2007).

[103] J. A. Quiroga, J. Antonio Gomez-Pedrero, and A. Garcia-Botella, "Algorithm for fringe pattern normalization," Opt. Commun. **197**, 43–51 (2001).

[104] S. Lawrence Marple Jr., "Computing the discrete-time analytic signal via fft," IEEE Trans. Sig. Proc. **47**, 2600–2603 (1999).

[105] V. Katkovnik and L. Stankovic, "Instantaneous frequency estimation using the wigner distribution with varying and data-driven window length," IEEE Trans. Sig. Proc. **45**, 2147 (1997).

[106] S. C. Sekhar and T. V. Sreenivas, "Signal-to-noise ratio estimation using higher-order moments," Signal Processing **86**, 716–732 (2006).

[107] L. Debnath and B. Rao, "On new two-dimensional wigner-ville nonlinear integral transforms and their basic properties," Integr. Transf. Spec. F. **21**, 165–174 (2010).

[108] N. Pandey and B. Hennelly, "Fixed-point numercial-reconstruction for digital holographic microscopy," Opt. Lett. **35**, 1076–1078 (2010).

[109] L. Ahrenberg, A. J. Page, B. M. Hennelly, J. B. McDonald, and T. J. Naughton, "Using commodity graphics hardware for real-time digital hologram view-reconstruction," J. Disp. Tech. **5**, 111–119 (2009).

[110] C. Cornu, S. Stanković, C. Ioana, A. Quinquis, and L. Stanković, "Generalized representation of phase derivatives for regular signals," IEEE Trans. Sig. Proc. **55**, 4831–4838 (2007).

[111] W. Osten, W. P. Jueptner, and U. Mieth, "Knowledge-assisted evaluation of fringe patterns for automatic fault detection," Proc. SPIE **2004**, 256–268 (1994).

[112] D. A. Tichenor and V. P. Madsen, "Computer analysis of holographic interferograms for nondestructive testing," Opt. Eng. **18**, 469–72 (1979).

[113] D. W. Robinson, "Automatic fringe analysis with a computer image-processing system," Appl. Opt. **22**, 2169–2176 (1983).

[114] W. P. Juptner, T. M. Kreis, U. Mieth, and W. Osten, "Application of neural networks and knowledge-based systems for automatic identification of fault-indicating fringe patterns," Proc. SPIE **2342**, 16–26 (1994).

[115] S. Krüger, G. Wernicke, W. Osten, D. Kayser, N. Demoli, and H. Gruber, "Fault detection and feature analysis in interferometric fringe patterns by the application of wavelet filters in convolution processors," J. Elect. Imag. **10**, 228–233 (2001).

[116] F. Kallmeyer, S. Krueger, G. Wernicke, H. Gruber, N. Demoli, W. Osten, and D. Kayser, "Optical processing for the detection of faults in interferometric patterns," Proc. SPIE **4777**, 371–381 (2002).

[117] T. W. Yannick Caulier, Klaus Spinnler and S. Bourennane, "Specific features for the analysis of fringe images," Opt. Eng. **47**, 057201 (2008).

[118] A. Federico and G. H. Kaufmann, "Retrieval of phase derivative discontinuities in digital speckle pattern interferometry fringes using the wigner-ville distribution," Proc. SPIE **5531**, 127–133 (2004).

[119] X. Li, "Wavelet transform for detection of partial fringe patterns induced by defects in nondestructive testing of holographic interferometry and electronic speckle pattern interferometry," Opt. Eng. **39**, 2821–2827 (2000).

[120] D. Francis, S. W. James, and R. P. Tatam, "Surface strain measurement of rotating objects using pulsed laser shearography with coherent fibre-optic imaging bundles," Meas. Sci. Tech. **19**, 105301 (2008).

[121] Y. H. Huang, S. P. Ng, L. Liu, Y. S. Chen, and M. Y. Y. Hung, "Shearographic phase retrieval using one single specklegram: a clustering approach," Opt. Eng. **47**, 054301 (2008).

[122] Y. H. Huang, S. P. Ng, L. Liu, C. L. Li, Y. S. Chen, and Y. Y. Hung, "Ndt&e using shearography with impulsive thermal stressing and clustering phase extraction," Opt. Laser Eng. **47**, 774–781 (2009).

[123] F. Labbe, "Strain-rate measurements by electronic speckle-pattern interferometry (espi)," Opt. Laser Eng. **45**, 827–833 (2007).

[124] B. Guelorget, M. Francois, C. Vial-Edwards, G. Montay, L. Daniel, and J. Lu, "Strain rate measurement by electronic speckle pattern interferometry: A new look at the strain localization onset," Mat. Sci. Eng. A **415**, 234–241 (2006).

[125] T. Shiraishi, S. Toyooka, H. Kadono, T. Saito, and S. Ping, "Dynamic espi system for spatio-temporal strain analysis of a deforming solid object," Key Eng. Mat. **326-328**, 95–98 (2006).

[126] C. Quan, C. J. Tay, X. Y. He, X. Kang, and H. M. Shang, "Microscopic surface contouring by fringe projection method," Opt. Laser Tech. **34**, 547–552 (2002).

[127] G. S. Spagnolo and D. Ambrosini, "Diffractive optical element based sensor for roughness measurement," Sensors and Actuators A: Physical **100**, 180–186 (2002).

[128] P. S. Huang, F. Jin, and F. Chiang, "Quantitative evaluation of corrosion by a digital fringe projection technique," Opt. Laser Eng. **31**, 371–380 (1999).

[129] J. Burke, T. Bothe, W. Osten, and C. Hess, "Reverse engineering by fringe projection," Proc. SPIE **4778**, 312–324 (2002).

[130] P. Picart, D. Mounier, and J. M. Desse, "High-resolution digital two-color holographic metrology," Opt. Lett. **33**, 276–278 (2008).

[131] T. Saucedo-A, M. H. De La Torre-Ibarra, F. Mendoza Santoyo, and I. Moreno, "Digital holographic interferometer using simultaneously three lasers and a single monochrome sensor for 3d displacement measurements," Opt. Express **18**, 19867–19875 (2010).

[132] I. Yamaguchi, T. Matsumura, and J. . Kato, "Phase-shifting color digital holography," Opt. Lett. **27**, 1108–1110 (2002).

[133] C. A. Sciammarella, "Holographic moire, an optical tool for the determination of displacements, strains, contours, and slopes of surfaces." Opt. Eng. **21**, 447–457 (1982).

[134] C. A. Sciammarella, P. K. Rastogi, P. Jacquot, and R. Narayanan, "Holographic moiré in real time," Exp. Mech. **22**, 52–63 (1982).

[135] E. S. Simova and K. N. Stoev, "Automated fourier transform fringe-pattern analysis in holographic moiré," Opt. Eng. **32**, 2286–2294 (1993).

[136] A. Patil and P. Rastogi, "Phase determination in holographic moire in presence of nonsinusoidal waveforms and random noise," Opt. Commun. **257**, 120–132 (2006).

[137] A. Patil, R. Langoju, and P. Rastogi, "Constraints in dual phase shifting interferometry," Opt. Express **14**, 88–102 (2006).

[138] A. Patil, P. Rastogi, and B. Raphael, "A stochastic method for generalized data reduction in holographic moire," Opt. Commun. **248**, 395–405 (2005).

[139] A. Patil and P. Rastogi, "Maximum-likelihood estimator for dual phase extraction in holographic moire," Opt. Lett. **30**, 2227–2229 (2005).

[140] A. Patil, R. Langoju, and P. Rastogi, "Model-based processing of a holographic moire," Opt. Lett. **30**, 2870–2872 (2005).

[141] A. Patil and P. Rastogi, "Estimation of multiple phases in holographic moire in presence of harmonics and noise using minimum-norm algorithm," Opt. Express **13**, 4070–4084 (2005).

[142] A. Patil and P. Rastogi, "Rotational invariance approach for the evaluation of multiple phases in interferometry in the presence of nonsinusoidal waveforms and noise," J. Opt. Soc. Am. A **22**, 1918–1928 (2005).

[143] R. Langoju, A. Patil, and P. Rastogi, "Resolution-enhanced fourier transform method for the estimation of multiple phases in interferometry," Opt. Lett. **30**, 3326–3328 (2005).

[144] R. Langoju, A. Patil, and P. Rastogi, "Estimation of multiple phases in interferometry in the presence of nonlinear arbitrary phase steps," Opt. Express **14**, 7686–7691 (2006).

[145] A. Patil, R. Langoju, P. Rastogi, and S. Ramani, "Statistical study and experimental verification of high-resolution methods in phase-shifting interferometry," J. Opt. Soc. Am. A **24**, 794–813 (2007).

[146] S. Barbarossa, A. Scaglione, and G. B. Giannakis, "Product high-order ambiguity function for multicomponent polynomial-phase signal modeling," IEEE Tran. Sig. Proc. **46**, 691–708 (1998).

[147] D. S. Pham and A. M. Zoubir, "Analysis of multicomponent polynomial phase signals," IEEE Tran. Sig. Proc. **55**, 56–65 (2007).

[148] S. S. Gorthi and P. Rastogi, "Piecewise polynomial phase approximation approach for the analysis of reconstructed interference fields in digital holographic interferometry," J. Opt. A:Pure Appl. Opt. **11**, 065405 (2009).

Curriculum Vitae

Gannavarpu Rajshekhar
Date of Birth: 07/03/1984
Nationality: Indian
E-mail: g.rajshekhar.gec@gmail.com

Education

2009-2012   :   Doctor of Philosophy, Photonics Doctoral School,
                 Swiss Federal Institute of Technology at Lausanne (EPFL)

2006-2008   :   Master of Technology, Laser Technology,
                 Indian Institute of Technology Kanpur

2001-2005   :   Bachelor of Engineering, Electronics & Telecommunication Engineering
                 Government Engineering College (now National Institute of Technology) Raipur

Experience

2008-2009   :   Research Engineer, Automation Division, TATA Steel

2005-2006   :   Engineer, Videsh Sanchar Nigam Limited (TATA Communications)

Areas of Interest

Fringe analysis, Applied signal processing, Shape measurement, Non-destructive testing, Fringe projection, Digital holographic interferometry

Service

Guest Editor for the Special Issue on "Fringe Analysis Methods & Applications" in the journal *Optics and Lasers in Engineering*

Reviewer for the journals *Optics Express, Applied Optics, Optics and Lasers in Engineering*

Publications in peer-reviewed Journals

1. G. Rajshekhar, Sai Siva Gorthi, and Pramod Rastogi, "Strain, curvature and twist measurements in digital holographic interferometry using pseudo Wigner-Ville distribution based method", **Review of Scientific Instruments**, 80, 093107, 2009.

2. G. Rajshekhar, Sai Siva Gorthi, and Pramod Rastogi, "An adaptive window Wigner-Ville distribution based method to estimate phase derivative from optical fringes", **Optics Letters**, 34(20), 3151-3153, 2009.

3. G. Rajshekhar, Sai Siva Gorthi, and Pramod Rastogi, "Polynomial Wigner-Ville distribution based method for direct phase derivative estimation from optical fringes", **Journal of Optics A: Pure and Applied Optics**, 11(12), 125402, 2009.

4. G. Rajshekhar, Sai Siva Gorthi, and Pramod Rastogi, "Estimation of phase derivative using adaptive window spectrogram", **Journal of Optical Society of America A**, 27(1), 69-75, 2010.

5. G. Rajshekhar, Sai Siva Gorthi, and Pramod Rastogi, "Estimation of displacement derivatives in digital holographic interferometry using a two-dimensional space-frequency distribution", **Optics Express**, 18(17), 18041-18046, 2010.

6. Sai Siva Gorthi, G. Rajshekhar and Pramod Rastogi,"Strain estimation in digital holographic interferometry using piecewise polynomial phase approximation based method" **Optics Express**, 18(2), 560-565, 2010.

7. Sai Siva Gorthi, G. Rajshekhar and Pramod Rastogi, "Three-dimensional shape measurement using high-order instantaneous moments based fringe projection method" **Optics and Laser Technology**, 43(1), 40-44, 2011.

8. G. Rajshekhar, Sai Siva Gorthi, and Pramod Rastogi, "Estimation of dynamically varying displacement derivatives using fringe projection technique", **Applied Optics**, 50(3), 282-286, 2011.

9. G. Rajshekhar, Sai Siva Gorthi, and Pramod Rastogi, "Simultaneous multidimensional deformation measurements using digital holographic moiré", **Applied Optics**, 50(21), 4189-4197, 2011.

10. G. Rajshekhar, Sai Siva Gorthi, and Pramod Rastogi, "Simultaneous measurement of in-plane and out-of-plane displacement derivatives using dual-wavelength digital holographic interferometry", **Applied Optics**, 50(34), H16-H21, 2011.

11. G. Rajshekhar and Pramod Rastogi, "Application of complex-lag distributions for estimation of arbitrary order phase derivatives in digital holographic interferometry", **Optics Letters**, 36(19), 3738-3740, 2011.

12. G. Rajshekhar, Sai Siva Gorthi, and Pramod Rastogi, "Estimation of multiple phases from a single fringe pattern in digital holographic interferometry", **Optics Express**, 20(2), 1281-1291, 2012.

13. G. Rajshekhar, Sai Siva Gorthi, and Pramod Rastogi, "Detection of defects from fringe patterns using a pseudo Wigner-Ville distribution based method", **Optics and Lasers in Engineering**, 50(8), 1059-1062, 2012.

14. G. Rajshekhar and Pramod Rastogi, ``Fringe analysis: Premise and perspectives", **Optics and Lasers in Engineering**, 50(8), iii-x, 2012.

Publications in Conferences

1. G. Rajshekhar, Sai Siva Gorthi and Pramod Rastogi, "Comparative Analysis of Various Single-tone Frequency Estimation Techniques in High-order Instantaneous Moments Based Phase Estimation Method", International Conference on Advanced Phase Measurement Methods in Optics and Imaging, Locarno, Switzerland, **AIP Conference Proceedings** 1236, 355-358, 2010.

2. Sai Siva Gorthi, G. Rajshekhar and Pramod Rastogi, "Estimation of Phase in Fringe Projection Technique Using High-order Instantaneous Moments Based Method", International Conference on Advanced Phase Measurement Methods in Optics and Imaging, Locarno, Switzerland, **AIP Conference Proceedings** 1236, 359-362, 2010.